

# Dynamics of Electron Transfer Processes at the Surface of Dye-Sensitized Mesoporous Semiconductor Films

THÈSE N° 4731 (2010)

PRÉSENTÉE LE 25 JUIN 2010

À LA FACULTÉ SCIENCES DE BASE

LABORATOIRE DE PHOTONIQUE ET INTERFACES

PROGRAMME DOCTORAL EN CHIMIE ET GÉNIE CHIMIQUE

ÉCOLE POLYTECHNIQUE FÉDÉRALE DE LAUSANNE

POUR L'OBTENTION DU GRADE DE DOCTEUR ÈS SCIENCES

PAR

Joël TEUSCHER

acceptée sur proposition du jury:

Prof. H. Girault, président du jury  
Prof. J.-E. Moser, Prof. M. Grätzel, directeurs de thèse  
Prof. M. Chergui, rapporteur  
Prof. A. Hagfeldt, rapporteur  
Prof. E. Vauthey, rapporteur



ÉCOLE POLYTECHNIQUE  
FÉDÉRALE DE LAUSANNE

Suisse  
2010



# Résumé

Les réactions de transfert d'électron à la surface de semi-conducteurs sensibilisés sont des étapes clés du fonctionnement des cellules solaires à colorant. Après absorption de la lumière, un état excité d'un colorant injecte un électron dans un semi-conducteur à large bande interdite comme le dioxyde de titane,  $\text{TiO}_2$ . La forme oxydée du colorant peut alors être interceptée par un médiateur rédox, typiquement du iodure, avant que la réaction de recombinaison entre l'électron injecté et le colorant oxydé ne se passe. Ce médiateur transporte la charge positive jusqu'à la contre-électrode. Un quenching de l'état excité du colorant pourrait empêcher une injection d'électron efficace.

Afin de développer une cellule solaire à colorant optimale, il est important de garder le rapport entre le nombre de photons absorbés et le courant produit aussi unitaire que possible. Il est donc indispensable que chaque réaction se passe idéalement après la première étape, l'absorption d'un photon par le colorant. Un schéma cinétique de réaction, incluant les réactions indésirables, doit être établi. Les différents paramètres agissant sur ces réactions doivent être bien compris. Le but de ce travail est l'étude de ces réactions clés.

Le chapitre 1 passe en revue la théorie nécessaire à la compréhension des résultats expérimentaux. Le chapitre 2 résume les outils expérimentaux qui sont utilisés, ainsi que les modifications qui ont été implémentées sur le spectromètre pompe-sonde existant.

Dans le chapitre 3, une réaction ne conduisant pas à la production de courant est étudiée : le quenching réductif du colorant. Cette réaction

forme le colorant réduit et ce dernier n'injecte apparemment pas d'électron dans le  $\text{TiO}_2$ . Cette réaction nécessite deux conditions pour être observée. Premièrement, une adsorption au delà d'une monocouche, impliquant la présence d'agrégats à la surface du semi-conducteur est nécessaire. Ces molécules de colorant ne sont alors pas correctement couplées à la surface du  $\text{TiO}_2$ . La deuxième condition est l'utilisation d'une concentration élevée en iodure, typiquement plus grande que 1 M. Cette réaction a également été observée pour un système colorant/ $\text{Al}_2\text{O}_3$ . Ceci aide à l'observation de la formation du colorant réduit, qui se déroule dans les premières picosecondes suivant l'absorption de lumière. Ces résultats sont utilisables pour le développement de nouveaux électrolytes, qui devront minimiser cette réaction.

Le chapitre 4 consiste en une étude de la dynamique de régénération de l'état fondamental du colorant. Si le colorant est adsorbé en monocouche sur la surface du semi-conducteur, l'interception du colorant oxydé par le iodure est efficace pour un grand intervalle de concentrations du médiateur. L'utilisation de complexes bipyridyles de ruthénium comme sensibilisateurs engendre deux situations. La première est le résultat d'un mécanisme associatif, avec une vitesse de régénération du colorant qui atteint un maximum après saturation des sites actifs du colorant. La deuxième situation est un comportement répulsif. Si le colorant ne favorise pas l'approche des ions iodures, la dynamique de régénération en fonction de la concentration en iodure est ralentie. L'utilisation de quatre différents colorants organiques de type donneur-pont-accepteur (D- $\pi$ -A) montre des vitesses de régénération rapides et dépendantes de la structure du pont. Cette étude permet de mieux comprendre la réaction d'interception du colorant oxydé et peut ainsi aider à la conception de nouveaux colorants organiques, en montrant l'importance de l'accès du iodure au colorant.

Le chapitre 5 présente une étude approfondie d'un colorant organique, ayant une structure de type D- $\pi$ -A. Toutes les échelles de temps sont étudiées, des premières femtosecondes jusqu'à la milliseconde, afin d'observer

---

les réactions qui se passent à la surface du  $\text{TiO}_2$ . L'injection d'électron est étonnamment lente,  $\tau = 1.7$  ps. Toutefois, le cation du colorant ainsi formé est intercepté par un électrolyte à base de iodure avec un rendement de 99 %, confirmant le potentiel de ces molécules dans le développement des cellules solaires à colorant.

Le dernier chapitre permet d'ouvrir la discussion sur les projets futurs permettant de continuer cette recherche.

## Mots clés

transfert d'électron, dynamique, spectroscopie ultrarapide, cellule solaire nanocristalline à colorant, colorant D- $\pi$ -A, quenching réductif, régénération par le iodure.



# Abstract

Electron transfer reactions taking place at the surface of dye-sensitized semiconductors are key processes in dye-sensitized solar cells (DSSCs). After light absorption, the excited state of a dye injects an electron into a wide-bandgap semiconductor, usually titanium dioxide,  $\text{TiO}_2$ . The formed oxidized dye can then be intercepted by a redox mediator, typically iodide, before charge recombination between the injected electron and the oxidized dye occurs. This mediator transports the positive charge to a counter-electrode. A quenching of the dye excited state by the redox mediator might prevent efficient electron injection.

To develop an optimal DSSC device, it is important to keep the absorbed photon-to-current efficiency as quantitative as possible. Therefore, every reaction has to be ideally placed along the temporal evolution after primary step of photon absorption by the dye. A good kinetic scheme of reactions, including undesirable charge annihilation loss pathways needs to be established. The different parameters affecting all of these series of reaction has to be well understood. The aim of this dissertation is to investigate these key reactions.

Chapter 1 reviews the theoretical background necessary for understanding the following experimental results. Chapter 2 summarizes the experimental tools that are used throughout this work as well as the main advances that have been implemented to the existing pump-probe spectrometer.

In chapter 3, a potential annihilation reaction is investigated, namely the reductive quenching of the dye. This reaction leads to the formation of a

reduced dye that is not found to inject an electron into  $\text{TiO}_2$ . This reaction occurs under two specific conditions. It requires an overloading of dye on the semiconductor surface, leading to the formation of aggregates that are not properly electronically coupled to the  $\text{TiO}_2$ . It also occurs only when a high concentration of iodide redox mediator is used, typically larger than 1 M. This reaction is also observed on a dye/ $\text{Al}_2\text{O}_3$  system. Alumina is an insulator and precludes electron injection, allowing the observation of the reduced dye formation, which takes place within the first picoseconds after light absorption. These findings are relevant for the development of new electrolytes that will have to suppress this reaction pathway.

Chapter 4 contains a study on the dye ground state regeneration dynamics. When the dye is adsorbed as a monolayer onto the semiconductor surface, the oxidized dye interception is efficient over a broad range of iodide concentrations. When using ruthenium bipyridyl complexes as sensitizer, two different situations are encountered. The first one reveals an associative mechanism, with a rate of regeneration that reaches a maximum after saturation of the active sites of the dye. The second mechanism presents a repulsive behavior. When the dye structure renders more difficult the approach of iodide, the response of the regeneration dynamics to the bulk iodide concentration implies a sub-linear response. The use of four different organic donor-bridge-acceptor (D- $\pi$ -A) dyes revealed fast interception rates, dependant on the  $\pi$ -bridge structure. This study allows for a better understanding of the dye cation interception reaction and might help in the design of new organic dyes, revealing the importance of the access of iodide to the sensitizer.

Chapter 5 presents a wide study of an organic dye, having a D- $\pi$ -A structure. All the timescales are investigated, from the early femtoseconds to the millisecond for a complete map of the reactions that take place at the  $\text{TiO}_2$  surface. Electron injection is found to be surprisingly slow with a  $\tau = 1.7$  ps. The dye cation thus formed is intercepted by an iodide-based electrolyte with 99 % efficiency, confirming the potential of these dyes in the



development of DSSCs.

The last chapter opens the discussion on future projects for the continuation of this research.

## **Keywords**

electron transfer, dynamics, ultrafast spectroscopy, dye-sensitized solar cell, D- $\pi$ -A dye, reductive quenching, iodide regeneration.



# Contents

<b>1</b>	<b>Theoretical background and state of the art</b>	<b>1</b>
1.1	Solar light harvesting . . . . .	2
1.2	Dye-sensitized solar cells, DSSCs . . . . .	3
1.2.1	Semiconductors . . . . .	5
1.2.2	Dyes . . . . .	9
1.2.3	Anchoring and sensitization . . . . .	14
1.2.4	Electron injection . . . . .	17
1.2.5	Back electron transfer . . . . .	20
1.2.6	Regeneration of the dye ground state . . . . .	22
1.3	References . . . . .	25
<b>2</b>	<b>Experimental section</b>	<b>29</b>
2.1	Femtosecond spectrometer . . . . .	30
2.1.1	Laser source . . . . .	30
2.1.2	NOPA . . . . .	31
2.1.3	White-light-NOPA . . . . .	32
2.1.4	Labview integration . . . . .	35
2.1.5	Determination of the beam fluence . . . . .	35
2.1.6	Two color pump-probe transient absorbance . . . . .	37
2.1.7	Pump-white-light-continuum-probe transient absorbance	43
2.2	Nanosecond laser flash photolysis, transient absorbance spec-	
	troscopy . . . . .	49
2.3	Photoinduced absorption spectroscopy . . . . .	51

---

2.4	Steady-state UV-visible absorption and emission spectroscopies	53
2.5	Sample preparation . . . . .	53
2.5.1	Dyes . . . . .	53
2.5.2	Titanium dioxide . . . . .	54
2.5.3	Alumina . . . . .	54
2.5.4	Sample sensitization . . . . .	54
2.6	References . . . . .	55
<b>3</b>	<b>Reductive quenching of ruthenium dye excited states at the surface of oxides</b>	<b>57</b>
3.1	Introduction . . . . .	58
3.1.1	Reaction scheme . . . . .	59
3.1.2	State of the art . . . . .	61
3.2	Experimental part . . . . .	64
3.2.1	Chemicals . . . . .	64
3.2.2	Samples . . . . .	68
3.3	Results and discussion . . . . .	68
3.3.1	PIA spectroscopy . . . . .	68
3.3.2	Femtosecond transient absorbance . . . . .	75
3.4	Conclusions and outlook . . . . .	87
3.5	References . . . . .	91
<b>4</b>	<b>Iodide concentration dependance of sensitizer cations interception dynamics</b>	<b>95</b>
4.1	Introduction . . . . .	96
4.1.1	Reaction scheme . . . . .	96
4.1.2	State of the art . . . . .	97
4.2	Experimental part . . . . .	100
4.2.1	Chemicals . . . . .	100
4.2.2	Samples . . . . .	103
4.3	Results and discussion . . . . .	103
4.3.1	Fluence . . . . .	103

---

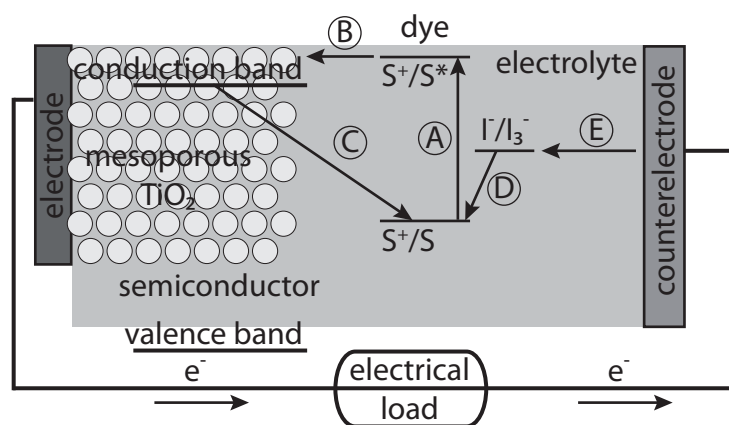
4.3.2	$I^-/S^+$ ratio . . . . .	105
4.3.3	Reciprocal regeneration half-time . . . . .	106
4.3.4	Ruthenium dyes . . . . .	108
4.3.5	Organic D- $\pi$ -A dyes . . . . .	114
4.4	Conclusions and outlook . . . . .	120
4.5	Aknowledgments . . . . .	123
4.6	References . . . . .	124
<b>5</b>	<b>Dynamics of an organic D-<math>\pi</math>-A dye sensitizing <math>TiO_2</math></b>	<b>127</b>
5.1	Introduction . . . . .	128
5.1.1	Organic D- $\pi$ -A dyes . . . . .	129
5.1.2	Electron injection into $TiO_2$ . . . . .	129
5.1.3	C204 state of the art . . . . .	131
5.2	Experimental part . . . . .	131
5.2.1	Chemicals . . . . .	131
5.2.2	Samples . . . . .	132
5.3	Results and discussion . . . . .	133
5.3.1	Absorption spectrum of the dye . . . . .	133
5.3.2	Emission spectroscopy . . . . .	134
5.3.3	Photoinduced absorption spectroscopy . . . . .	136
5.3.4	Nanosecond transient absorbance . . . . .	137
5.3.5	Femtosecond transient absorbance; two colors pump- probe . . . . .	139
5.3.6	Femtosecond transient absorbance; pump white-light- continuum-probe . . . . .	141
5.4	Conclusions and outlook . . . . .	151
5.5	References . . . . .	152
<b>6</b>	<b>Concluding remarks and outlook</b>	<b>155</b>



# Chapter 1

## Theoretical background and state of the art

### Graphical abstract



The dye-sensitized solar cell reaction scheme

The general discussion of this chapter is based on several references that are not cited in the text. They comprise three thesis,<sup>1-3</sup> three books,<sup>4-6</sup> and a recent review.<sup>7</sup>

## 1.1 Solar light harvesting

The sun is a sustainable energy source that could supply the whole energy demand of human beings. To illustrate its potential power, the total amount of energy that reaches the earth within one day could power the entire planet for a whole year.

The photosynthesis is a well known example of the use of solar energy. Plants, algae and several bacteria harvest the sun for converting carbon dioxide into organic compounds such as sugars. This process is crucial for life on earth and helps to maintain the normal level of oxygen in the atmosphere.

The total amount of energy stored by photosynthesis is approximately 100 terawatts per year. Chlorophyll is a major dye used for the conversion of light into energy by plants. The concept behind transformation of energy of light into chemicals has been understood in the middle of the 20th century.

Mankind uses the sun as a source of energy since the early times. Currently, three main ways of converting sunlight to a useable source of energy are industrially developed. Biofuels are a form of stored solar energy. Solar furnaces are devices that collect solar energy and convert it into heat, either for water heating for residential or commercial use or for electric power generation through steam production. A third possibility is to use light for moving electrons and therefore generating electricity.

Silicium photovoltaic cells currently dominate the market with commercial devices having conversion yields, varying upon the technology, from 5 to 25 %. However, this technology is limited by high production costs, high energetic costs and problematic integration in the built environment.

Several alternative photovoltaics are competing with the silicium based devices. Thin-film photovoltaics (CdTe, CIGS, amorphous silicium) and



concentrator modules are directly derived from the silicon technology. All-organic devices are made possible with the use of conducting organic polymers.

Organic solar cells can have different design. The single layer version is very inefficient and is not applicable to an industrial production. Multilayer cells rely on an interface between an electron donor (n) and an electron acceptor (p) material or a bulk-heterojunction formed between n and p interpenetrated materials.

Finally, dye-sensitized solar cells are photovoltaic devices in which a dye is used as the light absorber and a semiconductor electrode (essentially titania) allows for the charge separation and the transport of the electron to the external circuit. The next section will give more details on this type of photovoltaics, which is another example of the use of a bulk heterojunction.

## 1.2 Dye-sensitized solar cells, DSSCs

Sensitization allows for extending the absorption spectrum useable for free carriers generation within a semiconductor. A dye absorbs visible light and its excited state has an oxidation potential that allows for electron injection into the conduction band of the semiconductor.

At first, most sensitization studies involved electrochemical measurements of sensitized wide-bandgap semiconductor planar electrodes. These allowed to measure efficient electron injection and demonstrated that dye sensitization was a strategy for populating the conduction band of semiconductors with electrons under visible light. However, the development of efficient devices for current collection was impossible due to the low light harvesting capability of single layers of an absorber on the surface and therefore low current densities.<sup>8</sup>

A breakthrough for these cells was constituted by the replacement of the planar electrode by a mesoporous nanocrystalline semiconductor film, possessing a high surface area.<sup>9</sup> The surface area allowing for a sensitizer

to bind on the surface can be three orders of magnitude larger than the geometric area of the sample on a 10  $\mu\text{m}$  thick sample. This has allowed for a drastic increase of the performances of DSSCs, reaching currently a power conversion yield of 12 %.<sup>10</sup>

In nanosized systems, the conduction band is flat within semiconductor particles. In the case of bulk semiconductors, with a planar interface, the band bending inhibits the recombination between the injected electron and the hole on the oxidized dye molecule. In the case of nanoparticles, the conduction band is flat and no electric field prevents back electron transfer. Another mechanism should thus prevail, that ensures efficient sustainable charge separation.

The general mechanisms behind such devices have been first described for the sensitization of planar semiconductors, but remains similar with the use of mesoporous materials. The reactions involved are depicted in figure 1.1. Light is absorbed by a sensitizer which is bound to the surface of a semiconductor (A). This prepares an electronically excited state. This state can inject an electron into the conduction band of the semiconductor (B). The oxidized sensitizer thus formed can recombine with the injected electron (C) or be regenerated by an external electron donor (D). The competition between these two reactions is crucial to the photon-to-current conversion yield of the system. The extracted electron can then perform work in an external circuit and return to a counter-electrode. The oxidized electron donor transports the positive charge to the counter-electrode where it is reduced (E). As a result, no net chemistry occurs, but electrical work has been produced.

These reactions enter in competition with a series of unwanted reactions that might occur within the system. The recombination of the injected electrons with either the oxidized sensitizer (C) or the oxidized redox mediator (reaction not shown) are the two major channels for charge annihilation.

As a consequence, the timescales of these reactions and the competition

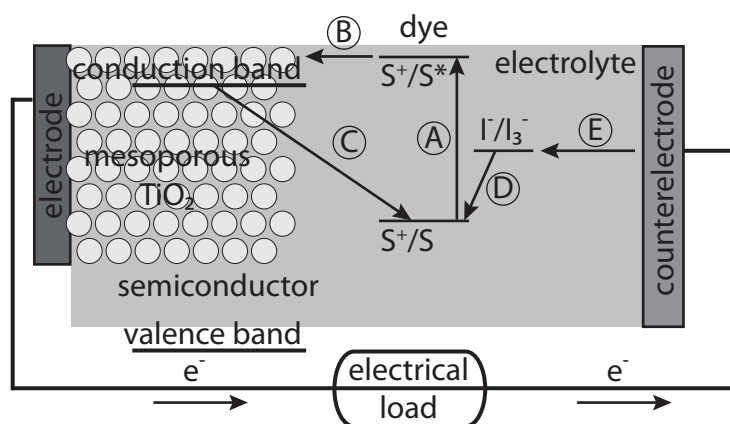


Figure 1.1: Schematic depicting a dye-sensitized solar cell. The main steps are: A. light absorption, B. electron injection, C. recombination, D. interception of the oxidized dye by a redox mediator, E. redox mediator regeneration at the counter-electrode.

between different channels are the key point for efficient current collection.

### 1.2.1 Semiconductors

A semiconductor is a material in which low concentrations of charge carriers can be produced either by thermal- or photo-excitation, or by chemical doping. Intrinsic semiconductors are characterized by a fully occupied valence band and an empty conduction band. Intrinsic absorption of photons, whose energy is larger than the bandgap, produces electron-hole pairs. Metal oxides such as TiO<sub>2</sub>, SnO<sub>2</sub> or ZnO are wide bandgap semiconductors. They do not absorb visible light, being characterized by bandgaps larger than 3 eV.

Unlike in molecular systems, the energy levels involved are broad and form bands instead of discrete energy levels.

In a semiconductor, photons with energies greater than the bandgap might be absorbed. This allows for the promotion of an electron to the conduction band, leaving a hole in the valence band. After some time, the free charge carriers cool down to the band edges. Trap states are states within the bandgap, that can accept either holes or cooled electrons. They

are often physically characterized by surface states or crystal defects. The recombination of an electron and a hole can take place either from free carriers or between trapped charges and can be either radiative or non-radiative. The timescale of this reaction spread over several orders of magnitude. Some trapped charges are stable for weeks.

### **The semiconductor-electrolyte interface**

The three important potentials at the interface are the conduction band edge potential  $\phi_{cb}$ , the flat-band potential  $\phi_{fb}$ , corresponding to the conduction band edge at the interface, and finally the Fermi potential  $\phi_F$ . The Fermi potential is calculated from the Fermi energy level,  $\phi_F = -E_F/\mathcal{F}$  ( $\mathcal{F}$  is the Faraday constant).  $\phi_F$  is considered as the electrochemical potential of the electrons in a semiconductor.

At the interface between the semiconductor and the electrolyte, solvent molecules or ions in the solution can adsorb on the surface of the solid. This can shift the flat-band potential significantly. Also the density of trap states affects the flat-band potential.

Typically in titanium dioxide nanocrystalline films, with a particle size of the order of 15 nm, the conduction band is flat, so  $\phi_{cb} \approx \phi_{fb}$ . If  $\phi_F < \phi_{cb}$ , electrons can percolate inside the nanocrystalline film. The absence of an electric field across the material is a characteristic of a nanostructured film compared to the bulk material. This limits the mechanism, within a mesoporous network of nanoparticles, to diffusion of the electrons in a random walk process rather than by migration.

In the particular case of electron injection into semiconductors, the  $\phi_F$  is not a relevant parameter, because the system is not at equilibrium conditions.  $\phi_{fb}$  and therefore  $\phi_{cb}$  will be the relevant potentials.

### **Titanium dioxide**

The semiconductor of choice for making DSSCs is titanium dioxide,  $\text{TiO}_2$ , also known as titania. This material has a strong ionic character and can be

seen as being constituted of  $\text{Ti}^{\text{IV}+}$  and  $\text{O}^{2-}$  ions. The conduction band is formed by the 3d orbitals of titanium and the valence band is formed by the 2p orbitals of oxygen.

$\text{TiO}_2$  is commercially available and widely used in industrial applications. Its properties such as a high refraction index, a good chemical stability, an amphoteric surface and a low production cost are the main advantages accountable for its broad use. It can be used as a white pigment or as a photocatalyst in self-cleaning surfaces, for example. Its availability on earth is big and its toxicity is low. These properties render  $\text{TiO}_2$  the material of choice for DSSC devices.

The most common form of this oxide in nature is rutile. Another form is brookite. A third form of this oxide is anatase, which is the thermodynamically stable crystalline form at high pressure. Its crystal structure is shown in figure 1.2.

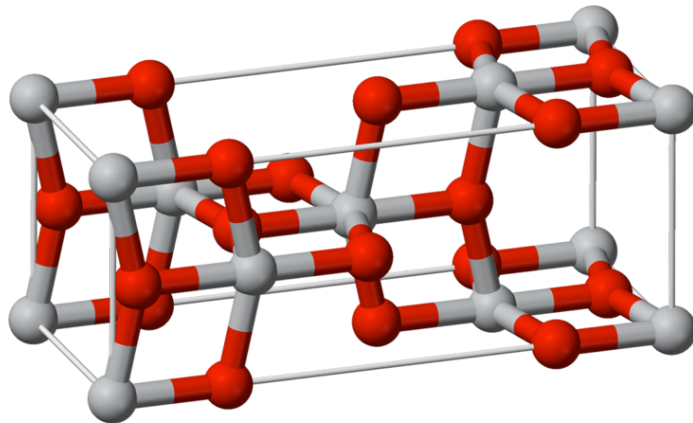


Figure 1.2: Crystal structure of anatase.

Nanoparticles of anatase can be synthesized and therefore the preparation of nanocrystalline mesoporous anatase films is feasible. Deposition of these nanoparticles onto a substrate, typically glass, is easy. A sintering process allows for the conduction between particles. A polymer, typically ethylcellulose, is inserted in the preparation before the sintering and defines

the size and the number of the pores, therefore the porosity of the film. Transparent films are prepared with an active area of about 100 times the geometric area per micrometer of thickness.

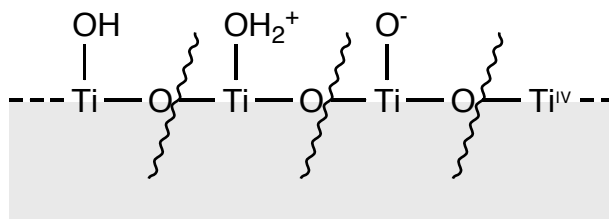


Figure 1.3: Scheme of the different surface titanium ions. From left to right, hydroxylated, protonated, deprotonated and dehydroxylated.

When prepared from aqueous precursors or in the presence of water vapor,  $\text{TiO}_2$  has a hydroxylated surface. In acidic medium, hydroxyl groups, as well as bridge oxygen atoms, are protonated, thus providing a positive charge to the surface. In basic conditions, a negative surface charge is rather produced by the deprotonation of hydroxyl groups. These different surface states are depicted in figure 1.3.

When treated at temperatures above 300 °C, the surface of  $\text{TiO}_2$  is gradually deprotonated, leaving the strong Lewis acidic  $\text{Ti}^{\text{IV}+}$  exposed to the surrounding medium. These sites are therefore involved in chemisorption of Lewis bases onto the surface.

Dispersed nanoparticles in propylene carbonate exhibit a negative zeta potential of -20 mV and even -30 mV when dyed with ruthenium complexes.<sup>11</sup> During sintering, the oxide has been calcinated at 450 °C and therefore its surface is mainly dehydroxylated. Upon addition of a dye, chemisorption overcomes electrostatic repulsion and thus renders the surface more negative. The surface charge will be relevant for dealing with the adsorption of the dye on the surface as well as with the adsorption of other species present in the electrolyte.

## 1.2.2 Dyes

### Ruthenium polypyridyls compounds

Efficient sensitizers are found within ruthenium polypyridyls dyes. These compounds have maximum  $\varepsilon$  values that are relatively small, typically around  $15'000 \text{ l} \cdot \text{mol}^{-1} \cdot \text{cm}^{-1}$ . They also have a broad absorbance over the visible. It renders these dyes usually red, from orange to dark garnet.

Such  $\varepsilon$  values corresponds to a cross section of about  $0.5 \text{ \AA}^2$ . Therefore for dye molecules with a geometric area of more than  $100 \text{ \AA}^2$  the probability of absorbing a photon is small and the absorptance of a dense dye monolayer cannot exceeds 0.5 %. In contrast, when used in combination with mesoporous materials possessing large internal surface area, having a roughness factor up to  $100 \mu\text{m}^{-1}$ , they allow to achieve efficient light collection with layers of  $10 \mu\text{m}$  thickness.

Many of the dyes employed in DSSC development are of the form  $\text{Ru}(\text{bpy})_2(\text{SCN})_2$ , the bpy unit being a functionalized bipyridyl unit. The two isothiocyanate groups are responsible for a shift of the highest occupied molecular orbital (HOMO) from the metal center to them. This enhances the visible absorption of the dye by shifting its absorption spectrum to the red.

The units grafted on the bipyridyl ligand have two goals. The first is to attach the dye on the semiconductor surface with an anchoring group such as carboxylate ( $\text{CO}_2^-$ ) or phosphonate ( $\text{PO}_3^{2-}$ ) moieties.<sup>12-14</sup> The second objective is to modify the surroundings of the dye. Typically, alkyl chains are added for preventing multilayer adsorption and forming a barrier to the surface.<sup>15,16</sup> Another interesting functionalization lies in the addition of chromophores allowing for extension of the  $\pi$ -system and therefore enhancing the molar extinction coefficient as well as shifting the spectral response to the red, improving the light harvesting efficiency.<sup>17,18</sup>

Figure 1.4 illustrates three examples of  $\text{Ru}(\text{bpy})_2(\text{SCN})_2$ . N719 (a. on figure 1.4) is the diprotonated analogue to the N3 dye. It possesses two

tert-butylammonium groups to balance the net charge of this compound to zero. Z907 compound (b. on figure 1.4) is a typical amphiphilic analogue of N719. When adsorbed on a surface, the two alkyl side chains are positioned in the direction of the surrounding medium and will form a barrier to the surface. Their shape will be dependent on the polarity of the surrounding media. Z993 dye possesses two thiophene groups that are inserted between the bipyridyl unit and the anchoring group. This will mainly enhance the absorption spectrum of the dye by extending the  $\pi$ -conjugation of the bipyridyl ligand.

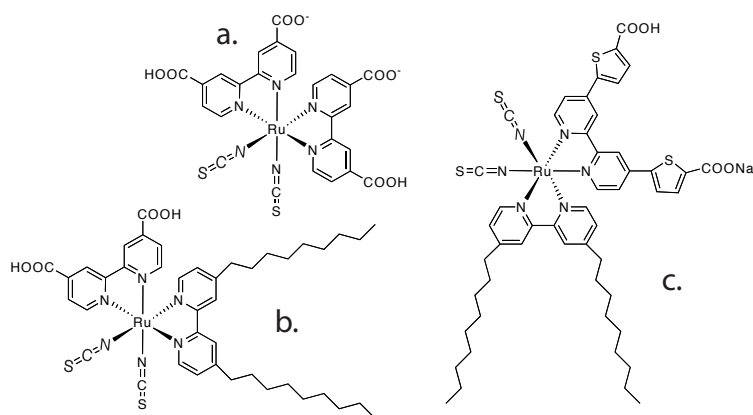


Figure 1.4: State of the art ruthenium polypyridyls dyes. a. N719, b. Z907, c. Z993, N719 is cis-bis(isothiocyanato)bis(4,4'-dicarboxylic-2,2'-bipyridyl) ruthenium(II), Z907 is cis-bis(isothiocyanato)(4,4'-dicarboxylic-2,2'-bipyridyl)(4,4'-dinonyl-2,2'-bipyridyl) ruthenium(II) and Z993 is cis-bis(isothiocyanato)(4,4'-dithiophenecarboxylic-2,2'-bipyridyl)(4,4'-dinonyl-2,2'-bipyridyl) ruthenium(II).

**Electronic transitions** The metal-to-ligand charge transfer (MLCT) excited state is populated after light absorption. An electron is promoted from the metal  $d$  orbitals to the ligand  $\pi^*$  orbitals. According to the Franck-Condon principle, the initially formed excited state has the same structural symmetry as the ground state. This  $^1\text{MLCT}$  is followed by the formation of a  $^3\text{MLCT}$  manifold.

The absorption spectrum of these compounds can be tuned. Especially



the MLCT bands can be tuned by changing the substituents on the bipyridyl ligands. These changes will also affect the redox potential of the dye and are therefore to be monitored in detail. Addition of substituents to bipyridyl with low lying  $\pi$  orbitals, such as aromatics or esters can enhance MLCT extinction coefficients, especially when grafted at the 4 and 4' positions.<sup>17,19</sup>

N3 (fully protonated N719) dye and its derivatives have been often compared to ruthenium(II) trisbipyridyl ( $\text{Ru}(\text{bpy})_3$ ).  $\text{Ru}(\text{bpy})_3$  complex has been widely studied and its photophysics is well documented.<sup>20</sup> This allows for assigning the visible absorption bands of N3 and analogues by comparison to its parent dye  $\text{Ru}(\text{bpy})_3$ .<sup>21</sup>

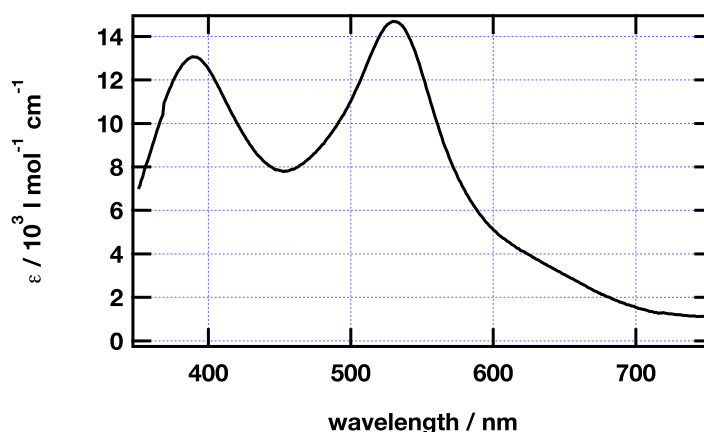


Figure 1.5: Absorbance spectrum of N719 dye in ethanol.

Figure 1.5 is the absorption spectrum of N719 dye in ethanolic solution. The 530 nm absorption band is attributed to a  $t_{2g} \rightarrow \pi^*$  MLCT transition. This excited state is weakly luminescent and has a lifetime of the order of 10 nanoseconds. On this timescale, this state comprises numerous MLCT states of mainly triplet character.

**Excited state evolution** In a ruthenium-dye-sensitized DSSC, the electron injection following light absorption is ultrafast ( $< 100$  fs).<sup>22</sup> It is therefore of major importance to know the timescale for the equilibration of

Ru(II) thexi states,  $^3\text{MLCT}$ . The  $^1\text{MLCT}$  state of N3 dye has a  $t_{1/2} = 30$  fs and the cooling of the triplet completes within 80 fs ( $t_{1/2}$ ) when the sensitizer is bound to mesoporous  $\text{TiO}_2$ .<sup>23</sup>

A Jablonski diagram is the picture of choice for representing these timescales. Figure 1.6 depicts the different channels that a sensitizer undergoes upon light absorption. Excited state deactivation can take place either in a radiative or in a non-radiative way. The latter case implies vibrational relaxation which is dependant on the surrounding atoms and media such as neighbouring molecules of the solvent. As a consequence, it ranges over a wide timescale. On the other side, radiative deactivation, phosphorescence and fluorescence, takes place from the lowest vibrational level, following Kasha's rule.

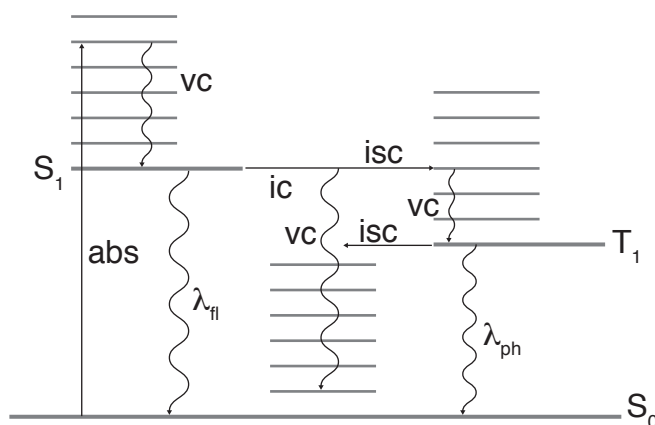


Figure 1.6: Jablonski diagram for an imaginary dye.  $S_0$ : singlet ground state,  $S_1$ : singlet first excited state,  $T_1$ : triplet excited state. abs: absorption, vc: vibrational cooling, ic: internal conversion, isc: intersystem crossing,  $\lambda_{fl}$ : fluorescence,  $\lambda_{ph}$ : phosphorescence.

### Organic D- $\pi$ -A dyes

Ruthenium dyes have several drawbacks such as the need of ruthenium itself or their relatively low extinction coefficients. In contrast, large  $\pi$ -aromatic molecules such as porphyrins, phthalocyanines and perylenes are potential

sensitizers for  $\text{TiO}_2$ . They all have high light harvesting capability as well as good photostability.<sup>24</sup>

Nevertheless, porphyrins for example, even with an intense Soret band around 400 nm and several Q-bands around 600 nm only present poor light harvesting properties over the solar spectrum compared to ruthenium-based complexes. Phtalocyanines remain transparent to a large part of the visible spectrum. Their tendency to aggregate is a major disadvantage that render them weak sensitizers because of an increased distance between the dye and the semiconductor.

Several improvements to these organic dyes have been made recently. The addition of push-pull groups to the structure of these dyes allows for improving the electron injection efficiencies, by improving the dye coupling to the surface. Insertion of substituents to reduce the aggregation is also a key parameter.

Indoline dyes, as well as coumarin dyes, tend to form aggregates of the J form when adsorbed onto  $\text{TiO}_2$ . Addition of alkyl chains to the indoline core helps preventing this aggregation and allows for efficient sensitization of the semiconductor.<sup>25</sup> The use of chenodeoxycholic acid as a co-adsorbent also allows for suppressing the dye aggregation. Therefore, this additive is often used in the preparation of organic DSSCs.

Most recent work involved dyes with a donor- $\pi$ -bridge-acceptor structure, which appears very robust.<sup>18</sup> Figure 1.7 illustrates the structure of such a molecule.



Figure 1.7: Structure of D- $\pi$ -A dyes.

These dyes are built from the same scheme. The electron donor moiety is

typically constituted by a triarylamine.<sup>26</sup> The acceptor is also the anchoring group, typically a cyanoacrylate group. This group attaches to the surface in a similar way to a carboxylic acid as no particular involvement of the cyano moiety with  $\text{Ti}^{\text{IV}+}$  surface atoms is observed. This design allows for an efficient localization of the electron in their excited state, as close as possible to the semiconductor surface. The conjugated bridge that links these two units is typically made of conjugated thiophene derivatives, rendering the bridge conducting.

With this design, molecular calculations show that the electron density of the HOMO (Highest Occupied Molecular Orbital) mainly lies on the triarylamine. Oppositely, the LUMO (Lowest Unoccupied Molecular Orbital) is centered at the cyanoacrylate unit.<sup>27</sup> Hence, upon light absorption, electrons are delocalized through the  $\pi$ -bridge from the triarylamine to the anchoring group. This allows for an efficient coupling of the excited state wave function with the conduction band states of the semiconductor.<sup>18</sup>

Contrary to ruthenium dyes, the photophysics of these D- $\pi$ -A dyes has not been intensively studied yet. As a consequence, not much is known on the evolution of their excited states and luminescence properties. A study reports the role of the anchoring group to the electron injection dynamics.<sup>28</sup>

### 1.2.3 Anchoring and sensitization

Because  $\text{TiO}_2$  does not absorb light at energies smaller than its bandgap of 3.2 eV (400 nm), it needs to be sensitized for efficient absorption of the solar light. Typically a dye is used to sensitize the semiconductor, but also quantum dots such as cadmium sulfide or lead sulfide can be efficient sensitizers.<sup>29-32</sup>

Therefore, the sensitization process allows for extending the absorption spectrum useable for free carriers generation within the conduction band. This scheme is illustrated in figure 1.8. The dye is excited by visible light and its excited state has an oxidation potential that allows for electron injection into the conduction band of the semiconductor.

A direct drawback of sensitization for generating an electrical current is that all the excess energy contained in the dye excited state is lost in cooling of the electron, either in the dye excited state or down to the conduction band edge level.<sup>33</sup>

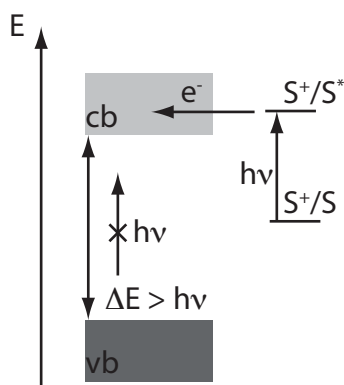


Figure 1.8: Dye sensitization mechanism. Light with energy  $h\nu$  cannot promote any electron from the valence band (vb) to the conduction band (cb). The sensitizer (S) LUMO lies above the conduction band edge of the semiconductor. Oxidation of  $S^*$  is feasible and an electron ( $e^-$ ) can be injected into the semiconductor.

Practically, it has been found that anchoring the sensitizer to the semiconductor surface is the most practical approach for an efficient sensitization.<sup>34</sup> Anchoring of dyes to the  $\text{TiO}_2$  surface requires groups that can form bonds with the acidic  $\text{Ti}^{4+}$  surface ions. Such groups are generally Lewis bases and are found within carboxylates, phosphonates, alcohols and amides for example. Ruthenium complexes with carboxylic acid units are the most efficient in DSSCs up to now. For organic D- $\pi$ -A dyes, cyanoacrylate is the state of the art anchoring group. Carefully designed linkers can be useful to control the distance from the semiconductor surface to the dye chromophore core. It allows for tuning the properties of the dye and preventing aggregation of the sensitizer.<sup>12</sup> Without the influence of aggregation, adsorption isotherms on nanocrystalline  $\text{TiO}_2$  show clean Langmuir behaviour.

The carboxylate-type linkage formed upon adsorption by a carboxylic acid (or a cyanoacrylate) to the semiconductor surface promotes rapid electron transfer into the conduction band of  $\text{TiO}_2$ . This adsorption leads to a loss of protons by the sensitizer. The exact location of these protons after adsorption remains unclear and therefore the formal charge of the bound sensitizer is often omitted.

The manifold of  $^3\text{MLCT}$  states observed in solution for ruthenium dyes is often considered as unperturbed upon adsorption. The electron injection is ultrafast and therefore usually precludes any slower relaxation process arising from the excited state. Also the lateral transfer between adjacent adsorbed dyes can be neglected due to the ultrafast nature of electron injection.

A good anchoring group, such as carboxylic acid derivatives, forms a strong bond with the metal oxide nanoparticle. This allows for an increase in the electronic coupling between the dye and the semiconductor, leading to fast electron injection rates. It also implies that the insertion of a spacer between the chromophore and the anchoring group can slow down the electron injection dynamics, according to equation 1.3 that will be introduced in the next section.

Practically, the photoinduced electron injection thermodynamics implies that the oxidation potential of the dye excited state is more negative than the flatband potential of the semiconductor, which is equal to the conduction band potential for nanoparticles. If the coupling between the dye and the semiconductor is large enough, direct electron injection into trap states is feasible, even if the conduction band potential lies at a higher energy.<sup>35</sup>

In general, the sensitization of wide bandgap semiconductors is relevant for many other applications than DSSCs. Photochromic and electrochromic devices, photography, xerography and displays are some of the affected fields. As a consequence, many future area of research and applications have been revealed.<sup>12,36</sup>

### 1.2.4 Electron injection

The classical theoretical treatment of molecular electron transfer (ET) is described by Marcus. His theory allows for the prediction of ET rates for many systems. The main assumption is that the vibronic coupling is strong and that ET is controlled by nuclear motion. When the acceptor and donor electronic levels are resonant, the electron can tunnel between these states.

The Born-Oppenheimer approximation<sup>i</sup>, allows to consider the nuclei frozen during the electron motion, obeying the Franck-Condon principle. In the non-adiabatic limit, the simplest kinetic model for a radiationless process is derived from Fermi's golden rule, equation 1.1. The rate constant of the reaction can be depicted as the product of a Franck-Condon weighted density of states (FCWD), which depends on the interaction between the acceptor and donor vibrational wavefunctions and an electronic term proportional to  $|H_{el}|^2$ , the electronic coupling matrix element squared.

$$k_{et} = \frac{2\pi}{\hbar} \cdot |H_{el}|^2 \cdot FCWD \quad (1.1)$$

In the case of a large number of acceptor states, like it is found in semiconductors, the FCWD factor is very large and constant, and reduces to a density of final electronic states.<sup>37</sup> Therefore the electron transfer rate is controlled by the electronic coupling between the donor and acceptor orbitals and the acceptor states density. In other words, the timescale for electron injection is mainly dependent upon the tunneling across the interface. This leads to a relation, analogous to Fermi's golden rule (equation 1.1) depending only on the electronic coupling and the acceptor state density within the conduction band,  $\rho(cb)$  (equation 1.2).

$$k_{et} = \frac{2\pi}{\hbar} \cdot |H_{el}|^2 \cdot \rho(cb) \quad (1.2)$$

$|H_{el}|^2$  is predicted to decline exponentially with the distance between

---

<sup>i</sup>The Born-Oppenheimer approximation allows the wavefunction of a molecule to be split into its electronic and nuclear (vibrational, rotational) components.

the donor and acceptor because of the exponential radial character of the electronic wavefunctions of the donor and acceptor species. If the FCWD is not dependent on the distance, the rate constant of electron transfer can be approximated as relation 1.3 using  $\beta$ , a damping factor given in  $\text{\AA}^{-1}$ .

$$k_{et} = k_0 \cdot \exp(-\beta(r - r_0)) \quad (1.3)$$

On  $\text{TiO}_2$ , the electron transfer has been reported to take place on timescales from less than 10 fs to several microseconds, depending on the conditions. To explain such a spread of reaction rates, only different values of the electronic coupling can be invoked. This variation of the dynamics can be explained with equation 1.3, having a distance of 15  $\text{\AA}$ , with an arbitrary damping factor of 1.2  $\text{\AA}^{-1}$ . Such a difference can be explained by different types of adsorption of the dye onto the surface.

As a consequence of relation 1.2, the electron injection will be independent of the temperature, independent of the reorganization energy and of the free Gibb's energy. Therefore, this particular electron transfer will not be governed by the thermodynamics.

A good sensitizer design will therefore locate the LUMO of the dye as close as possible to the  $\text{TiO}_2$  surface. This will help to couple the empty  $\text{Ti}^{\text{IV}}$ -3d orbital manifold of the semiconductor with the LUMO of the dye, which can be extended to the anchoring group for a better overlap.

For  $\text{Ru}(\text{II})$  compounds, the nature of the injecting state is the MLCT state of the sensitizer. Such charge separation occurs on a femtosecond to picosecond timescale and experimentally, the electron injection is reported with a non-exponential behavior attributed to three main factors. The surface heterogeneity of  $\text{TiO}_2$  and its density of states (DOS), the mode of the binding onto the surface as well as the presence of aggregated dye molecules and electron injection arising from different states in the thermal relaxation pathway are these three parameters. Many reasonable explanations are given to rationalize this complex dynamics, but a complete mechanistic model still lacks.



For the fastest electron injection reported, as short as 25 fs for Ru(II) sensitizers, singlet injection is predominant with a vibrational wave packet injecting the electron into the semiconductor. This behavior precludes any aggregation on the dye, because of the strong electronic coupling needed.

The longer electron injection time components reported, varying the conditions, are attributed to several factors. A well defined conduction band potential is not relevant to excited state injection into these nanocrystalline thin films. Therefore, a difference in the conduction band edge potential, induced by coadsorbed ions (proton adsorption for example) decreasing the DOS of TiO<sub>2</sub> might be a cause for a slower injection dynamics.

Also a multilayer adsorption of the dye onto the surface, leading to variations of the distance between the donor and the acceptor might be the cause for such broad dynamics. In this case, the spread of the dynamics over time reflects the spread of dye-to-semiconductor distances.

Other propositions implicate triplet injection, i.e. cooled sensitizer injection, in relation to the different excited state reduction potential of the triplet. However, it remains unclear why the dye would “wait” for injection, letting time for an efficient intersystem crossing. These slower time components lie in the 100 ps time domain. However, due to the long lifetime of the MLCT excited states, there is still much room for a quantitative injection yield.

In the environment of a functional DSSC device, the electron injection might be rather different than what has been reported for model samples. The presence of various additives such as lithium salts as well as the redox mediator, iodide, might alter the injection dynamics. However, the electron injection remains quantitative. In extreme cases, the local iodide concentration might be high enough to lead to reductive quenching of the excited sensitizer. The reduced dye thus formed can also inject an electron into the semiconductor, leading to a process that is called supersensitization.

### 1.2.5 Back electron transfer

The timescale for the back electron transfer in ruthenium dye-sensitized TiO<sub>2</sub> nanoparticles, also called the recombination reaction, takes place in the hundreds of micro- to milliseconds time domain.

The origin of this huge difference in timescale between the forward and back electron transfer rate has to be explained. The forward electron transfer originates from the  $\pi^*$  orbital of the MLCT state, but the back reaction has to reach the Ru(III) metal center to complete its  $t_{2g}$  orbitals. As a consequence, the electronic coupling might be completely different for the two reactions. In addition, it is known that the recombination reaction lies in the inverted Marcus region, whereas the electron injection is nearly activationless, occurring to a continuum of acceptor states and having therefore a FCWD close to unity. These factors can explain the big difference between the forward and back electron transfer reactions.

Classical Marcus theory predicts a parabolic dependance of the rate constant on the driving force of the reaction. The maximum rate constant is attained at the maximum of the parabola in activationless condition ( $-\Delta G^0 = \Lambda$ , where  $\Lambda$  is the reorganization energy of the system). The processes occurring at higher driving forces ( $-\Delta G^0 > \Lambda$ ) are therefore slower, lying within the inverted region. Because efficient sensitizers are generally characterized by an oxidation potential of their excited state having an energy slightly above the conduction band edge,  $|\Delta G^0|$  of the back electron transfer is large. Therefore the recombination reaction is located within this inverted region ( $-\Delta G^0 > \Lambda$ ).

A temperature-independent rate constant, and a pseudo-activationless behavior are observed in such conditions as a consequence of nuclear tunneling effects that become very important within the inverted region. The potential energy parabola of the initial state is inscribed into the potential energy parabola of the acceptor state and consequently, even the lower vibrational modes of the donor are overlapped with higher modes of the acceptor. The classical approach is not valid anymore in the inverted

region and the tunnelling is taken into account in a semi-classical description of the nuclear factor FCWD. Internal vibrations, which are approximated by a single collective high frequency vibrational mode ( $h\nu > kT$ ), are treated quantum mechanically, while solvent reorganization and internal low frequency modes are grouped in a continuum of states and considered classically. As a consequence, the Marcus curve, modified for this quantum effect, is not symmetrical anymore, but distorted in the inverted region.

The back electron transfer is also dependant on the reorganization energy, and therefore on the solvent. In the inverted Marcus region, an increase in the reorganization energy implies an increase in the rate constant. Oppositely, a smaller reorganization energy leads to a decrease of the reaction rate constant. This effect is inverted in the normal region.

The details of the preparation of the  $\text{TiO}_2$  films are crucial to the observed behavior and might explain the differences in the conflicting results reported within the literature, such as rate constants independent of the ground state reduction potential of the sensitizer. The films are in several studies pretreated with  $\text{TiCl}_4$  and the measurements are performed in different chemical environments, from vacuum to complete electrolytes, comprising several ionic species that can alter the redox chemistry.

Another factor greatly influencing the recombination dynamics is the number of injected electrons, i.e. the charge density within the semiconductor. This has been investigated, either by applying an electrical bias to the substrate or by allowing for many electrons being injected per nanoparticles. With excitation light intensities generating less than one electron per nanoparticle, the reaction half-times have shown remaining invariant.

A distance dependent electron tunneling can also be studied in the case of the recombination reaction and should reveal an exponential behavior versus the distance according to equation 1.3, similarly to the electron injection case. However, this distance dependence might be difficult to investigate, especially for sensitizer that are bound with non-rigid anchoring groups. Such groups

might let some degrees of freedom to the dye, not ensuring for a perfectly orthogonal adsorption and therefore not defining a reliable distance.

With the introduction of hole acceptor units on a ligand of the ruthenium complex<sup>38</sup> or with organic D- $\pi$ -A dyes,<sup>27</sup> the distance between the hole of the oxidized dye and the TiO<sub>2</sub> surface is important. A good spatial separation can ensure a longer oxidized dye lifetime, letting time for quantitative interception by a redox mediator.

### 1.2.6 Regeneration of the dye ground state

In DSSCs, the electrolyte comprises a redox mediator. The reduced form of this mediator has to regenerate the dye ground state prior to the back electron transfer. Ideally, this redox mediator should not absorb light to prevent photon-to-current efficiency losses.

#### Iodide

The first data reporting efficient interception of a Ru(III) complex cation by iodide were assigned to a mechanism involving the prior formation of ion pairs.<sup>39</sup>

They have been a number of studies aimed at resolving the rate at which the dye is regenerated, mostly for Ru(II) complexes. However, the use of transient absorbance to resolve the rate of cation interception does not give much information regarding the mechanisms of iodide oxidation at the surface of dye-sensitized TiO<sub>2</sub> electrodes.

The key parameters comprise the oxidation potential of the dye ( $S^+/S$ ), the charge of the TiO<sub>2</sub> surface as well as the ability of the dye to form an ion pair with iodide.

Iodide oxidation can be complicated by the presence of several reaction mechanisms, involving ion pairing at the surface of TiO<sub>2</sub> or with the dye. The details of the reduction reaction, involving two iodide ions, is described in more details within the introduction of chapter 4.

### Other than iodide

Several electrons donors other than iodide have been tested for DSSC operation. The major drawbacks of using a liquid electrolyte based on iodide are the potential leakages in devices and the corrosive nature of iodine.<sup>40</sup> The volatile electrolytes prepared (acetonitrile-based) have a volatility that can lead to these leaking problems, even in sealed systems and the corrosive nature of iodine precludes the use of inexpensive electrodes, but requires platinum electrodes.

Furthermore, there is a fundamental electronic loss in energy in the dye regeneration process which ultimately limits the maximum possible efficiency of the iodide based DSSC to  $\sim 15\%$ .<sup>33</sup> This is because the use of iodide induces a significant loss in free energy under standard conditions. It is assumed that the loss in an acetonitrile based electrolyte is almost as large as this standard value.

Therefore attention has been focused on replacing this liquid electrolyte with alternative redox systems.

Organic donors have been investigated. Phenothiazine donors are able to efficiently regenerate oxidized sensitizers. However, the recombination of the injected electrons with the oxidized phenothiazine is too fast to allow for an efficient transport of the holes to the cathode of a DSSC.

Several pseudo-halides mediators have also been investigated comprising  $(\text{SeCN})_2/\text{SeCN}^-$  or  $(\text{SCN})_2/\text{SCN}^-$ . Unfortunately, none of them proved being as efficient as iodide. The regeneration rate followed the order  $\text{I}^- > \text{SeCN}^- > \text{SCN}^-$ , when regenerating  $\text{N3}|\text{TiO}_2$ .

The radical tempo<sup>ii</sup> has been tested as a potential efficient mediator.<sup>41</sup> It is chemically oxidized by  $\text{NOBF}_4$  to generate a  $\text{tempo}^+/\text{tempo}$  redox couple in a 1:9 ratio, similarly to what is employed in iodide-based electrolytes.

A solid-state hole-transporter such as spiro-OMeTAD<sup>iii</sup> has also been broadly used for making devices.<sup>42,43</sup> Unfortunately, the interception reaction

<sup>ii</sup>2,2,6,6-tetramethyl-1-piperidinyloxy

<sup>iii</sup>2,2',7,7'-tetrakis(N,N-di-p-methoxyphenyl-amine)9,9'-spirobifluorene

in itself and its governing parameters has been only poorly investigated for this mediator.

Some cobalt complexes have also been used.<sup>44,45</sup> The interception of the dye oxidized state by the Co(II) complex in diluted electrolyte was found to exhibit a first order kinetics. Dynamics of the recombination reaction between the injected electron and the oxidized mediator is determined with a behavior close to that of the triiodide/iodide redox couple.

## 1.3 References

1. Pelet, S. *Femtosecond Dynamics of Electron Transfer in the Photosensitization of Wide Band Gap Semiconductors*, Thèse École Polytechnique Fédérale de Lausanne no. 2626, **2002**.
2. Wenger, B. *Effect of Electronic and Nuclear Factors on the Dynamics of Dye-to-Semiconductor Electron Transfer*, Thèse École Polytechnique Fédérale de Lausanne no. 3447, **2006**.
3. Moser, J. *Dynamique des réactions de transfert d'électrons induites par la lumière à la surface de semi-conducteurs colloïdaux*, Thèse École Polytechnique Fédérale de Lausanne no. 616, **1986**.
4. Lakowicz, J. R. *Principles of Fluorescence Spectroscopy*, 3rd edition, Springer, **2006**.
5. *Electron Transfer in Chemistry*, volumes 1, 4 and 5, Balzani Ed., Wiley-VCH, **2001**.
6. Moser, J.-E. *Dye Sensitized Solar Cells*, Chapter 11: *Dynamics of interfacial and surface electron transfer processes*, Kalyanasundaran K., Ed., EPFL Press, **2010**.
7. Ardo, S.; Meyer, G. J. *Chem. Soc. Rev.* **2009**, 38, 115–164.
8. Watson, D.; Meyer, G. *Annu. Rev. Phys. Chem.* **2005**, 56, 119–156.
9. O'Regan, B. C.; Moser, J. E.; Anderson, M.; Grätzel, M. *J. Phys. Chem-Us* **1990**, 94, 8720–8726.
10. O'Regan, B. C.; Grätzel, M. *Nature* **1991**, 353, 737–740.
11. Pelet, S.; Moser, J. E.; Grätzel, M. *J. Phys. Chem. B* **2000**, 104, 1791–1795.
12. Galoppini, E. *Coordin. Chem. Rev.* **2004**, 248, 1283–1297.
13. Nazeeruddin, M. K.; Kay, A.; Rodicio, I.; Humphry-Baker, R.; Muller, E.; Liska, P.; Vlachopoulos, N.; Grätzel, M. *J. Am. Chem. Soc.* **1993**, 115, 6382–6390.

- 
14. Nazeeruddin, M. K.; Zakeeruddin, S.; Humphry-Baker, R.; Jirousek, M.; Liska, P.; Vlachopoulos, N.; Shklover, V.; Fischer, C.; Grätzel, M. *Inorg. Chem.* **1999**, *38*, 6298–6305.
  15. Zakeeruddin, S.; Nazeeruddin, M. K.; Humphry-Baker, R.; Pechy, P.; Quagliotto, P.; Barolo, C.; Viscardi, G.; Grätzel, M. *Langmuir* **2002**, *18*, 952–954.
  16. Wang, P.; Zakeeruddin, S.; Exnar, I.; Grätzel, M. *Chem. Commun.* **2002**, 2972–2973.
  17. Snaith, H. J.; Karthikeyan, C. S.; Petrozza, A.; Teuscher, J.; Moser, J. E.; Nazeeruddin, M. K.; Thelakkat, M.; Grätzel, M. *J. Phys. Chem. C* **2008**, *112*, 7562–7566.
  18. Grätzel, M. *Accounts Chem Res* **2009**, *42*, 1788–1798.
  19. Kuang, D.; Klein, C.; Snaith, H.; Moser, J. E.; Humphry-Baker, R.; Comte, P.; Zakeeruddin, S.; Grätzel, M. *Nano Lett.* **2006**, *6*, 769–773.
  20. Kalyanasundaram, K. *Coord. Chem. Rev.* **1982**, *46*, 159–244.
  21. Tachibana, Y.; Moser, J. E.; Grätzel, M.; Klug, D. R.; Durrant, J. R. *J. Phys. Chem.-Us* **1996**, *100*, 20056–20062.
  22. Kallioinen, J.; Benkö, G.; Myllyperkiö, P.; Khriachtchev, L.; Skarman, B.; Wallenberg, R.; Tuomikoski, M.; Korppi-Tommola, J. E. I.; Sundström, V.; Yartsev, A. P. *J. Phys. Chem. B* **2004**, *108*, 6365–6373.
  23. Benkö, G.; Kallioinen, J.; Korppi-Tommola, J. E. I.; Yartsev, A. P.; Sundström, V. *J. Am. Chem. Soc.* **2002**, *124*, 489–493.
  24. Imahori, H.; Uneyama, T.; Ito, S. *Accounts Chem Res* **2009**, *42*, 1809–1818.
  25. Ito, S.; Miura, H.; Uchida, S.; Takata, M.; Sumioka, K.; Liska, P.; Comte, P.; Pechy, P.; Grätzel, M. *Chem. Commun.* **2008**, 5194–5196.
  26. Ning, Z.; Tian, H. *Chem. Commun.* **2009**, 5483–5495.
  27. Xu, M.; Wenger, S.; Bala, H.; Shi, D.; Li, R.; Zhou, Y.; Zakeeruddin, S.; Grätzel, M.; Wang, P. *J. Phys. Chem. C* **2009**, *113*, 2966–2973.
  28. Wiberg, J.; Marinado, T.; Hagberg, D. P.; Sun, L.; Hagfeldt, A.; Albinsson, B. *J. Phys. Chem. C* **2009**, *113*, 3881–3886.



- 
29. Tachibana, Y.; Umekita, K.; Otsuka, Y.; Kuwabata, S. *J. Phys. Chem. C* **2009**, *113*, 6852–6858.
30. Hyun, B.-R.; Zhong, Y.-W.; Bartnik, A. C.; Sun, L.; Abruna, H. D.; Wise, F. W.; Goodreau, J. D.; Matthews, J. R.; Leslie, T. M.; Borrelli, N. F. *Acs Nano* **2008**, *2*, 2206–2212.
31. Robel, I.; Kuno, M.; Kamat, P. V. *J. Am. Chem. Soc.* **2007**, *129*, 4136–4137.
32. Robel, I.; Subramanian, V.; Kuno, M.; Kamat, P. V. *J. Am. Chem. Soc.* **2006**, *128*, 2385–2393.
33. Snaith, H. J. *Adv. Funct. Mater.* **2010**, *20*, 13–19.
34. Anderson, S.; Constable, E.; Dareedwards, M.; Goodenough, J.; Hamnett, A.; Seddon, K.; Wright, R. *Nature* **1979**, *280*, 571–573.
35. Huber, R.; Moser, J. E.; Grätzel, M.; Wachtveitl, J. *J. Phys. Chem. B* **2002**, *106*, 6494–6499.
36. Kamat, P. V. *J. Phys. Chem. B* **2002**, *106*, 7729–7744.
37. Lanzafame, J.; Palese, S.; Wang, D.; Miller, R.; Muentner, A. *J. Phys. Chem-US* **1994**, *98*, 11020–11033.
38. Hirata, N.; Lagref, J.; Palomares, E.; Durrant, J. R.; Nazeeruddin, M.; Grätzel, M.; Censo, D. D. *Chem-Eur. J.* **2004**, *10*, 595–602.
39. Fitzmaurice, D.; Frei, H. *Langmuir* **1991**, *7*, 1129–1137.
40. Boschloo, G.; Hagfeldt, A. *Accounts Chem Res* **2009**, *42*, 1819–1826.
41. Zhang, Z.; Chen, P.; Murakami, T. N.; Zakeeruddin, S.; Grätzel, M. *Adv. Funct. Mater.* **2008**, *18*, 341–346.
42. Bach, U.; Lupo, D.; Comte, P.; Moser, J. E.; Weissortel, F.; Salbeck, J.; Spreitzer, H.; Grätzel, M. *Nature* **1998**, *395*, 583–585.
43. Saragi, T. P. I.; Spehr, T.; Siebert, A.; Fuhrmann-Lieker, T.; Salbeck, J. *Chem. Rev.* **2007**, *107*, 1011–1065.
44. Nusbaumer, H.; Moser, J. E.; Zakeeruddin, S.; Nazeeruddin, M.; Grätzel, M. *J. Phys. Chem. B* **2001**, *105*, 10461–10464.

45. Nusbaumer, H.; Zakeeruddin, S.; Moser, J. E.; Grätzel, M. *Chem-Eur. J.* **2003**, *9*, 3756–3763.

# Chapter 2

## Experimental section

### Graphical abstract



Superfluorescence cone and amplified white light

---

This chapter describes the main setup used in this work.

## 2.1 Femtosecond spectrometer

The femtosecond spectrometer used in this thesis was built by Serge Pelet during his thesis.<sup>1</sup> Some parts of it have been improved by Bernard Wenger during his thesis.<sup>2</sup> Finally, it has been further modified during the present work.

Two major experimental configurations are used for measuring ultrafast dynamics. A two color pump-probe experiment permits the very accurate measurement around time zero as well as allowing for a very sensitive signal due to its phase sensitive detection scheme using a lock-in amplifier. The second configuration uses a white-light-continuum (WLC) as the probe beam and therefore permits monitoring of wavelengths ranging from 500 to 700 nm simultaneously. However this experiment involves a double diode array detector which has a dynamic range that is much less sensitive than the lock-in detection. Consequently some temporal precision as well as absorbance change sensitivity is lost using this configuration. On the other hand, collection of such a data matrix containing at the same time wavelength and time dependant components permits deeper analysis by means of Singular Value Decomposition and Global fitting procedures.

### 2.1.1 Laser source

The source used is a Ti:Sapphire amplified femtosecond laser (CPA-2001, Clark-MXR) that runs at 1 kHz. Typical output beam has a pulse width of 120 fs with an energy of 950  $\mu$ J at the fundamental wavelength of 775 nm.

The oscillator is made of a self-mode-locked erbium doped fiber pumped by a telecommunication diode laser (980 nm) which exhibits a gain at 1550 nm. Among the many advantages of using this type of oscillator is the high stability of the pump laser which is relevant to our setup. The fiber produces pulses at 25.8 MHz. A frequency doubler converts the IR light to

red light at 775 nm. After passing through a stretcher, this beam constitutes the seed of the cavity.

The amplification is based on a chirped-pulse amplification design. This technique minimizes crystal damage but still allowing high intensities for ultrashort pulses. The amplification itself is done in a Ti:Sapphire crystal which is pumped by a frequency doubled Nd:YAG laser (7.7 W at 532 nm). The amplified pulses are picked out of the amplifier cavity at a frequency of 1 kHz, being the repetition rate of our experiment. A grating compressor permits the generation of pulses as short as 120 fs with an energy close to 1 mJ, centered at  $\lambda = 775$  nm.

### 2.1.2 NOPA

The source beam is split into three major beams. Half of the source intensity is used for pumping two similar NOPA's. The other half of the fundamental beam, pumps a broadband NOPA in order to produce an amplified WLC between 500 and 700 nm.

The pump and the one color probe of our experiments are produced by two non collinear phase matching optical parametric amplifiers (NOPA) pumped by 200  $\mu$ J of the fundamental. They are comprised of three main functional blocks. A small fraction of the fundamental is used for generating a continuum in a sapphire disk. This WLC (the seed beam) is then parametrically amplified in a  $\beta$ -Barium Borate (BBO) crystal pumped by the frequency doubled fundamental. A second stage amplifies the first stage output, using it as the seed beam, pumping a second BBO crystal. This scheme permits efficient tuning of the beams from 450 up to 1600 nm without any gap in spectrum with sub 50 fs pulse width after compression in prism pair.<sup>3</sup>

In general, the presented experiments involve a pump beam in the visible, typically tuned either at 530 nm or at 480 nm with a typical energy of 10  $\mu$ J per pulse. The probe beam lies in the orange, 600-650 nm (about 10  $\mu$ J per pulse), or in the near-infrared (NIR), either at 860 nm or at 1100 nm with

2-4  $\mu\text{J}$  per pulse. For the spectral region around the fundamental wavelength of the laser source (775 nm) a third stage is inserted between the two stages of the NOPA. This latter is used to generate a second continuum, centered in the NIR (typically 1100 nm) and therefore avoiding the modulations of the spectrum that are present around the fundamental wavelength of the laser. This allows for efficient amplification at 860 nm in the last stage of the NOPA. In this configuration, only one stage is used for the generation of the wavelength of interest. This is the reason for weaker pulses energies being attained using this scheme.

These outputs are systematically compressed by a pair of SF10 prisms down to at least 50 fs.

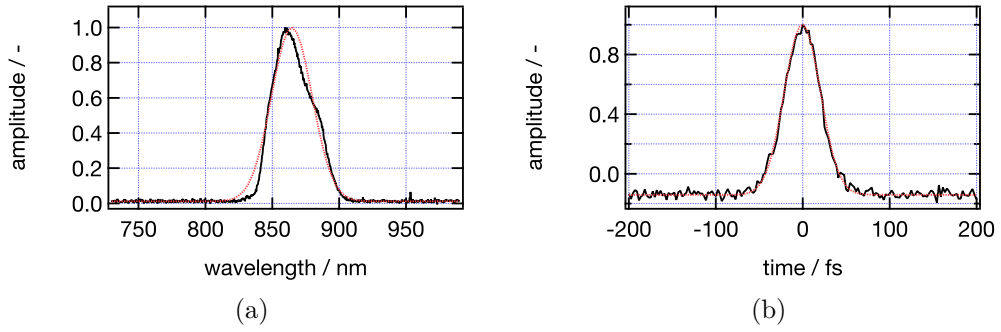


Figure 2.1: Typical spectral and temporal shape of a pulse at the output of a NOPA. (a) Spectral profile of a pulse centered at 860 nm measured with a dual-channel spectrometer (S2000, Ocean Optics) (—), gaussian fit (---), FWHM = 35 nm. (b) Temporal profile of the same 860 nm pulse after compression with a pair of SF10 prisms measured with an intensity autocorrelator (AC150, Clark-MXR) (—), gaussian fit (---), FWHM = 48 fs.

### 2.1.3 White-light-NOPA

This part of the setup has been developed during this thesis. The home-built broadband NOPA is based on a configuration proposed by Manzoni et al.<sup>4</sup> Unlike the pump for which a narrow bandwidth is desired for selective

excitation of an optical transition of the sample, the probe pulse should be as short as possible and might therefore be broader in the energy domain.

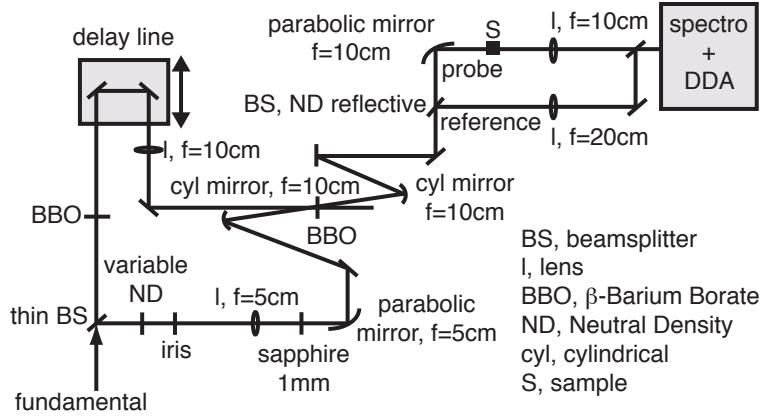


Figure 2.2: Detailed scheme of the home-built broadband NOPA and the detection scheme of the spectrometer.

The white-light NOPA is pumped by half of the output of the laser source. 500  $\mu\text{J}$  of 775 nm light are split in two parts with a 92:8 thin beamsplitter as shown on figure 2.2.

The intense part is then sent to a 0.7 mm thick BBO crystal cut for type-I SHG at 775 nm ( $\theta = 30^\circ$ ). The latter is slightly tilted for optimising the phase matching. Resulting yield is close to 30 %. This UV (387 nm) beam is then separated from the remaining transmitted fundamental light by two dielectric mirrors. These mirrors reflect the UV component but let the remaining fundamental pass through. This trick permits efficient color filtering without the use of a bandpass coloured filter<sup>i</sup> which would have had the disadvantage of adding a chirp to the UV pulse. This filtering module is mounted on a short manual delay line and will therefore be used for adjusting the time overlap between the pump and the WLC seed as well.

The weaker beam passes through a variable neutral density filter, an iris and a 5 cm focal length lens. This allow to focus less than 2  $\mu\text{J}$  of the light

<sup>i</sup>A Schott BG 40 filter that has a transmission of more than 60 % from 350 to 600 nm and 0 % from 700 to 1200 nm

onto a 1 mm sapphire plate. Careful control of the energy incident to the plate permits the generation of a stable single filament WLC. The damage threshold of the sapphire plate is high, permitting operation without any translation of the crystal, thus increasing the stability of the generated beam. From this point of the NOPA, only reflective optics are used for guiding the WLC to avoid the introduction of any additional chirp.<sup>5</sup>

Parametric amplification is achieved in a 1 mm thick BBO cut at  $32^\circ$  (type-I). This angle is chosen for giving the broadest phase matching bandwidth for the non-collinear type-I interaction geometry.<sup>4</sup> This crystal is placed perpendicular to the pump light and therefore produces a strong superfluorescence cone as depicted in figure 2.3. The seed-to-pump angle is then adjusted for matching the apex angle of the cone. This requires an angle between the pump and seed beams to be close to  $3.7^\circ$ .<sup>6</sup> The seed is focused onto the BBO with a cylindrical mirror ( $f = 10$  cm).



Figure 2.3: Picture of the superfluorescence cone with the red components outside and the green inside, amplified WLC just after the amplification (left bright white spot) and the IR idler (right pale spot).

The amplified WLC thus obtained is collected (left white spot of figure 2.3) by a second cylindrical mirror ( $f = 10$  cm) which collimates the beam again. A residual astigmatism is always present in the WLC after all and has never been fully compensated. This will induce a probe beam at the sample



focus having more the shape of a small slit than a round point. In addition, no compression is performed on the WLC and it is therefore directly used as the probe for our experiment.

The typical white light has an intensity profile that renders it useful between 500 and 700 nm as shown in figure 2.4.

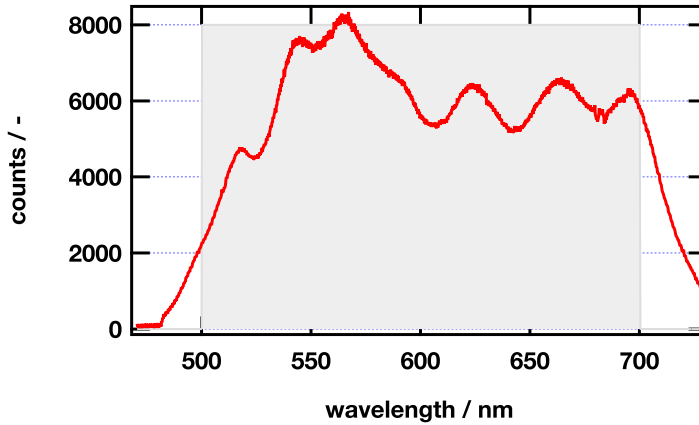


Figure 2.4: WLC spectrum recorded with one of the two diode array. The grey background highlight the usable range.

### 2.1.4 Labview integration

All components of the femtosecond laser setup are coupled together by a Labview (National Instruments) software. It controls and synchronises the different steps of the acquisition process.

### 2.1.5 Determination of the beam fluence

The fluence is the energy that reaches the sample on a given area. It is therefore expressed in units of  $\mu\text{J}\cdot\text{cm}^{-2}$ .

Dye-sensitized samples may be rather fragile and their photodegradation might be accelerated under intense illumination. Several experiments report degradation of the samples during the data acquisition or the appearance of early dynamics induced by a high fluence.<sup>7-9</sup>

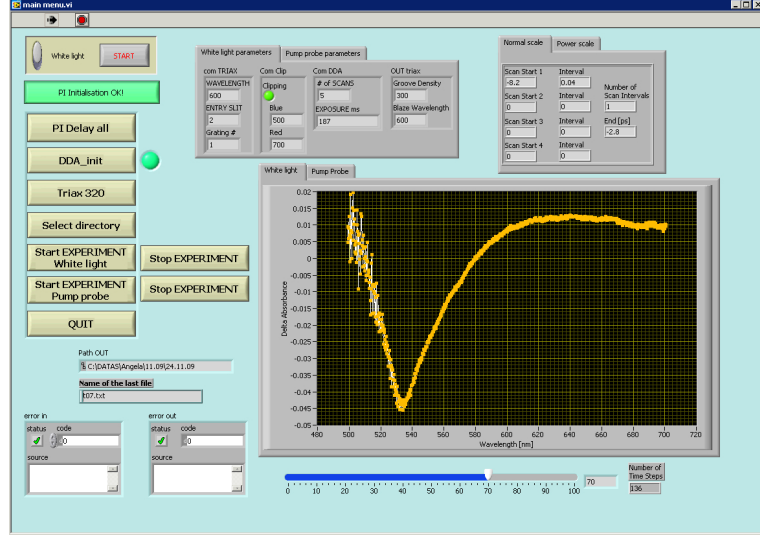


Figure 2.5: Front panel of the Labview software in the middle of the acquisition of a WLC spectrum. The upper right tab recall the time parameters, the central tab is a summary of the acquisition parameters (detector exposure time, averages), the left buttons are the main functions of the software. A progress bar informs the user about the degree of completion of his experiment.

Characterization of the pulse energy is straightforward by measuring the beam power with a powermeter (Lasermate-1, Coherent) and dividing it by the repetition frequency of the laser.

Measurement of the beam diameter is achieved with a knife-edge technique referenced in Skinner et al.<sup>10</sup> A razor blade is translated with the help of a micrometer over the laser beam at the sample position. The power of the beam is measured after the blade with steps of 10  $\mu\text{m}$  of the razor blade passing through the optical pathway.

$$P = \frac{1}{2} \cdot P_0 \cdot \text{erf} \left( \frac{\sqrt{2} \cdot (x - x_0)}{w} \right) \quad (2.1)$$

Relation 2.1 allows the determination of the  $w$  parameter, the gaussian radius of the beam, from the measurements of  $P_0$  and  $P$ , the full power and the series of attenuated power, respectively.  $x$  is the displacement of the blade and  $x_0$  is the position value at the inflexion point and erf denotes the

error function. The beam diameter is defined as  $2 \cdot w$ .

Figure 2.6 gives an example of the measurement of the beam diameter with the knife-edge technique.

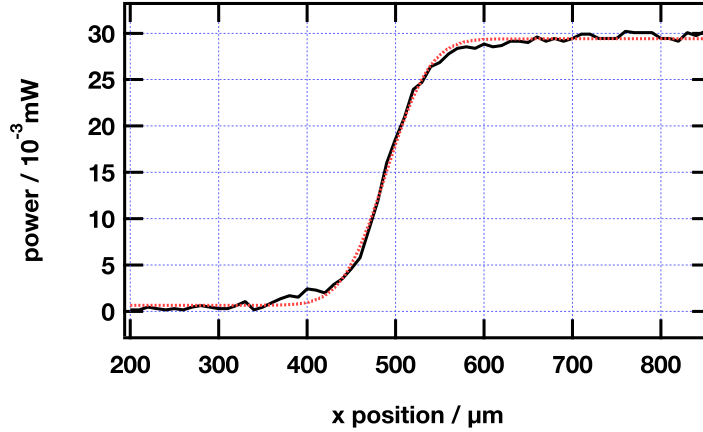


Figure 2.6: Knife-edge measurement on a  $\lambda = 675 \text{ nm}$  pulse prepared as a probe (—). Result of the fit following equation 2.1 (---). The beam diameter is  $156 \mu\text{m}$ .

Typical two color pump-probe measurements in this work are performed with beam diameters of  $150 \mu\text{m}$  for the probe and  $250 \mu\text{m}$  for the pump. With typical pulse energies of about  $0.2 \mu\text{J}$  at the sample, this leads to fluences of  $1131 \mu\text{J} \cdot \text{cm}^{-2}$  for the probe and  $407 \mu\text{J} \cdot \text{cm}^{-2}$  for the pump. This latter value corresponds to about 10 injected electrons per nanoparticle for a typical ruthenium dye-sensitized  $\text{TiO}_2$  sample (calculation leading to this result is presented in details in chapter 4).

### 2.1.6 Two color pump-probe transient absorbance

One configuration of the experimental setup is the two color pump-probe transient absorbance spectrometer. In this scheme, a first short excitation pulse, known as the pump, induces a transient response to a sample. This time dependance is then probed by a second short pulse (the probe) which has been delayed in time with respect to the pump. This is physically achieved by changing the relative path length of the two beams. The two pulses are

the output of the two NOPAs described in section 2.1.2. Time limit of this technique is only limited by the duration of the laser pulses and not by the time response of the detector.

A path length change as short as  $1 \mu\text{m}$  can be achieved with our setup ( $2 \cdot 0.5 \mu\text{m}$ ), corresponding to 3.33 fs according to relation 2.2 and considering that  $n_{\text{air}} \approx 1$  and  $c \approx 3 \cdot 10^8 \text{ m}\cdot\text{s}^{-1}$ .

$$\Delta t = \frac{n \cdot l}{c} \quad (2.2)$$

Delay lines are mounted on both the pump and the probe optical paths introducing the time scale of our setup. They are controlled by the acquisition software (see details in section 2.1.4) and are configured for time steps as short as 10 fs. As shown on figure 2.7 it will be achieved with a  $1.5 \mu\text{m}$  displacement of the translation stage (M521.PD, Physik Instrumente) placed within the probe beam path. This allows for delays up to 2 ns. This stage is driven by a 4 channel C-843 DC-Servo-Motor Controller PCI board.

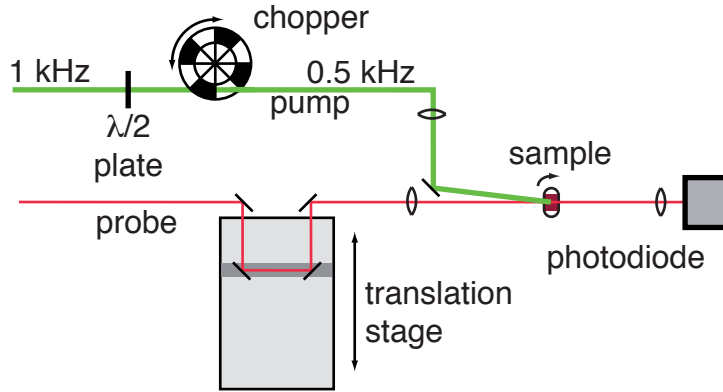


Figure 2.7: Scheme of the pump-probe configuration. The pump beam (green) polarity is rotated at the magic angle ( $54.7^\circ$ ), respectively to the probe beam (red). The repetition rate of the pump is divided by two and the beam is focused onto the sample. The probe beam passes through a translation change, providing the time resolution of the setup. It is then focused onto the sample and well overlapped with the probe. A photodiode records the probe pulses, which are analysed by a lock-in amplifier, locked to the mechanical chopper.

Transient absorbance measurement records the change in transmission of the probe pulse induced by the transient species present in the sample. This is practically achieved by chopping the pump pulse at half the repetition frequency of the laser source with a mechanical chopper triggered by the laser (MC1000A, Thorlabs). This scheme lets exactly one pulse out of two of the pump to pass through the sample and therefore a direct comparison, alternating between the transmission at steady-state and the transient one induced by the pump pulse.

The sample is continuously rotated during an acquisition and might also be translated vertically and horizontally (home-made sample holder). The polarization of the pump relative to the probe is adjusted at  $54.7^\circ$ , the magic angle, with the help of a  $\lambda/2$  waveplate to avoid artifacts. The pump and the probe are focused onto the sample with fused silica lenses ( $f = 10$  cm for the probe, 25 cm for the pump). This scheme induces some chirp in both pulses and therefore lengthens the instrument time response. Systematically, the pump beam focus is adjusted not to be at the plane of the sample for two main reasons. At first the pump beam has to homogeneously overlap the probe beam for a better response. Secondly, defocusing the pump is a way of lowering the fluence. This is practically achieved by positioning the lens on a translational stage.

After passing through the sample, the pump beam is blocked and coloured glass filters are introduced to remove any potential scattered light before the detector.

The change in transmittance of the sample is measured by a photodiode (Nirvana detector, New Focus, model 2007 for the visible and 2017 for the NIR used as single photodiodes) placed directly after the sample. The signal is extracted by a lock-in amplifier (SR-830, Stanford Research) referenced to the chopper at half the repetition frequency of the pulsed laser source. The lock-in is set with a time constant of 1 s, a 24 dB/octet slope and at a high reserve sensitivity. The phase is adjusted for Y (the out-of-phase component) being close to zero so X (the in-phase signal) can be used as the

difference between the transmitted intensity with and without the pump. As a consequence, if an unwanted process affects the transient, such as a time-dependant misalignment affecting the spatial overlap between the probe and the pump across time, a drift from zero of Y will be present in the recorded transient data and alert the user.

The buffer of the lock-in works at 128 Hz and typically accumulates 0.5 to 1 s before sending the values to the computer via a GPIB<sup>ii</sup> board. These values are then averaged by the acquisition software and the result is stored with its corresponding time value. A dwell time of at least four times the integration constant of the lock-in is introduced between each point for improving accuracy of the measurement.

### Data acquisition and treatement

The X value of the lock-in amplifier expresses only a relative transmission change and therefore does not allow for quantitative measurement directly. Nevertheless it is proportional to the absorbance change of the sample induced by the pump according to the following development.

Transient absorbance change is defined as :

$$\Delta A = -\log\left(\frac{I_t}{I_0}\right) = -\log\left(\frac{\Delta I + I_0}{I_0}\right) \quad (2.3)$$

$I_0$  is the intensity of the transmitted light without the pump and  $I_t$  with the pump. X value of the lock-in at 500 Hz ( $X_{500}$ ) is proportional to the difference between the intensity of the probe monitored by the diode with the pump and without the pump :

$$X_{lock-in} \propto \Delta I = I_t - I_0 \quad (2.4)$$

Applying the following mathematical relations :

$$\ln(x + 1) \rightarrow x \quad , \text{ for } x \rightarrow 0 \quad (2.5)$$

---

<sup>ii</sup>IEEE-488, General Purpose Interface Bus

$$2.3 \cdot \log(x + 1) \rightarrow x, \text{ for } x \rightarrow 0 \quad (2.6)$$

It is therefore possible to show the relationship between  $\Delta A$  and  $X$ :

$$\Delta A = -\log\left(\frac{\Delta I + I_0}{I_0}\right) = -\log\left(\frac{\Delta I}{I_0} + 1\right) \approx -\frac{1}{2.3} \cdot \frac{\Delta I}{I_0} = \alpha \cdot \Delta I \quad (2.7)$$

$$\Rightarrow \Delta A \propto \Delta I \propto X_{lock-in} \quad (2.8)$$

If a quantitative measurement is needed, it is although possible to resolve it by the means of measuring the full range signal at 1 kHz without the pump as depicted in equation 2.9. This is measured by triggering the lock-in amplifier directly by the laser source and by measuring the amplitude of the signal without any pumping.

$$\Delta A = -\log\left(\frac{X_{500} + X_{1000}}{X_{1000}}\right) \quad (2.9)$$

Figure 2.8 indicates that the approximation made here above is correct and may be applied on our experiments. After normalization,  $\Delta A$  and  $X$  indeed superimpose perfectly.

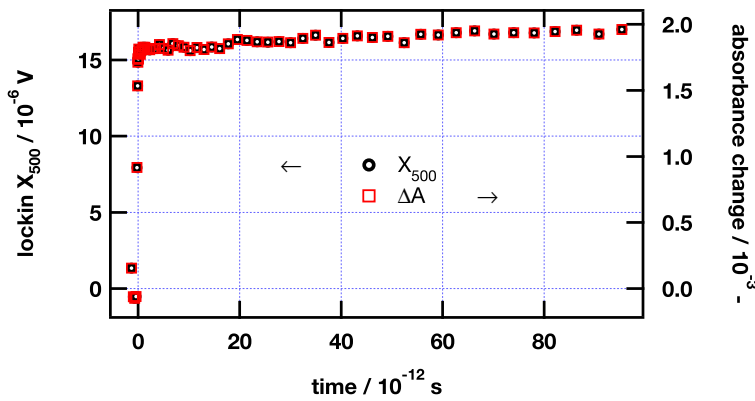


Figure 2.8: Femtosecond transient absorbance,  $\lambda_{obs} = 860$  nm,  $\lambda_{ex} = 530$  nm, N719/TiO<sub>2</sub> in MPN; Comparison of  $X_{500}$  (○) and  $\Delta A$  (□) absolute values. No difference is observed.

Such obtained datas are fitted with an analytical convolution of a Gaussian instrument response and n exponential decays (or rises).

$$\sum_{i=1}^n \left( \frac{A}{2} \cdot \exp\left(-\frac{t}{\tau_i}\right) \cdot \exp\left(\frac{1}{\tau_i} \cdot \left(\mu + \left(\frac{\sigma^2}{2 \cdot \tau_i}\right)\right)\right) \cdot \left(1 + \operatorname{erf}\left(\frac{\left(t - \left(\mu - \frac{\sigma^2}{\tau_i}\right)\right)}{\sqrt{2} \cdot \sigma}\right)\right) \right) \quad (2.10)$$

Equation 2.10 is derived from the global fitting proposed by van Stokkum et al. in his lecture notes.<sup>11</sup>  $\mu$  and  $\sigma$  represent, as usual, the center and the width of the gaussian function, respectively. A negative amplitude (A factor) will be then used if a subsequent slower rise after the ultrafast response of the instrument is observed.

The global fitting analysis procedure as well as different file handling tools have been implemented into a series of Igor Pro (Wavemetrics) functions and macros.

### Instrument response

The parameters of the gaussian function of the fitting equation have to be derived from the instrument response. The cross-correlation time between the pump and the probe pulses is measured at the sample position and is used for this purpose.

A Kerr gating technique is used to measure the temporal overlap of the pulses. The relative polarization of the probe and the pump is set to 45° for favouring non-linear optical Kerr effect. Both beams are focused and spatially overlapped onto a thin glass plate (0.15 mm), alternatively a SF10<sup>iii</sup> (0.3 mm) window, which are used as the Kerr media. The probe passes through a Glan-Thompson polarizer positioned at normal angle to the beam after the plate, i.e. it blocks the probe beam.

When the pump and the probe are temporally overlapped, the birefringence induced by the pump slightly rotates the polarization of the probe. As a consequence, the latter partially passes through the polarizer and this change

---

<sup>iii</sup>Schott SF10 Glass



in amplitude can be detected by a diode connected to the lock-in amplifier. The short lifetime of the birefringence hence enables rotation of the probe beam polarization only when both pulses temporally overlap. During such a measurement, the lock-in is triggered at the laser repetition frequency while the pump beam is not chopped.

Figure 2.9 shows a typical instrument response obtained measuring the cross-correlation between the pump and the probe.

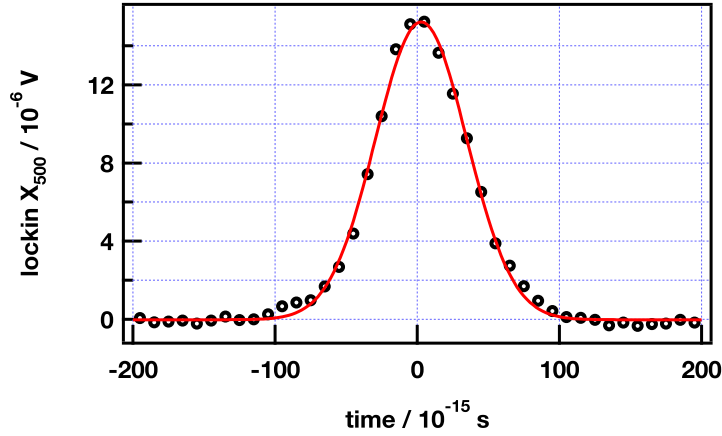


Figure 2.9: Cross-correlation obtained by optical Kerr gating in a thin glass window (O).  $\lambda_{obs} = 860$  nm,  $\lambda_{ex} = 530$  nm. The line (—) represents a gaussian fit of the data with a FWHM = 75.6 fs.

### 2.1.7 Pump-white-light-continuum-probe transient absorbance

The second experimental configuration is the pump-white-light-continuum-probe transient absorbance spectrometer. The scheme uses the same principles as reported in previous section, a first short excitation pulse, known as the pump, induces a transient response in a sample. This time dependence is then probed by a second short pulse (the probe), which is spectrally a WLC.

In this configuration, the pump beam is not chopped anymore as the detector used is not able to measure a single pulse response. As

a consequence, the signal without the pump is averaged over a certain acquisition time, giving the value for  $I_0$ . Then a home-made pneumatic shutter opens the pump pathway. A second acquisition then measures  $I_t$ .

As depicted on figure 2.2, the WLC is split into two beams by a neutral density (ND) reflective filter (60 % reflectance). The reflected beam constitutes the probe (to avoid introduction of additional chirp) and the second a reference beam that balances the acquired signal. The polarization of the pump relative to the probe is adjusted at  $54.7^\circ$ , the magic angle, with the help of a  $\lambda/2$  waveplate to avoid artifacts. The pump is focused onto the sample with a fused silica lens with  $f = 25$  cm. The pump beam is applied onto the sample in a similar manner as in the two color configuration except that the time delay stage (M531.PD, Physik Instrumente) is located on the pump beam in this configuration. The probe is focused onto the sample by a parabolic mirror ( $f = 10$  cm) to avoid the introduction of an additional chirp with the WLC.

After the sample, achromatic lenses are used for collimating the WLC and focusing it onto the spectrograph slits according to its F number ( $F/4.1$ ) and focal length (320 mm) (TRIAX 320, Jobin Yvon Horiba). This imaging spectrograph is equipped with a grating of 300 grooves per millimeter and a blaze wavelength of 600 nm. The WLC amplitude is measured on a cooled ( $-40^\circ\text{C}$ ) double diode array detector (DDA; ST-116, Princeton Instruments) which is coupled at the output of the spectrograph. The detector arrays has 1024 pixels each. They are usually exposed for 100 to 200 ms and scanned five times.

For measuring the real absorbance change, the measurement is taken with the pump and sequentially without the pump. The absorbance change can be easily calculated applying relation 2.11.  $I_{0p}$  is the intensity of the probe without the pump,  $I_p$  is the intensity of the probe with the pump,  $I_{0r}$  is the intensity of the reference without the pump and  $I_r$  is the intensity of the reference with the pump. This scheme for acquiring a reference in parallel is the best design for compensating for WLC fluctuations.<sup>12</sup>

$$\Delta A = \log \left( \frac{I_{0p} \cdot I_r}{I_p \cdot I_{0r}} \right) \quad (2.11)$$

This measurement is then typically averaged over five times to obtain a satisfactory signal-to-noise ratio.

### Data acquisition and treatment

The transient matrices obtained can be displayed in a 3D plot showing the absorbance change as a function of time and wavelength (figure 2.10). The saved file contains absolute values of transient absorbance change calculated according to equation 2.11, related to a certain wavelength at a certain time. A collection of Igor Pro functions and macros permits efficient data handling with automated procedures for file handling and then spectral background subtraction, wavelength number reduction, scaling of the matrices, singular value decomposition (SVD) analysis and a global fitting procedure.

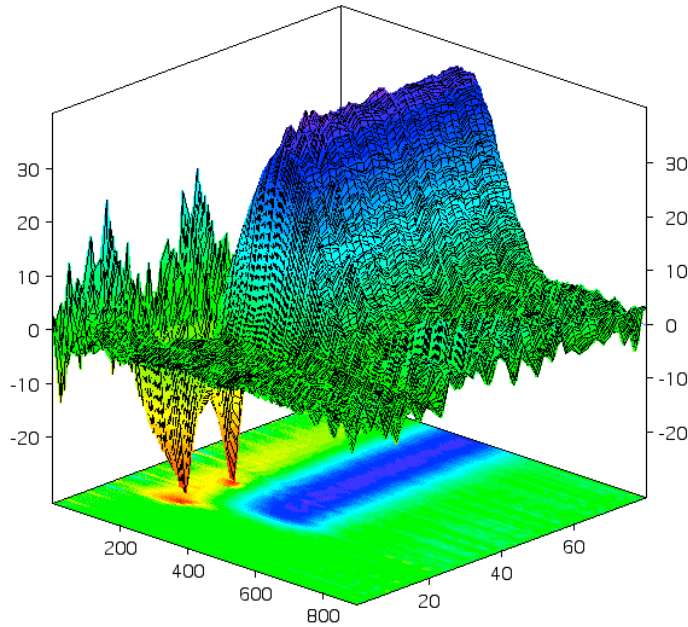


Figure 2.10: Typical raw data matrix displayed as a 3D surface.

A typical analysis of a data matrix starts by wavelength number

reduction. Commonly, the matrix is smoothed over 50 to 100 wavelengths for a more convenient handling (figure 2.11(b)). Then SVD is applied.

**Singular Value Decomposition** This purely mathematical technique permits an efficient data cleaning, removing many unwanted components of the matrix consisting of noise. The data matrix  $M$  is decomposed into the product of three matrices.

$$M = U \Sigma V^{-1} \quad (2.12)$$

The diagonal values in matrix  $\Sigma$  are the singular values of the matrix  $M$ , they are therefore an amplitude that will multiply their associated wavelength and time base vectors and are therefore arranged in descending order. The rows of  $V^{-1}$  form a set of time base vectors and the columns of  $U$  form a set of wavelength base vectors. This is a decomposition into linearly independent information.<sup>13</sup>

The number of singular values greater than 0 is equivalent to the rank of the matrix  $M$  and in a transient spectroscopy analysis. This determines the number of base spectra and base time traces necessary for a correct description of the recorded data. In a model case, every exponential component of a transient defines a linearly independent vector of  $M$ .<sup>13</sup>

But in practice, with real data, the rank of the matrix cannot be determined unambiguously and therefore the decision of what are the significant singular value is extremely difficult. The choice of the number of singular values retained as non-zero is based on three empirical considerations. First, the relative amplitude is crucial for retaining one value. Second, the wavelength base vectors are carefully observed for making sure that no vector with a clear and smooth behavior is being rejected. Finally the same analysis is performed onto the time base vectors.

Figure 2.11 shows typical data reduction of a transient spectrum by SVD. Noteworthy figures 2.11(c) and 2.11(d) are the reconstructed matrices with one and three non-zero singular values, respectively. It is clear on this

example that adding two more components adds a time dependant behavior of the spectrum that allows for a more accurate representation of the original transient matrix.

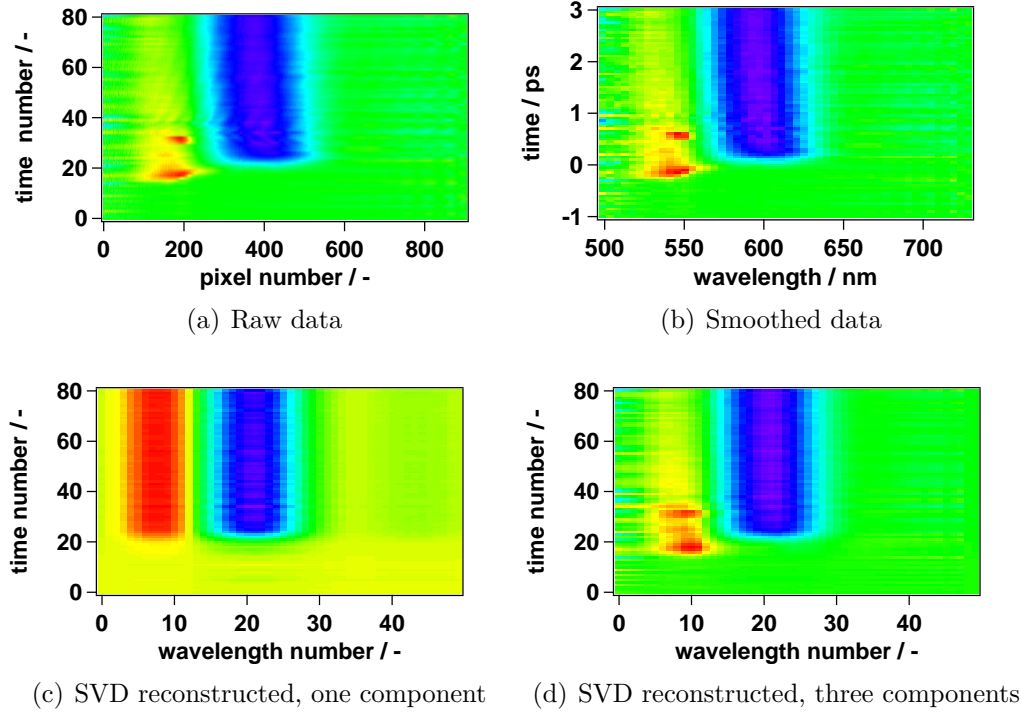


Figure 2.11: Example of a Singular Value Decomposition, (a) Raw data of a pump-white-light-continuum-probe transient absorbance experiment, (b) Smoothed matrix over the wavelengths, 50 wavelengths components, (c) Reconstructed matrix considering a rank 1, only one singular value is non-zero, (d) Reconstructed matrix considering a rank 3, three singular values are non-zero.

**Global fitting** After SVD data reduction, global fit of the data is performed. This consists of fitting the data with the same analytical convolution of a gaussian instrument response and  $n$  exponential decays (or rises) used for the pump-probe experiment, equation 2.10. In this case the desired function is fitted with a link of the time parameters ( $\tau$ 's of the exponentials) across the different wavelengths. This permits

association of a specific amplitude to each wavelength, related to a single time constant. These amplitudes enable plotting a decay associated spectrum, i.e. a spectrum of a species related to a specific lifetime.

### Instrument response

One need to know the instrument response in the case of WLC probe for two reasons. First, and as for the unicolor probe case, the parameters of the gaussian function of the fitting equation have to be derived from the instrument response. Second, the chirp needs being corrected for short times measurements as it can be as wide as 500 fs in our setup design.

The cross-correlation time between the pump and the probe pulses is measured at the sample position, with an experimental operational setup, using the same Kerr gating technique that was described in section 2.1.6. In this case, it is acquired via the DDA coupled to the spectrometer and, hence, is resolved in wavelength. Due to its broad spectral width, as a consequence of the pulse not being compressed, the WLC has a strong positive group velocity dispersion (GVD). This means the red wavelengths propagate in front of the pulse and the blue wavelengths at the rear of it. Therefore, it is difficult to define a time zero valid over the whole spectrum if the time step width is shorter than the chirp of the WLC pulse. Figure 2.12(a) shows a typical instrument response obtained by measuring the cross-correlation between the pump and the WLC-probe. It clearly shows that some 700 fs separate both ends of the pulse spectrum.

For overcoming this defect of the setup, a mathematical correction of the data is applied for the shortest measurements. This is achieved by fitting every wavelength component of the Kerr response with a gaussian function. This gives us two main pieces of information. First, the width of each gaussian provides us the instrument response for each wavelength. Being typically shorter than 100 fs, this value is always wavelength-dependant. Secondly, the location of the minimum of every gaussian, reported versus the wavelength permits efficient reconstruction of the pulse front, as shown in

figure 2.12(b).

This is achieved by fitting the front pulse obtained with the gaussian information with an exponential function and then reconstructing a new time corrected matrix by linear data interpolation. This technique allows for efficient correction of the chirp and makes the information contained in the leading edge of the transients meaningful. Nevertheless, it cannot achieve a time measurement as precisely as the two color pump-probe configuration.

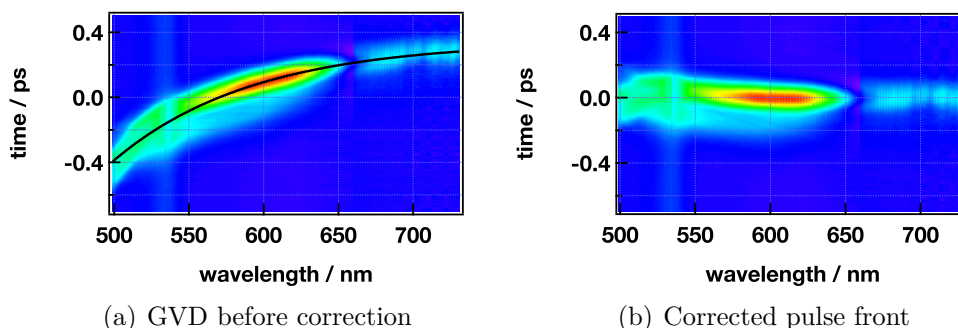


Figure 2.12: Typical chirp of a WLC, (a) GVD of a typical WLC, superimposed black curve is a monoexponential fit of the minimum of the gaussian at each wavelength, (b) Typical corrected chirps of a WLC, time zero has been fixed at 600 nm.

## 2.2 Nanosecond laser flash photolysis, transient absorbance spectroscopy

Flash photolysis is a pump-probe technique developed in the late forties by Ronald George Wreyford Norrish and George Porter, who won the 1967 Nobel Prize in Chemistry for this invention together with Manfred Eigen<sup>iv</sup>.

The sample is primarily excited by a relatively energetic nanosecond laser pulse. This light pulse induces a change in the electronic configuration that

<sup>iv</sup>The Nobel Prize in Chemistry 1967: "for their studies of extremely fast chemical reactions, effected by disturbing the equilibrium by means of very short pulses of energy"

can lead to a photochemical reaction. A continuous light beam, probes the sample and allows for the recording of a transient trace related to the optical perturbation. This is in practice recorded with an oscilloscope measuring the transient response of a photodiode or photo-multiplier tube.

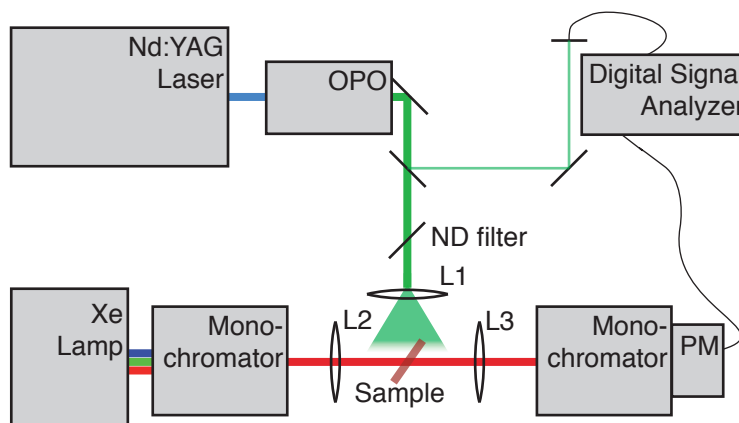


Figure 2.13: Nanosecond laser flash photolysis setup. A Nd:YAG laser pumps an Optical Parametric Oscillator (OPO). This tunable light is attenuated by a neutral density (ND) filter and used as the pump of the experiment. It is then dispersed by plano-concave lens L1 for a better spread over the sample. A perpendicular light beam is produced by a Xe arc-lamp, passes through a monochromator, is focused by plano-convex lens L2 on the sample, collimated by a second plano-convex lens L3, passed through a second monochromator and finally detected by a photo-multiplier tube (PM). The signal is acquired by a digital signal analyser. The latter is triggered synchronously to the pulsed laser by a fast photodiode.

Figure 2.13 presents a scheme of the setup used in the framework of this thesis. An optical parametric oscillator (OPO, GWU-350) is pumped by a Continuum Powerlite 7030 frequency-tripled Q-switched Nd:YAG laser ( $\lambda=355$  nm, 30 Hz repetition rate, 3 W). The output of the OPO (5 ns FWHM) is typically tuned between 450 and 650 nm. This beam is attenuated down to a fluence of less than  $30 \mu\text{J cm}^{-2}$  before the sample for avoiding unwanted effects due to large intensities. The output of a Xenon arc-lamp, filtered through a monochromator and various filters, constitutes the probe beam. It is focused onto the sample and then collected in a second monochromator. Both monochromators are tuned at the desired probe



wavelength. The photo-detection is finally achieved by a fast photomultiplier tube (R9110, Hamamatsu) supplied with 750 V. The induced transient voltage signal is then recorded into a digital signal analyser (DSA 602 A, Tektronix).

A typical acquisition requires averaging of 2500 laser shots to obtain satisfactory signal to noise ratio. At the running frequency of the laser, 30 Hz, this represents typical acquisition time of one to two minutes. Data analysis is then performed by a series of Igor Pro macros that load and process the data. A sensitivity of  $10^{-4} \Delta A$  is commonly achieved.

## 2.3 Photoinduced absorption spectroscopy

Photoinduced absorption (PIA) spectroscopy is used to study states which are not emissive and have relatively long lifetimes. These states are produced through photoexcitation and probing through the sample permits to identify transient states that absorb this probe with a characteristic spectrum.<sup>14,15</sup>

It is a quasi-steady-state technique which uses a modulated excitation source, associated to a lock-in amplifier, i.e. phase sensitive, detection. The scheme of the setup is depicted in figure 2.14.

In the setup used in this study, the pump is a diode (Lumiled Luxeon Star/O, Philips) with a center emission at either 470, 500, 535, 595 or 635 nm. The internal clock of the lock-in (SR-830, Stanford Research) is used to drive the diode pulses repetition rate, typically at 9 Hz. The light is focused onto the sample with an approximate intensity of  $6 \text{ mW}\cdot\text{cm}^{-2}$ . An alternative pump source that can be used is provided by a Kr-ion laser centered at 568 nm (Innova 200 Kr, Coherent). In this latter case, the clock of the experiment is not the lock-in anymore but a chopper wheel that modulates the laser light output. This chopper then serves as the master clock of the experiment and triggers the lock-in.

The probe beam is provided by a halogen light bulb (10 W) attenuated with metal mesh filters (approx. 0.1 % transmittance). The light intensity

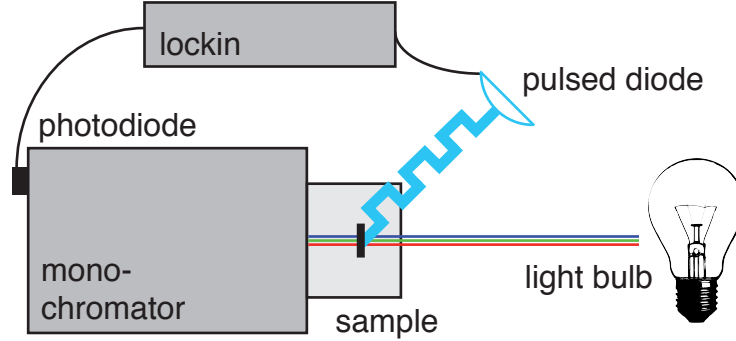


Figure 2.14: Photoinduced Absorption (PIA) spectroscopy setup. An emissive diode driven by the lock-in amplifier excite the sample. It is then probed by the white light of a halogen light bulb. The probe light passes through a monochromator and is then detected by a photodiode and acquired by the lock-in amplifier. A scan of the spectral domain permits acquisition of a spectrum from 300 up to 1650 nm.

on the sample is approximately  $65 \mu\text{W}\cdot\text{cm}^{-2}$ . This low probe intensity only represents therefore a very small bias to the sample and the steady-state it induces can be neglected. The probe light is then imaged on the slits of a monochromator (Gemini-180). The detector is a cooled dual colour solid-state Si/InGaAs photodiode mounted on the exit slits of the monochromator. This design allows for collecting spectra from 300 up to 1650 nm over a single scan.

Besides being the master clock of the experiment, the lock-in amplifier is also used to acquire the AC signal from the detectors. This component of the signal oscillates at the frequency of the modulated pump. This process discards noise at frequencies other than the modulation frequency. It is possible with this setup configuration to collect the signal in-phase with the modulation which provides the change in transmission,  $\Delta T$ . A transient positive absorbance then appears as a negative change in transmission.

At the same time, the DC value on the photodiode signal is recorded and is proportional to the absolute transmittance ( $T$ ). It permits to calculate

$-\Delta T/T$  which will be retained for presenting the data. Simultaneous recording of the phase also permits to get information about the origin of the signal recorded. Typically, a  $0^\circ$  phase signal will be associated to an emission process and a  $\pm 180^\circ$  will be attributed to a transient species.

The sample is kept in air during the experiments or in the desired solvent.

All experiments are controlled using a home-made software that runs in Igor Pro. The different experiment elements are linked through GPIB connections.

## 2.4 Steady-state UV-visible absorption and emission spectroscopies

Spectral characterizations of the samples have systematically been carried out on the following setups :

- UV-Vis absorbance spectroscopy. A Cary 1E (Varian) UV-Vis spectrometer is used. It is controlled by the Cary WinUV software.
- Luminescence spectroscopy. A LS 50 (Perkin-Elmer) fluorescence spectrometer is used. It is controlled by the FL Winlab software.

## 2.5 Sample preparation

### 2.5.1 Dyes

Dye solutions are systematically kept in the dark. Both ruthenium complexes and organic dyes used in this thesis are synthesized in house or provided by collaborating groups. Details on their compositions and characteristics will be specified in the respective chapters.

### 2.5.2 Titanium dioxide

The substrate used in this thesis consists of a mesoporous layer of anatase  $\text{TiO}_2$ , also called titania, which is deposited onto a glass substrate by doctor blading.<sup>16</sup> A paste containing  $\text{TiO}_2$  16 nm diameter particles (14 wt%), a polymer (ethyl cellulose) and various additives are used. Upon calcination at 470 °C for about 25 minutes, the resulting layer has a controlled thickness of 2.7 to 10  $\mu\text{m}$ , with a porosity of 0.625.

### 2.5.3 Alumina

Alumina ( $\text{Al}_2\text{O}_3$ ) layers of 4 to 8  $\mu\text{m}$  are deposited on a glass substrate in a manner similar to  $\text{TiO}_2$  layers. The paste used for the doctor blading procedure is composed of  $\text{Al}_2\text{O}_3$  6.4 nm diameter nanoparticles (18 wt%), a polymer (hydroxypropyl cellulose 100'000) and various additives. Upon deposition, the semiconductor layer is sintered at 470 °C for 25 minutes, thus producing mesoporous layers with a porosity of 0.72.

### 2.5.4 Sample sensitization

$\text{TiO}_2$  or  $\text{Al}_2\text{O}_3$  films of about 1  $\text{cm}^2$  are dipped in a dye solution, typically having a concentration below  $5 \cdot 10^{-4}$  M in acetonitrile - tert-butanol 1:1 or ethanol depending on the dyes. The dying time may vary from 1 up to 12 hours (overnight) or even more, depending on the sample desired. A careful control of both the concentration of the dye solution and the dipping time has been shown to be crucial for the quality of the dyed film obtained.<sup>17</sup> Such careful dying permits homogeneous coverage of the semiconductor nanoparticles surface by a monolayer of the dye. More extreme conditions, depending on the considered experiment, will result in multilayer coverage.

During the measurements, samples are immersed into an inert ionic liquid (1-ethyl-3-methylimidazolium bis(trifluoromethanesulfonyl)imide) or 3-methoxypropionitrile (MPN) or a desired redox electrolyte.

## 2.6 References

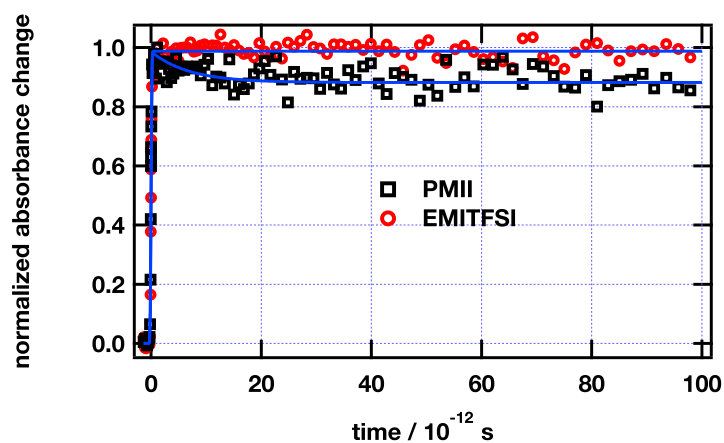
1. Pelet, S. *Femtosecond Dynamics of Electron Transfer in the Photosensitization of Wide Band Gap Semiconductors*, Thèse École Polytechnique Fédérale de Lausanne no. 2626, **2002**.
2. Wenger, B. *Effect of Electronic and Nuclear Factors on the Dynamics of Dye-to-Semiconductor Electron Transfer*, Thèse École Polytechnique Fédérale de Lausanne no. 3447, **2006**.
3. Riedle, E.; Beutter, M.; Lochbrunner, S.; Piel, J.; Schenkl, S.; Sporlein, S.; Zinth, W. *Appl. Phys. B-Lasers O.* **2000**, 71, 457–465.
4. Manzoni, C.; Polli, D.; Cerullo, G. *Rev. Sci. Instrum.* **2006**, 77, 023103.
5. Cerullo, G.; Nisoli, M.; Silvestri, S. D. *Appl. Phys. Lett.* **1997**, 71, 3616–3618.
6. Cerullo, G.; Silvestri, S. D. *Rev. Sci. Instrum.* **2003**, 74, 1–18.
7. Wiberg, J.; Marinado, T.; Hagberg, D. P.; Sun, L.; Hagfeldt, A.; Albinsson, B. *J. Phys. Chem. C* **2009**, 113, 3881–3886.
8. Kallioinen, J.; Benkö, G.; Myllyperkiö, P.; Khriachtchev, L.; Skarman, B.; Wallenberg, R.; Tuomikoski, M.; Korppi-Tommola, J. E. I.; Sundström, V.; Yartsev, A. P. *J. Phys. Chem. B* **2004**, 108, 6365–6373.
9. Kallioinen, J.; Benkö, G.; Sundström, V.; Korppi-Tommola, J. E. I.; Yartsev, A. P. *J. Phys. Chem. B* **2002**, 106, 4396–4404.
10. Skinner, D.; Whitcher, R. *J. Phys. E. Sci. Instrum.* **1972**, 5, 237–&.
11. van Stokkum, I. H. *Global and target analysis of time-resolved spectra, Lectures notes : “Troisième Cycle de la Physique en Suisse Romande”*, **2005**.
12. Ernsting, N. P. *Femtosecond Spectroscopy, Lectures notes : “CUSO Summerschool, Villars-sur-Ollon, Frontiers in Photochemistry”*, **2007**.
13. Satzger, H.; Zinth, W. *Chem. Phys.* **2003**, 295, 287–295.
14. Ford, T. A. *Long-lived excitations in conjugated polymer blend films and devices, Dissertation, Clare College, University of Cambridge*, **2005**.

15. Boschloo, G.; Hagfeldt, A. *Inorganica Chimica Acta* **2008**, *361*, 729–734.
16. Nazeeruddin, M. K.; Kay, A.; Rodicio, I.; Humphry-Baker, R.; Muller, E.; Liska, P.; Vlachopoulos, N.; Grätzel, M. *J. Am. Chem. Soc.* **1993**, *115*, 6382–6390.
17. Wenger, B.; Grätzel, M.; Moser, J. E. *J. Am. Chem. Soc.* **2005**, *127*, 12150–12151.

## Chapter 3

# Reductive quenching of ruthenium dye excited states at the surface of oxides

### Graphical abstract



Ultrafast dynamics of N719/Al<sub>2</sub>O<sub>3</sub>, observed at 630 nm

### 3.1 Introduction

In dye-sensitized solar cells (DSSCs), several electron transfer processes follow light absorption by the sensitizer. Ultrafast electron injection from the dye excited state into the conduction band of a wide bandgap semiconductor, such as nanocrystalline titanium dioxide ( $\text{TiO}_2$ ), is the key charge separation step. It has to efficiently compete with ultrafast and fast, radiative and non-radiative deactivation pathways. Moreover, the environment surrounding the dye in a solar cell contains species that might react with the dye excited state.

Sensitizer cations produced upon electron transfer to the semiconductor have to be intercepted before their potential recombination with conduction band electrons. This charge transfer between the oxidized dye and the reducing agent present in the electrolyte is crucial to ensure a large absorbed-photon-to-current conversion efficiency (APCE) of the solar cell. Simultaneously, percolation of the electrons within the semiconductor network, to reach the doped tin oxide layer on the glass electrode, has to be efficient enough to compete with electron-hole recombination within the oxide. Additionally reaction between the doped tin oxide layer and the electrolyte, especially triiodide, leads to a short-circuit within the cell.

All of these reactions are thermodynamically favorable and the reason why such high efficiencies are attained in DSSCs lies in a precise kinetic competition control of these different reactions, allowing for an optimization of the desired reaction scheme. Figure 3.1 details the different reactions taking place in a dye-sensitized semiconductor electrode.

The aim of this part of the work is a better understanding of a potential deactivation pathway, namely the reductive quenching of the excited state of a ruthenium sensitizer by iodide. This reaction has been identified to depend on the dye load, the presence of aggregates of the dye on the surface of the semiconductor being a prerequisite for observing this pathway. Iodide concentration is the second main parameter favoring this reaction pathway.<sup>1</sup>

To compete efficiently with electron injection into the semiconductor, reductive quenching has to complete within only a few picoseconds. This



time window corresponds to the slowest observed components attributed to interfacial electron transfer. The reductive quenching has been observed onto  $\text{TiO}_2$  under high concentrations of iodide. It has also been shown that it can be prevented by careful deposition of the dye onto the semiconductor, avoiding the formation of aggregates by a better control of the adsorption process.<sup>2</sup>

The reductive quenching reaction might be a cause for lower performances in DSSCs for which the concentration of redox mediator is very high. Such a situation is encountered specially when pure ionic liquids are used as electrolytes, as the iodide concentration can be as high as 6.1 M. On the other hand, monitoring the reductive quenching mechanism might be a tool for investigating the dye aggregation onto the surface of the substrate, and hence can be related with the presence of injection slow dynamics components.<sup>3</sup>

This chapter presents the continuation of work of J. Teuscher<sup>1</sup> and B. Wenger.<sup>2</sup> For a better understanding of the reaction between iodide ions and dye excited states, this study will consider measurements carried out on samples prepared onto alumina ( $\text{Al}_2\text{O}_3$ ) substrate. This semiconductor has a bandgap which is wide, positioning its conduction band potential at a level which is too low for allowing electron transfer from the excited state of the dye. Thus, the energy of the latter lies below the conduction band of the oxide. As a consequence, such samples enable to observe the dye excited state, but with adsorption conditions similar to those used with  $\text{TiO}_2$  samples. In these conditions and using photoinduced absorption spectroscopy and optical pump-probe transient absorbance, the reduced dye species has been probed.

### 3.1.1 Reaction scheme

Figure 3.1 presents in a schematic way the different photophysical processes and electron transfer steps involved in a DSSC upon light absorption. The conduction band is represented as a flat line and therefore does not account for the density of states. Vibrational states of the sensitizer are also omitted,

not being directly involved in this picture.

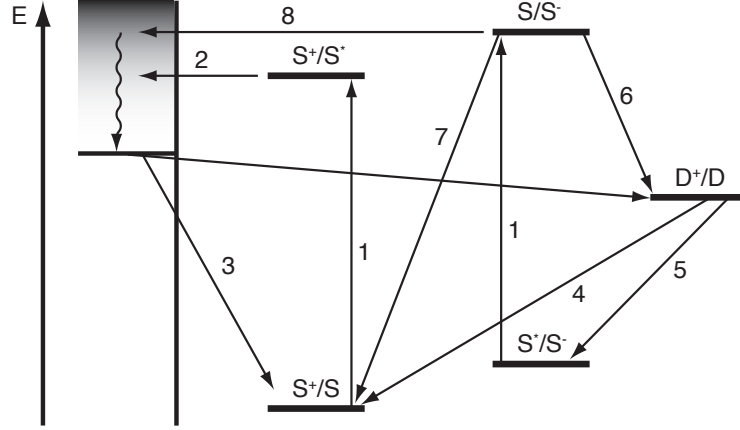


Figure 3.1: Reaction scheme of a sensitizer S at the photoanode of a DSSC in the presence of a donor D. 1. light absorption; 2. electron injection into the semiconductor; 3. recombination of the dye cation with an injected electron; 4. dye cation interception by the donor; 5. reductive quenching of the sensitizer; 6. reduced dye recombination with the oxidized donor; 7. reduced dye recombination with a nearby dye cation; 8. electron injection from the reduced dye. Numbers refer to equations of this chapter.

Upon excitation of the sensitizer (reaction 3.1), the energy of the electronically excited dye is high enough to allow for electron injection into the semiconductor (reaction 3.2). The injected electron can percolate into the semiconductor and might be collected at an indium doped tin oxide conductive glass electrode.



A reaction can occur by recombination between the injected electron and the oxidized dye anchored on the surface (reaction 3.3), leading to charge separation annihilation. This is prevented in a solar cell by efficient interception of the dye cation by a suitable redox mediator, such as iodide (reaction 3.4).



If the interception of the dye excited state by the redox mediator is fast enough and competes with electron injection, the formation of the reduced dye ( $S^-$ ) is observed (reaction 3.5). Such reaction has been reported for ruthenium complexes in solution or on the surface of sensitized oxides.<sup>4-6</sup>



Upon formation of this reduced species, three main paths are considered for dye ground state regeneration. Firstly, direct recombination of the reduced dye with the oxidized mediator is possible (reaction 3.6). Secondly, recombination with a nearby  $S^+$  (reaction 3.7) is a possible way to recover the ground state, if electron injection (reaction 3.2) occurs in parallel. Finally, electron injection from the dye reduced state is also a possible path, leading to dye ground state regeneration (reaction 3.8).



### 3.1.2 State of the art

For ruthenium dyes N719 and its heteroleptic analogue Z907 (see structures on figure 3.3), the reductive quenching reaction can be monitored by nanosecond time resolved laser flash photolysis. It is observed as a transient bleaching of the ground state absorbance recorded at 630 nm.<sup>1</sup> Upon laser light excitation and in 3-methoxypropionitrile (MPN) environment, the formation of N719 cation induces a positive absorbance change at this wavelength (figure 3.2(a), curve a). Its lifetime is limited by reaction 3.3,

hence leading to recovering of the initial species.

After addition of a reductant, the ionic liquid 1,3-propylmethyylimidazolium iodide (PMII) in the presented case, the oxidized state of N719 is intercepted by iodide and its lifetime therefore shortened, this corresponds to reaction 3.4 and is represented by the c curve of figure 3.2(a). Under higher concentrations of iodide (up to 6.1 M in pure PMII ionic liquid), the reductive quenching pathway is open (reaction 3.5) and leads to the formation of the reduced dye. The negative transient absorbance of the curve g on figure 3.2(a) exemplify this pathway.

The amplitude of the negative transient absorbance is a probe for the effective concentration of reduced dye species. At 630 nm, the dye ground state absorbs light and the observed bleaching is proportional to the concentration of the dye ground state that lacks because of the reduced dye formation. Up to 25 % of the initial dye excited state can undergo this channel. The lifetime of the dye anion is observed being at the millisecond timescale, indicating that this latter species does not inject an electron in the conduction band of the semiconductor.

Femtosecond pump-probe experiments have been performed to measure the dynamics of dye excited state quenching by iodide. The reductive quenching is reported to complete within tens of picoseconds, a timescale similar to the slower components of electron injection.<sup>2</sup> Figure 3.2(b) illustrates this behavior.

In MPN environment, the transient absorption monitored at 860 nm is dominated by the dye cation absorbance.<sup>8</sup> A first ultrafast rise of the transient absorbance signal is induced by the oxidized dye formed after ultrafast electron injection (reaction 3.2) into the semiconductor. It is followed by a subsequent slower increase of this transient absorbance, indicating a heterogeneity in electron injection dynamics. The reproducibility of the amplitude of the second dynamics component is poor. It depends on the film preparation (dye solution concentration and adsorption time).<sup>2</sup>

When the sample is prepared from a dilute solution, the slow phase

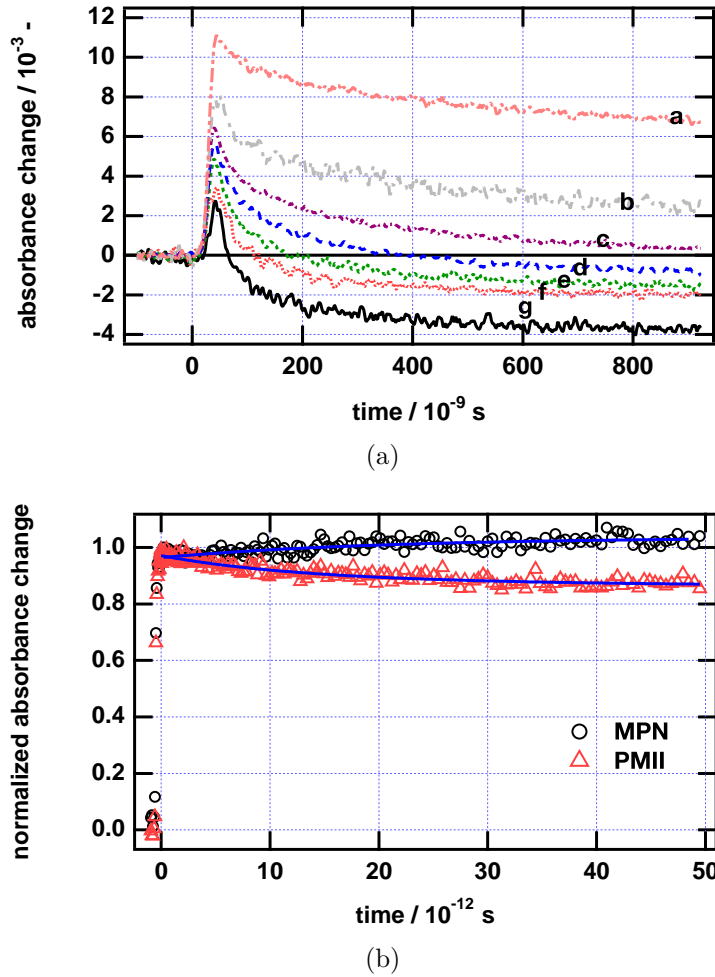


Figure 3.2: Summary of the state of the art of the reductive quenching of ruthenium dye excited states on the surface of  $\text{TiO}_2$ . (a) Nanosecond transient absorbance,  $\lambda_{\text{obs}} = 630 \text{ nm}$ ,  $\lambda_{\text{ex}} = 532 \text{ nm}$ ,  $\text{N719}/\text{TiO}_2$ , several dilutions of  $\text{PMII}$  in  $\text{MPN}$  ( $[\text{I}^-]$ : a. 0 M, b. 0.25 M (tert-propylammonium iodide (TPAI) solution), c. 0.3 M, d. 0.8 M, e. 1.5 M, f. 2.8 M, g. 6.1 M);<sup>1</sup> (b) Femtosecond transient absorbance,  $\lambda_{\text{obs}} = 860 \text{ nm}$ ,  $\lambda_{\text{ex}} = 530 \text{ nm}$ ,  $\text{N719}/\text{TiO}_2$ , in  $\text{MPN}$  ( $\circ$ ) and  $\text{PMII}$  ( $\triangle$ ), solid lines are monoexponential fits, adapted from Teuscher et al.<sup>7</sup>

disappears as the result of a monolayer adsorption of the dye and therefore homogeneous coupling to the surface. On the contrary, samples dyed with N3 dye (four protons derivative of N719 dye) concentrated solutions present a larger amplitude for the slowest dynamics.<sup>2,3</sup> This suggests the attribution of this slower component to electron injection from dye molecules loosely bound to the semiconductor. Due to the presence of dye aggregates, they are sensitizer molecules that are not in direct contact with the  $\text{TiO}_2$  surface. They have therefore a weaker coupling to the surface  $\text{Ti}^{\text{IV}+}$  ions.<sup>7,9</sup>

Upon addition of pure PMII, the same ultrafast rise is observed. But the subsequent increase is not present as the loosely bound excited molecules are intercepted by iodide prior to electron injection into the semiconductor. The reductive quenching by iodide efficiently competes with electron injection from dyes presenting slower injection dynamics.

As a consequence, the formation of the reduced dye species leads to a decrease of the transient absorbance, as fewer dye cations are formed after light absorption (reaction 3.5) and the dye anion does not absorb light at this wavelength. The dynamics of this decrease is similar to the slow increase dynamics observed in non-redox environment.

## 3.2 Experimental part

### 3.2.1 Chemicals

#### Dyes

The dye used in this study is the bis(tetrabutylammonium)[cis-di(thiocyanato)-bis(2,2'-bipyridyl-4-carboxylate-4'-carboxylic acid)-ruthenium(II)], coded as N719.<sup>10</sup> This dye is known to suffer from reductive quenching when regenerated by more than 0.8 M iodide and adsorbed in large quantities onto the semiconductor.<sup>1</sup> This has been also highlighted in the ultrafast time domain in pure iodide-based ionic liquid, i.e.  $[\text{I}^-] = 6 \text{ M}$ , observing the competition between the reductive quenching and the slowest time

components of electron injection.<sup>2</sup>

Z907 dye, cis-di(thiocyanato)-(2,2'-bipyridyl-4,4'-dicarboxylic acid)(4,4'-dinonyl-2,2'-bipyridyl)-ruthenium(II),<sup>11,12</sup> has been also used for comparison with earlier studies. Its structure differs from that of N719 by two carboxylic groups that have been replaced by nonyl chains. This hydrophobic structure allows for a better stability at higher temperatures.<sup>13</sup>

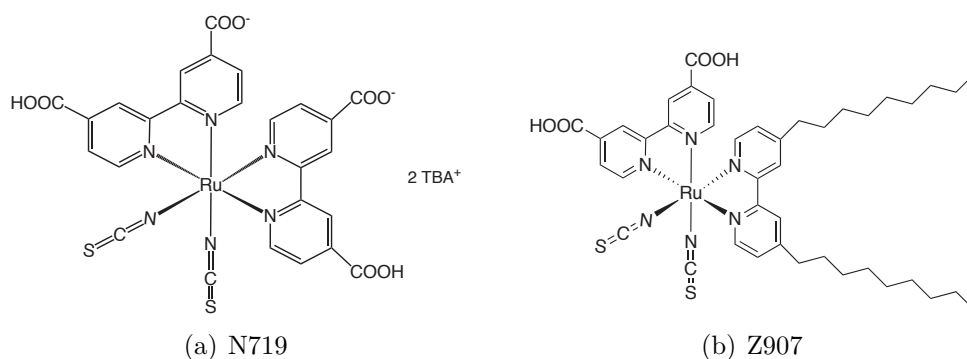


Figure 3.3: Molecular structure of ruthenium dyes. (TBA<sup>+</sup>: tetrabutylammonium).

### 1,3-propylmethylimidazolium iodide

Room-temperature ionic liquids (ILs) are of interest due to peculiar physical and chemical properties. Their thermal stability, negligible vapor pressure, non flammability, high ionic conductivity and wide electrochemical window are the key parameters of this special class of salts. They are also explored as green solvents for reaction or separation processes.<sup>14</sup>

These amazing properties made them very good candidates for DSSC applications. They can play the role of solvent only, having inert counteranions or be involved in the electrochemical processes with anions such as iodide. Mixing redox-inactive and redox-active ILs allows for adjusting the desired iodide concentration, i.e. maintaining a high donor concentration.<sup>15</sup> In addition, this mixture allows for lowering the viscosity of the solution, which is high for pure 1,3-propylmethylimidazolium iodide (PMII).

The reductive quenching pathway has been only observed under high iodide concentration. When a dissolved iodide salt, as lithium iodide (LiI) or tetrapropylammonium iodide (TPAI) allows for preparing solutions up to about 0.3 M, the use of ILs renders possible the reaching of iodide concentrations far beyond 1 M.

PMII (figure 3.4 a) is a IL which is promising for uses in electrolytes due to its relatively low viscosity of 1084 cP and its redox-active iodide counteranion.<sup>16</sup> In DSSC electrolytes, it is commonly used at a concentration of less than 1 M, diluted in a less viscous, redox-inactive IL such as 1-ethyl-3-methylimidazolium tetracyanoborate (EMITCB). In this fundamental study, PMII is used pure having 6.1 M iodide ( $\rho(\text{PMII}) = 1.54 \text{ g} \cdot \text{cm}^{-3}$ ,  $\text{MW}(\text{PMII}) = 252.1 \text{ g} \cdot \text{mol}^{-1}$ )<sup>i</sup>. This strategy enables to enhance the reductive quenching. In these conditions, up to 25% of the excited dye undergoes this pathway.<sup>1,17</sup> Measurements in redox-inactive environments are carried out in 1-ethyl-3-methylimidazolium bis(trifluoromethanesulfonyl)imide<sup>ii</sup> (EMITFSI).

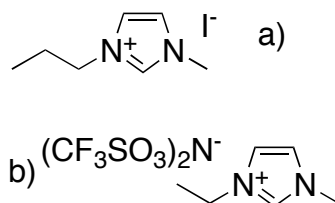


Figure 3.4: a) Molecular structure of 1,3-propylmethylimidazolium iodide (PMII) ionic liquid; b) Molecular structure of 1-ethyl-3-methylimidazolium bis(trifluoromethanesulfonyl)imide (EMITFSI) ionic liquid.

## Alumina

To simplify the system studied, we use alumina (Al<sub>2</sub>O<sub>3</sub>) films, removing the dye cation from the reaction scheme. As presented in section 3.1, the position

<sup>i</sup>Merck datasheet

<sup>ii</sup>IUPAC name: 1,1,1-trifluoro-N-(trifluoromethylsulfonyl)methanesulfonamide



of its conduction band edge does not allow for electron injection from the dye.

$\text{Al}_2\text{O}_3$  has a band gap of 8.45-9.9 eV, which renders its conduction band high in energy at a potential of -4.45 V vs. SCE.<sup>18</sup> This does not allow for electron injection from excited N719, which excited-state oxidation potential is -1.1 V vs. SCE.<sup>19</sup> This electronic property easily suppresses the presence of the oxidized dye in the system, facilitating the identification of other phenomena than electron injection upon absorption of light.

On titania, if the reduced dye is formed by quenching of the dye excited state, this branch of the reaction scheme has to efficiently compete with the electron injection process (the system undergoes reaction 3.5 instead of reaction 3.2). The electron injection has been shown to present yields close to unity at 530 nm excitation in an electrochemically inert environment with heterogeneous dynamics ranging from  $< 100$  fs up to several hundreds of picoseconds. The slowest available timescale for the reductive quenching to occur is then in the hundreds of picoseconds time domain, corresponding to the slowest reported components of the electron transfer to the semiconductor.<sup>20</sup> Onto  $\text{Al}_2\text{O}_3$ , although electron injection does not occur, the reductive quenching of the dye is expected to happen within the same timescale.

$\text{Al}_2\text{O}_3$  layers of 4 to 8  $\mu\text{m}$  are deposited on a glass substrate by the doctor blade technique, which consists in translating a roller over the sample to spread the paste.<sup>21</sup> The paste used is composed of  $\text{Al}_2\text{O}_3$  6.4 nm diameter nanoparticles (18 wt%), a polymer (hydroxypropyl cellulose 100'000, 3.6 wt%) in 2-butoxyethanol (78.4 wt%). After evaporation of the solvent on a hotplate set at 80 °C, the sample is calcinated at 470 °C for 25 minutes for removing the polymer and therefore opening the mesoporous network. The resulting porosity is of 0.72. This latter step also allows for sintering of the sample, preparing an interconnected network of the nanoparticles.

## Titanium dioxide

Anatase titanium dioxide ( $\text{TiO}_2$ ) layers of controlled thickness of 2.5 to 10  $\mu\text{m}$  are also prepared by the doctor blade technique. The thickness is controlled by the depth of the well used for the doctor blade, which is controlled by successive layers of Scotch tape (3M, Magic tape).

The paste used consists of  $\text{TiO}_2$  16 nm diameter particles (14 wt%) and a polymer (ethyl cellulose, 40 wt% (in respect to  $\text{TiO}_2$ ) in anhydrous terpeneol. Upon calcination at 470 °C for 25 minutes, the resulting layer has a porosity of 0.625. This corresponds to a rugosity factor of 141  $\mu\text{m}^{-1}$  and a pore mean diameter of 20 nm.

### 3.2.2 Samples

Semiconductor substrate (titania or alumina) is dipped into a dye solution (N719 or Z907) of concentration  $5 \cdot 10^{-5}$  M in a 1:1 (v:v) acetonitrile - tert-butanol mixture overnight (12 - 15 hours). Prior to the dipping, the samples are briefly warmed up to 200 °C to avoid the presence of water in the pores, and thus favoring adsorption.

After dyeing, samples are carefully rinsed with ethanol. A drop of the desired environment, either redox-active (PMII) or inert (MPN or EMITFSI), is deposited onto the film, which is then covered with a thin glass plate.

## 3.3 Results and discussion

### 3.3.1 PIA spectroscopy

#### Methodology

PIA spectroscopy is carried out onto alumina and titania samples. This technique is used to map the spectral signature of the long lived dye anion. Excitation is applied either at 568 or 470 nm.

### N719 excited state

Measurement on  $\text{Al}_2\text{O}_3$  films are performed to observe the UV-Vis-NIR spectrum of the excited dye species,  $S^*$ . As stated before,  $S^*$  cannot inject an electron in the  $\text{Al}_2\text{O}_3$  film because of location of the conduction band edge of this oxide. Hence  $S^*$  should not be quenched by the substrate and the species should be observable, as well as the emission of the dye.

The use of this technique has the advantage of a phase sensitive detection scheme, thus it allows for the measurement of weak transient absorbance. In addition, the spectral range of the PIA setup extends to 1600 nm in the NIR, which is wider than commercial luminescence systems that might have been used for monitoring the emission of the dye.

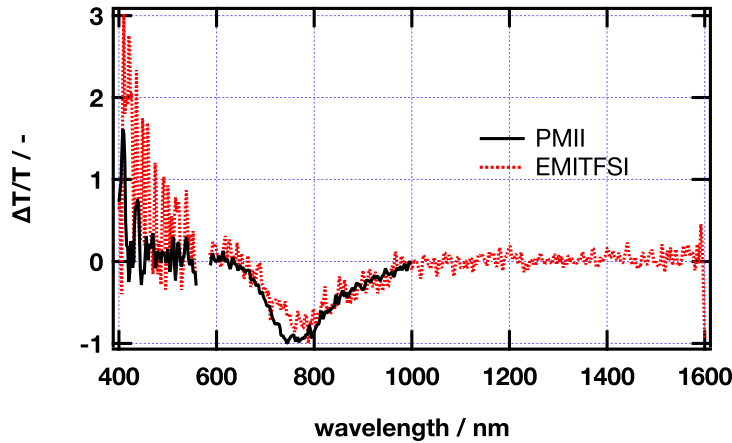


Figure 3.5: PIA spectra of N719/ $\text{Al}_2\text{O}_3$ ,  $4\ \mu\text{m}$ ,  $\lambda_{\text{ex}} = 568\ \text{nm}$  at 10 Hz, in EMITFSI (—) and PMII (---).

A first measurement is realized in a redox-inactive environment, i.e. the ionic liquid EMITFSI. Unfortunately, emission of the sample for N719 dye presents a strong signal that masks all possible small component arising from a transient species (see figure 3.5). This emission is centered at 770 nm, 60 nm lower than that reported for N719 in ethanolic solution (830 nm).<sup>10</sup> In PIA spectroscopy of such samples, one expects a transient signal amplitude in the range of the  $m\Delta T/T$  for a transient dye species. Emission signals, with a 1000

times stronger amplitude therefore hide every potential transient absorbance signal. As a consequence, the response only shows the emission of N719 dye adsorbed onto  $\text{Al}_2\text{O}_3$ .

Replacing EMITFSI by pure PMII, the emission amplitude is not quenched by iodide. In terms of spectral shape, no change is noticed. In the near-infrared (NIR) no new transient species is revealed up to 1600 nm.

These measurements do not allow for characterizing the dye reduced state. If it is formed after light absorption, it is generated in a too small quantity to affect the emission and is therefore not observable.

### N719 oxidized state

Upon adsorption onto  $\text{TiO}_2$ , one expects to see the spectral signature of the dye cation when the transient is measured in the redox-inactive environment (EMITFSI). The lifetime of the oxidized dye is reported occurring on the microsecond-millisecond time scales by Tachibana *et al.*<sup>22</sup> This time window is easily observable by PIA spectroscopy.<sup>23</sup> The dashed curve on figure 3.6 shows this transient spectrum, assigned to the dye cation. A band is revealed having its maximum at 770 nm and a shoulder at 620 nm. This corresponds to the reported oxidized N719 spectrum.<sup>24</sup> In the NIR, a featureless weak positive transient absorbance is measured. Its origin is ascribed to absorption by trapped electrons or polaron states at the conduction band edge of the  $\text{TiO}_2$ .<sup>25,26</sup>

After addition of PMII, the NIR side of the spectrum presents drastic changes. A broad and intense positive absorbance covers all wavelength between 800 and 1600 nm. Besides this NIR change, the isosbestic point is shifted to the lowest energies direction, up to 590 nm. This result is consistent with previous nanosecond flash-photolysis experiments under the same conditions that revealed a negative signal from 600 nm to 660 nm when the reduced species is present.<sup>1</sup> PMII PIA spectroscopy spectrum on a bare  $\text{TiO}_2$  sample (i.e. without dye) has also been measured, allowing the rejection of any artifact due to PMII light absorption. Therefore, these changes in the

transient spectra are attributed to the reduced dye present after reductive quenching of excited N719.

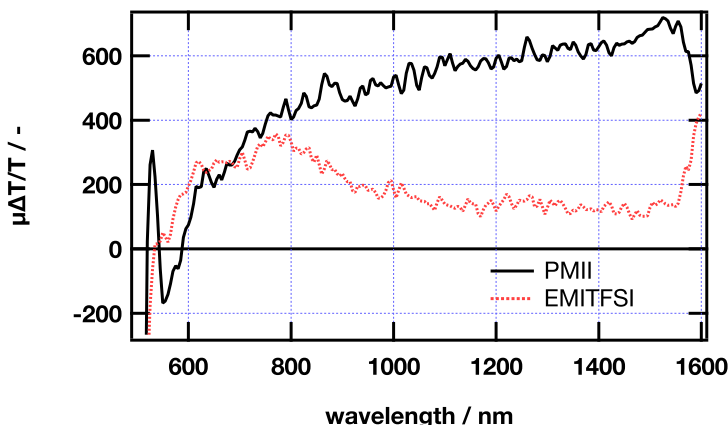
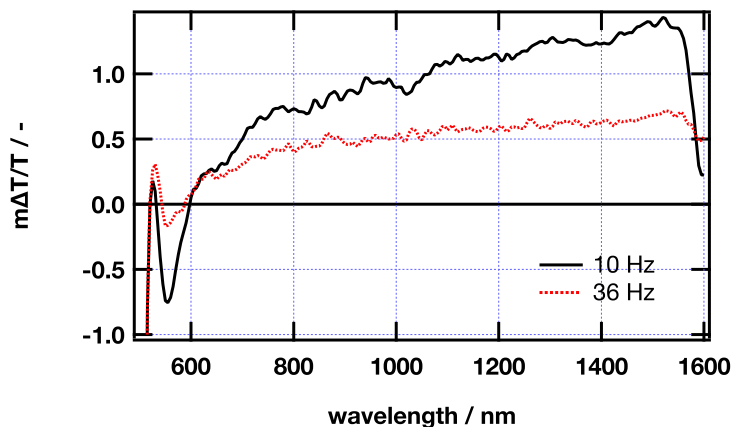


Figure 3.6: PIA spectra of N719/TiO<sub>2</sub>, 2.8  $\mu\text{m}$ ,  $\lambda_{\text{ex}} = 470$  nm at 10 Hz, in EMITFSI (--) and PMII (-).

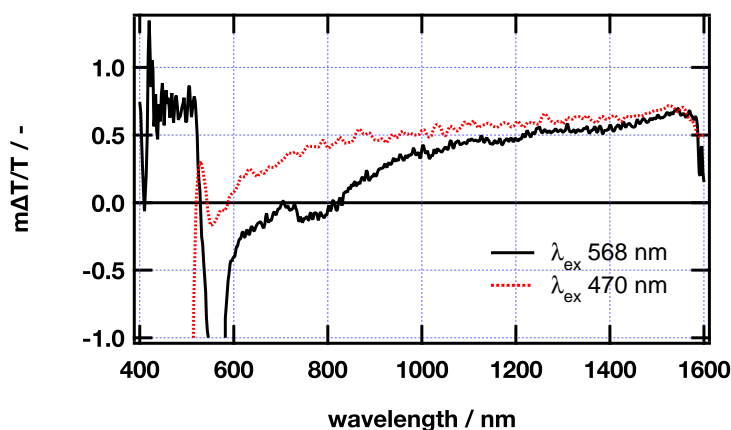
As the lifetime of the reduced dye is expected to be long, i.e. milliseconds, the frequency of PIA acquisition has been changed. In PIA spectroscopy, the intensity of the recorded signal is related to the lifetime of the observed species. Therefore the comparison of two transient spectra recorded at different excitation modulation allows for learning on the timescale of the observed transient species. A first acquisition at 10 Hz, and another at 36 Hz are compared in our case. Figure 3.7(a) reflects this difference, enhancing the NIR components at a slower modulation frequency. Hence it grants the confirmation of the assignment of the NIR broad and intense positive transient absorbance to the dye anion.

Moreover, the dye anion is suspected to have a positive transient absorbance below 550 nm.<sup>5</sup> Unfortunately, the excitation light source is a diode centered at 470 nm and therefore masks this region of the spectrum with a very intense and large in spectrum negative signal. Using a yellow light source, a diode centered at 568 nm, allows for cleaning this region of the spectrum, shifting the negative signal induced by the excitation light to the red. In this scheme, it is now possible to reveal transient species presenting

transient absorbance below 500 nm.



(a)



(b)

Figure 3.7: PIA spectra of N719/TiO<sub>2</sub>, 2.8 μm, PMII. (a) Modulation frequency change, 10 Hz (—) and 36 Hz (---),  $\lambda_{\text{ex}} = 470$  nm; (b) Excitation wavelength change,  $\lambda_{\text{ex}} = 568$  nm (—) and  $\lambda_{\text{ex}} = 470$  nm (---) at 10 Hz.

Figure 3.7(b) reveals a positive transient absorbance, which appears being noisy but intense. The dye anion therefore absorbs light from 420 to 520 nm. In addition, this measurement presents a red shift of the isosbestic point. This is probably due to an artifact, arising from the negative signal induced around the light source wavelength.

Thanks to these measurements, the dye anion has been observed. It

absorbs light from 420 to 520 nm as well as in the NIR. This is an evidence for its formation.

### Z907 comparison

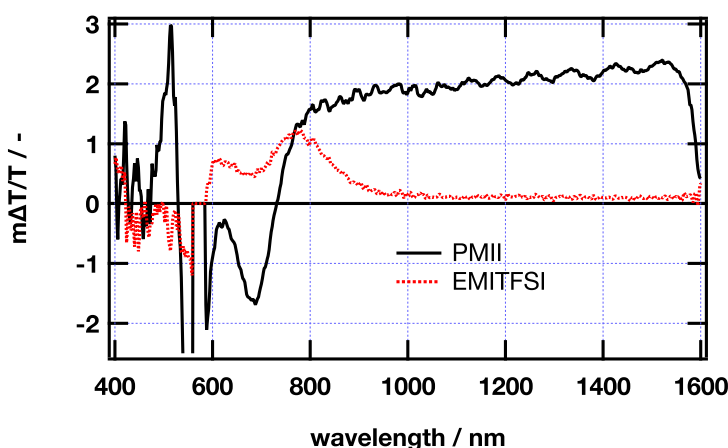


Figure 3.8: PIA spectra of Z907/TiO<sub>2</sub>, 2.8  $\mu$ m,  $\lambda_{\text{ex}} = 568$  nm at 10 Hz, in EMITFSI (--) and PMII (—).

Previous nanosecond experiments have been also reported for Z907 parent dye.<sup>1,2</sup> Figure 3.8 is obtained after 568 nm excitation of Z907/TiO<sub>2</sub> and maps the transient spectrum of the dye cation. When compared to figure 3.6, it reveals a similar behavior than N719. In the redox-inactive environment, EMITFSI, one can clearly observe a peak centered at 770 nm and a shoulder at 610 nm. This corresponds to the expected spectra for Z907 oxidized species according to measurements performed with nanosecond flash photolysis. In the NIR, the positive transient due to the injected electrons is not clearly observable.

After PMII addition onto the sample, a similar behavior than the N719 case is observed. The isosbestic point is red-shifted, with this molecule up to 730 nm. A broad and intense featureless absorbance is present in the NIR from 800 to 1600 nm. Below the excitation wavelength, a strong and sharp peak is centered at 515 nm. These two observations are similar to what is

observed with N719 dye and therefore mean that the reduced species of Z907 is observed. It has an absorption band centered at 515 nm in the visible and also a broad NIR absorption.

### PIA conclusions

Measurements achieved with N719 adsorbed onto  $\text{Al}_2\text{O}_3$  do not make possible to see any positive transient resulting from the dye anion transient absorbance. This is due to the dye emission which hides any positive signal because of its high amplitude.

Upon adsorption of the dye onto  $\text{TiO}_2$ , the emission is quantitatively quenched and thus the transient species might be observed. The dye cation is easily observed in redox-inactive environment (EMITFSI) and drastic changes are observed upon addition of pure PMII onto the sample. Reduced N719 appears having positive transient absorbance from 420 to 520 nm as well as in the NIR. These results are comparable to what has been measured with nanosecond transient absorbance.<sup>1</sup> The same red shift of the isosbestic point is observed.

A comparison of figure 3.8 with figure 3.9 for the Z907 case illustrates the consistency of the results obtained by two different methods, PIA and nanosecond flash photolysis, respectively. The bleaching at longer times covers the 600-750 nm region. This is the signature for a lack of dye ground state after iodide regeneration, and therefore for the presence of reduced dye in the reaction scheme. A characteristic positive transient absorbance is also observed in both cases, centered at 515 nm. In addition, the NIR side is explored with the PIA method and reveals a strong positive absorbance, as for N719.



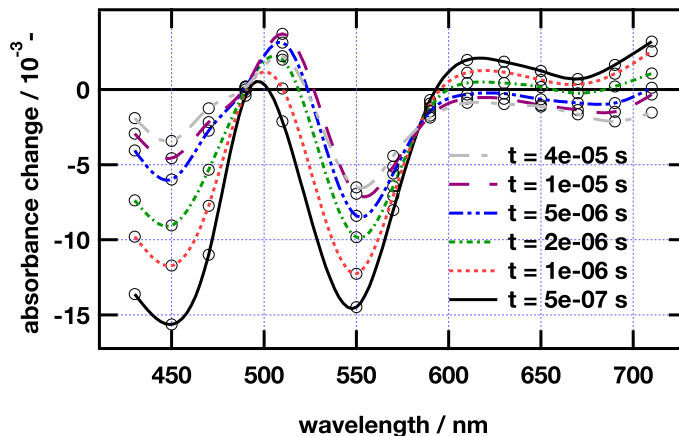


Figure 3.9: Nanosecond time resolved transient spectrum of Z907/TiO<sub>2</sub> in pure PMII,  $\lambda_{\text{ex}} = 532$  nm, adapted from.<sup>1</sup>

### 3.3.2 Femtosecond transient absorbance

#### Methodology

Two colors and white-light-continuum setups are used. These measurement are carried out on Al<sub>2</sub>O<sub>3</sub>.

#### Two colors pump-probe spectroscopy, $\lambda_{\text{obs}} = 860$ nm

The formation of the dye excited state species following ultrashort laser excitation is measured. The probe wavelength is set at 860 nm as it is the most documented wavelength in the literature for observing N719 and derivatives dyes cations.<sup>20,27</sup> This is because it has been established by different groups that the dye oxidized state has a much higher molar extinction coefficient than the excited state at this wavelength, but transient absorbance by the latter is not negligible. On Al<sub>2</sub>O<sub>3</sub>, the monitoring of the dye excited state is expected as electron injection to the semiconductor is not possible. The pump is tuned at  $\lambda_{\text{ex}} = 530$  nm, close to the maximum of the UV-Vis absorption spectrum.

The transient of N719/Al<sub>2</sub>O<sub>3</sub> is measured in an inert environment (EMITFSI) and in a high iodide concentration medium (PMII) for compar-

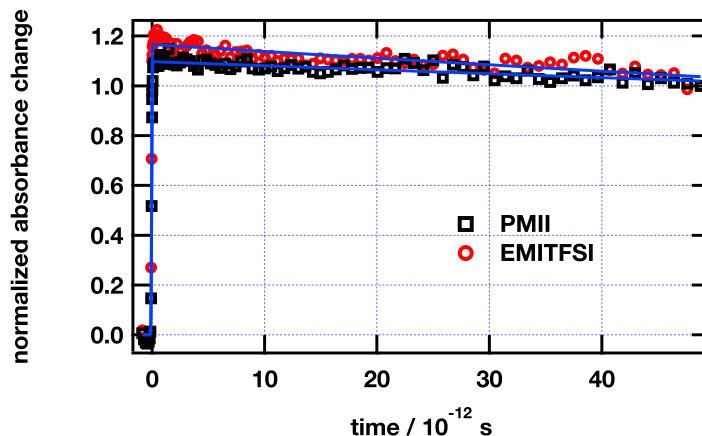


Figure 3.10: Femtosecond transient absorbance,  $\lambda_{obs} = 860$  nm,  $\lambda_{ex} = 530$  nm, N719/ $\text{Al}_2\text{O}_3$ , in EMITFSI (○) and PMII (◻); solid lines are fits results for a convolution of a gaussian and one exponential. EMITFSI:  $\sigma = 40$  fs,  $\tau_1 = 415$  ps; PMII:  $\sigma = 38$  fs,  $\tau_1 = 664$  ps.  $\sigma$  and  $\tau_1$  are the parameters of equation 2.10.

ison. The result is reported on figure 3.10. A fit analysis reveals that both curves of this figure do not need any component to be deconvoluted with the ultrafast rise. This is in accordance with the observation of an excited state. Therefore, a single value of about 40 fs is reported for the rise time constant, being faster than the resolution of the setup. This corresponds to the light absorption step.

The transient recorded does not allow for the observation of any change in absorbance of the sample induced by intersystem crossing. Nevertheless, the latter is known to occur for bipyridyl ruthenium complexes within hundred femtoseconds<sup>28,29</sup> and nothing, excepted the ultrafast rise is observed at this timescale. For the ruthenium(II) trisbipyridyl dye, the intersystem crossing completes on even a faster timescale, within 15-40 fs.<sup>30,31</sup>

The following process observed is the deactivation of the excited state, leading to a decrease of the positive transient signal. The luminescence lifetime of N3 parent dye has been reported being 50 ns in ethanol and at room temperature.<sup>21</sup>

Here the apparent lifetime of the dye excited state appears shorter.

In EMITFSI and adsorbed onto  $\text{Al}_2\text{O}_3$ , the transient shows a small decay over 50 ps. Upon iodide addition (pure PMII) a slight change is observed, revealing a slower decay than in redox inactive medium. This is therefore not fully explained because it is not likely to represent the lifetime of the dye excited state.

This difference expected for the two distinct environments, namely quenching of the dye excited state by iodide, is not observed at this wavelength. The weak absorbance of the excited state of the dye might be the cause of the failure of observing the quenching as the latter is probably not affecting all the population of the dye. For that reason, the investigation continues at a probe wavelength of 630 nm for the observation of quenching evidence. At this latter wavelength, the dye excited state is expected to have a higher molar extinction coefficient.<sup>22,32</sup> Hence the measurement will be more accurate.

### Two colors pump-probe spectroscopy, $\lambda_{obs} = 630$ nm

Figure 3.11 presents the dye MLCT state of N719 adsorbed onto  $\text{Al}_2\text{O}_3$  transient absorbance, recorded at 630 nm under 530 nm excitation.

The transient in EMITFSI therefore presents the absorbance change induced by the appearance of the excited dye. On the timescale presented (from 0 to 100 ps) and after the ultrafast rise, no noticeable change of the absorbance is recorded after the laser pulse. This is in agreement with the lifetime of the MLCT state of this dye in solution, which is 50 ns.<sup>21</sup> This transient is well fitted by the convolution of the instrument response (100 fs) and a single exponential with  $\tau = 10 \mu\text{s}$ . This large value stands for infinity, compared to the timescale of the measurement.

Upon addition of PMII, a clear decrease of the initial absorbance change is noticed. It accounts for about 10 to 15% of the initial amplitude and is associated with a 6.9 ps time constant. A second time component is necessary for fitting these data, with a large time constant,  $\tau = 10 \mu\text{s}$ . This latter time constant is kept at this “infinity” value, matching the observation raised in

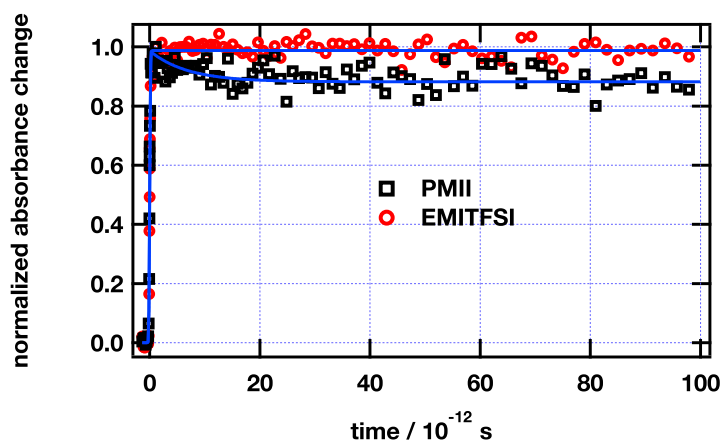


Figure 3.11: Femtosecond transient absorbance,  $\lambda_{obs} = 630$  nm,  $\lambda_{ex} = 530$  nm, N719/ $\text{Al}_2\text{O}_3$ , in EMITFSI ( $\circ$ ) and PMII ( $\square$ ); solid lines are fits results. The convolution of a gaussian and one exponential for EMITFSI:  $\sigma = 100$  fs,  $\tau_1 = 10$   $\mu\text{s}$ ; the convolution of a gaussian and two exponentials for PMII:  $\sigma = 100$  fs,  $\tau_1 = 6.9$  ps,  $\tau_2 = 10$   $\mu\text{s}$ .  $\sigma$  and  $\tau_i$  are the parameters of equation 2.10.

### EMITFSI.

This observation clearly confirms the reaction between the dye excited state and iodide reductant species. A decrease of transient absorbance is consistent with the production of reduced dye through reductive quenching by iodide. The time constant associated to the quenching is 6.9 ps. It is for that reason compatible with a direct competition with the slow components reported for electron injection, i.e. ten to several hundreds picoseconds.<sup>20,29,33–38</sup> As a consequence, in the case of N719-sensitized  $\text{TiO}_2$ , the reductive quenching will compete with the slowest part of the electron injection. But the small difference in timescale between these two reactions means that the reductive quenching will not be an efficient pathway. Only part of the dye molecules that undergo slow injection will be quenched by iodide.

Finally it seems that, even on  $\text{Al}_2\text{O}_3$ , not all the dye can be intercepted by this reaction, otherwise we would have seen a 100 % efficient process, which is not the case.

### Pump-white-light-supercontinuum-probe spectroscopy

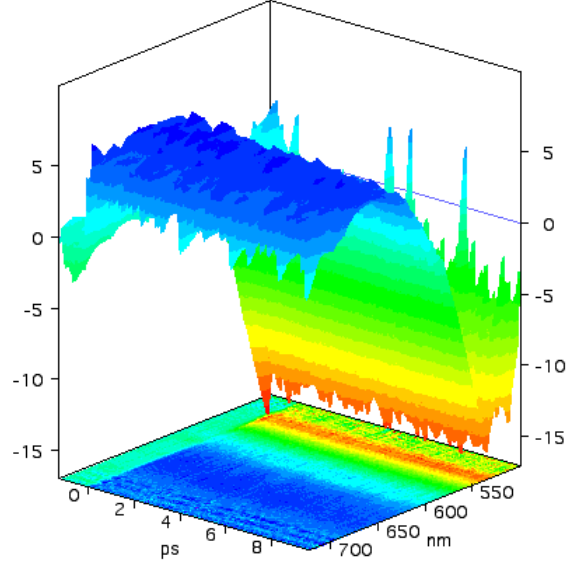
Following these latter results, one may want to better understand the reaction scheme involved for reductive quenching. As the reduced dye species, although undoubtedly revealed, is still not known by its spectra, only indirect measurements of its presence have been done. Recording a transient spectrum over the visible domain instead of a single wavelength is one of the tools of choice for this purpose. This measurement is similar to the measurement taken at  $\lambda_{obs} = 630$  nm. It will allow for direct comparison of the early dynamics of N719 adsorbed onto  $\text{Al}_2\text{O}_3$  in EMITFSI, redox inactive, versus PMII, redox active.

As described in section 2.1.7, the data treatment applied to white-light results involves at first a time correction that accounts for the chirp of the probe pulse and a smoothing over the wavelength axis (figure 3.12). Then singular value decomposition (SVD) is the second step applied to the data matrices following the procedure described in section 2.1.7. This mathematical data reduction method provide the means to get rid of most of the noise.

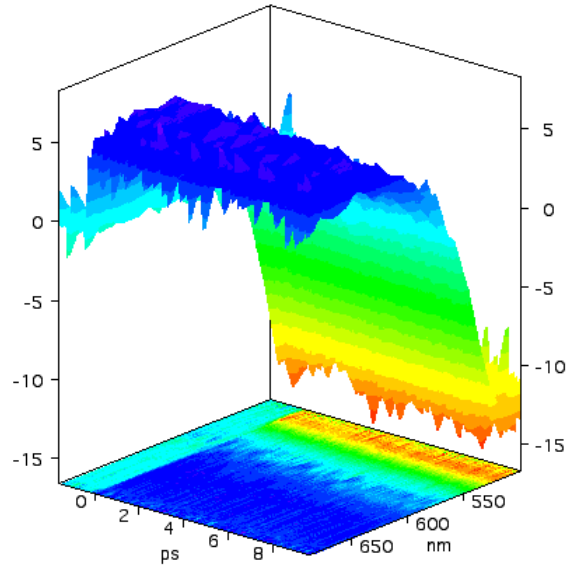
From the SVD results over the EMITFSI samples, several observations are made. The first singular value is very intense compared to the others (see figure 3.13(a)) and thus accounts for 55 % of the total amplitude (over 100 components). This domination suggests us that there is only one chemical species involved.<sup>39</sup> This is what we expect observing N719 onto  $\text{Al}_2\text{O}_3$  and we therefore deduce that the observed transient is the spectrum of the excited dye. It is composed of a bleaching centered at 540 nm, a maximum absorbance change at 650 nm and an isosbestic point at 585 nm, in agreement with the spectrum of the excited N719 reported in the literature.<sup>22,32</sup>

Although the second and third components, both of time and wavelength, do not seem to present any other reliable behavior, they will be added in the reconstructed matrix. This is done not to loose any hidden spectral behavior of the recorded transient.

The reconstructed matrix after SVD data reduction is then used for the

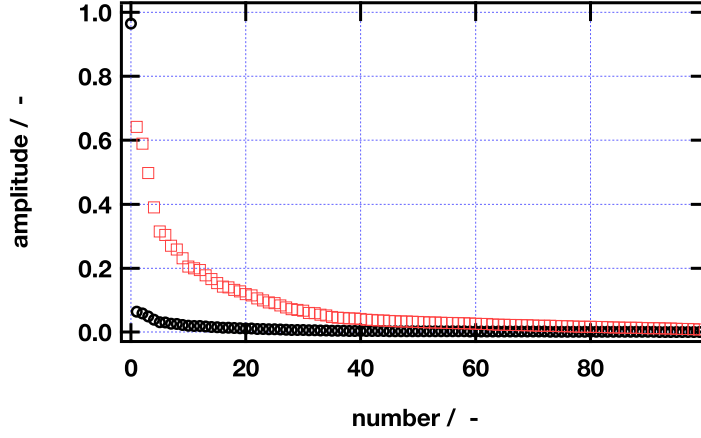


(a) EMITFSI

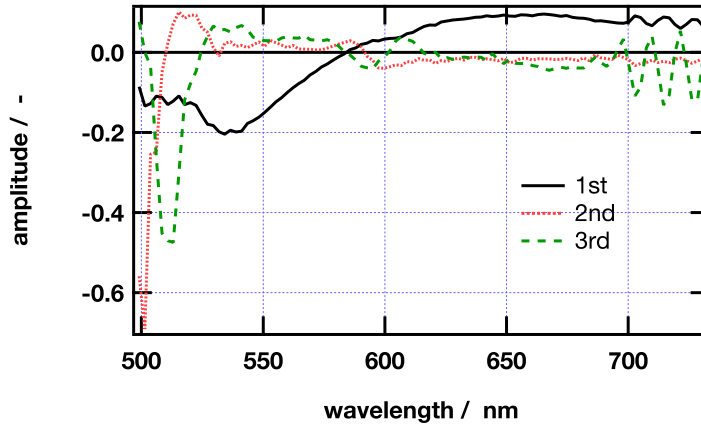


(b) PMII

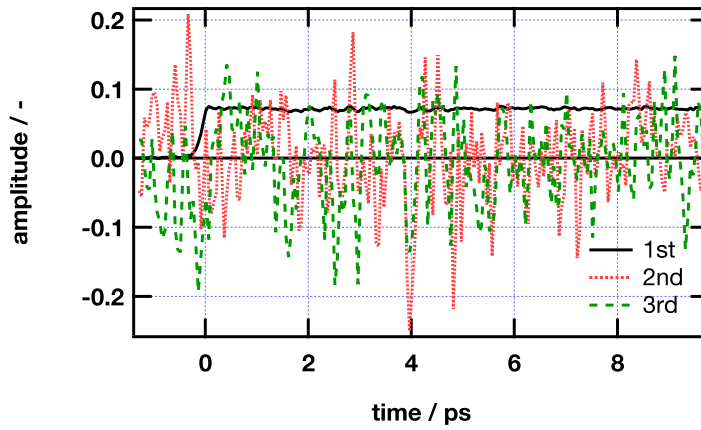
Figure 3.12: (a) Femtosecond transient spectra of N719/ $\text{Al}_2\text{O}_3$  in EMITFSI over 10 ps, white-light-continuum probe,  $\lambda_{\text{ex}} = 530$  nm, the vertical axis is the mOD value. (b) Femtosecond transient spectra of N719/ $\text{Al}_2\text{O}_3$  in PMII over 10 ps, white-light-continuum probe,  $\lambda_{\text{ex}} = 530$  nm, the vertical axis is the mOD value. Data matrix shown are smoothed and reduced to 100 wavelengths.



(a) Singular values (○), expanded 10 times (□)



(b) Wavelength vectors



(c) Time vectors

Figure 3.13: Singular value decomposition of the femtosecond transient spectrum of N719/ $\text{Al}_2\text{O}_3$  in EMITFSI.

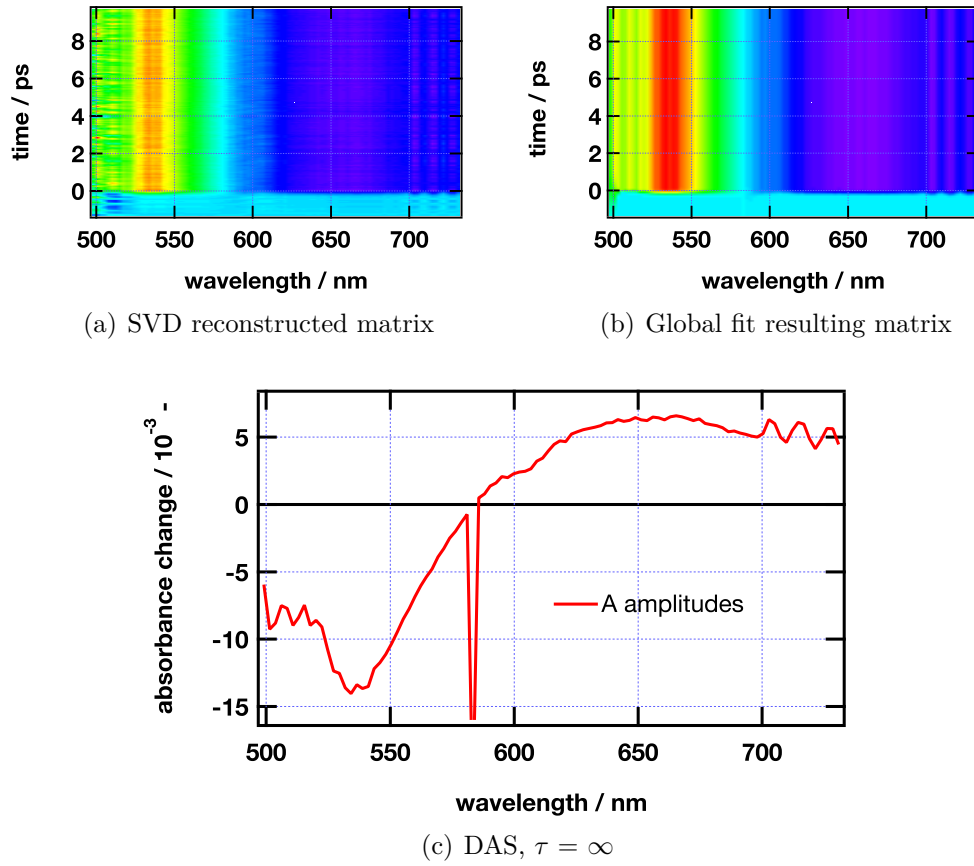


Figure 3.14: Data treatment results. (a) SVD reconstructed matrix with three wavelength and time components. (b) Global fit resulting matrix, convolution of a gaussian ( $\sigma = 88$  fs) and one exponential ( $\tau = 9.7 \mu\text{s}$ ).  $\sigma$  and  $\tau_i$  are the parameters of equation 2.10. (c) Decay associated spectrum of the first time component.



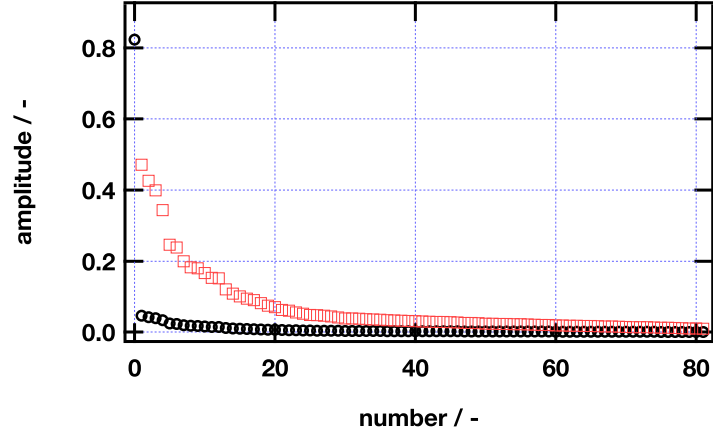
global fitting procedure. The latter is applied as described in section 2.1.7. Enabling to fit hundred wavelengths at the same time, it produces a “decay associated spectrum” (DAS) associated with each time component.

In the case of N719/ $\text{Al}_2\text{O}_3$  in EMITFSI, a single time constant is sufficient to fit the data at the observed time scale. This time constant is found being  $\tau = 9.7 \mu\text{s}$ , thus at infinity on our timescale. This is again in accordance with the lifetime of the excited state of N719.

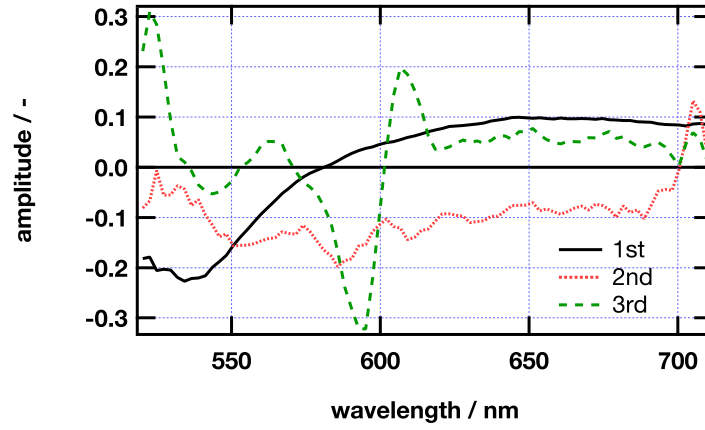
The same data processing is applied on samples upon addition of PMII iodide source.

Again, the first singular value accounts for 60 % of the total amplitude (over 100 singular values) (see figure 3.15(a)). The first wavelength component seems to stand for the dye excited state, with a bleaching centered at 540 nm, a transient maximum at 650 nm and the isosbestic point at 585 nm as reported for the measurement in EMITFSI. But, contrary to the latter case, the second time component presents a clear time-dependant behavior (figure 3.15(b)), well fitted with a 5 ps exponential time constant. Its associated spectral component appears to be smoothly negative over the reported spectrum. The third wavelength base vector seems to contain information located around the isosbestic point. At the wavelength of the isosbestic point, the quality of the data tends to be poor. This is due to the null change in absorbance, which is drastically affected by any small perturbation. This will have consequences in the global fit analysis, which will be poor around the isosbestic point on a systematic manner.

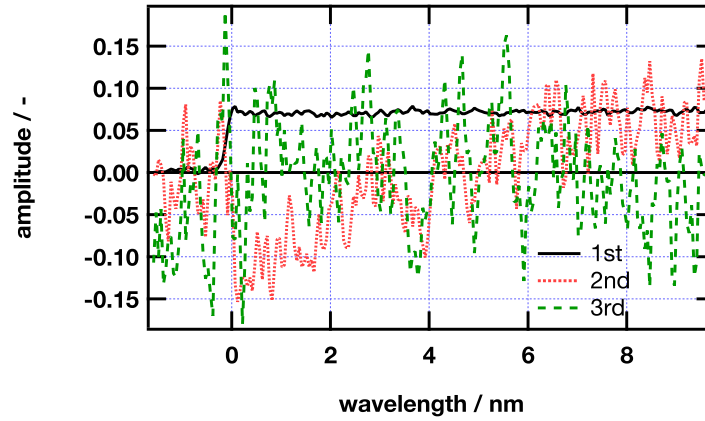
After data reduction, the matrix is reconstructed and used for the global fitting procedure. The DAS at large times, i.e. at infinity, presents the spectrum of the excited dye species. The bad resolution around the isosbestic point adds very high noise to the spectrum. This spectrum is therefore consistent with the only DAS reported for the EMITFSI case. It might be noted that this time is drastically smaller than the one reported for the EMITFSI case, indicating a shorter lifetime for the excited species under these conditions. In addition, for the PMII case, a second exponential



(a) Singular values (O), expanded 10 times (□)



(b) Wavelength vectors



(c) Time vectors

Figure 3.15: Singular value decomposition of the femtosecond transient spectrum of N719/ $\text{Al}_2\text{O}_3$  in PMII.

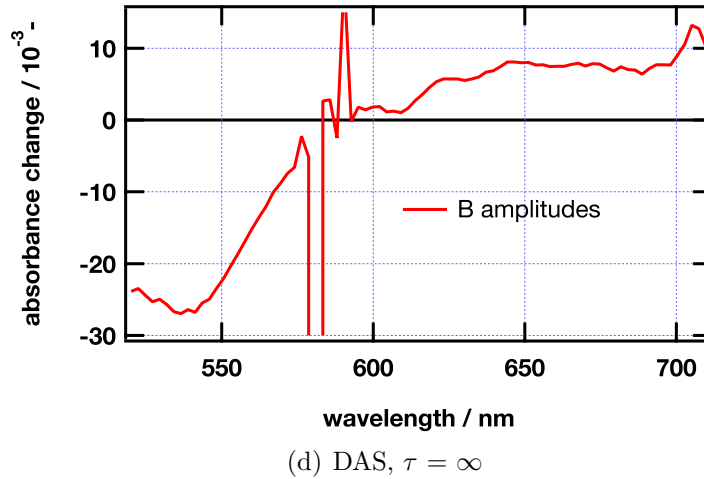
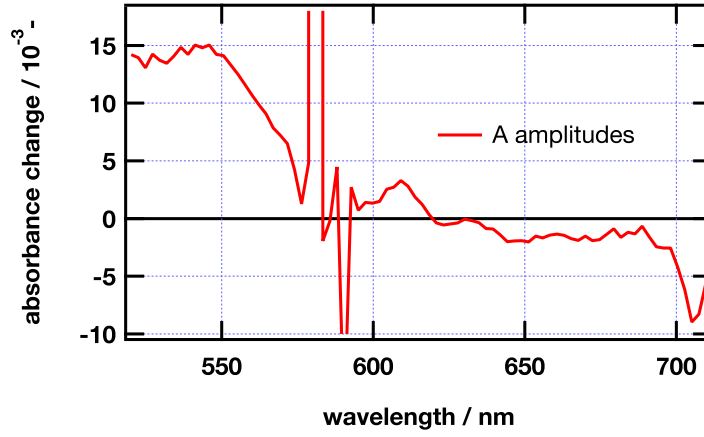
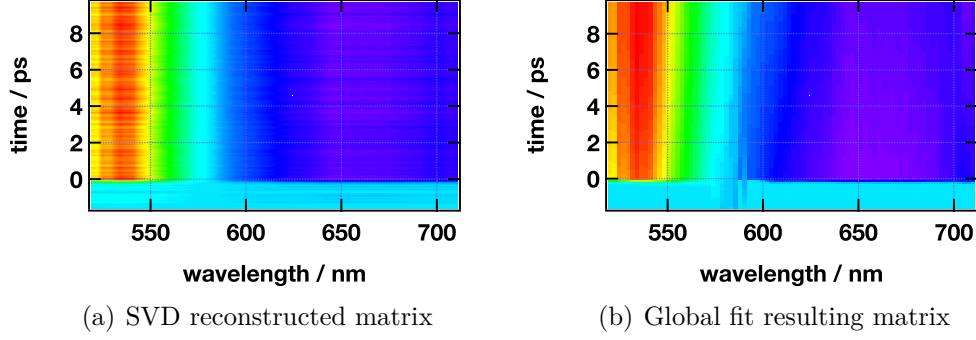


Figure 3.16: Data treatment results. (a) SVD reconstructed matrix with three wavelength and time components. (b) Global fit resulting matrix, convolution of a gaussian ( $\sigma = 75$  fs) and two exponentials ( $\tau_1 = 19.2$  ps,  $\tau_2 = 53.1$  ps).  $\sigma$  and  $\tau_i$  are the parameters of equation 2.10. (c) Decay associated spectrum of the first time component. (d) Decay associated spectrum of the second time component.

is needed for fitting the matrix. It is characterized by a time constant,  $\tau = 19.2$  ps, and a DAS that influences mainly the blue side of the spectrum, inducing a subsequent decrease of the bleaching signal. This second time component can then be understood as a result of reductive quenching.

In the two colors experiment, the timescale of the reductive quenching has been defined at 6.9 ps and the reported difference for the white-light measurement (treble duration) needs to be explained. Previous literature reports of reductive quenching in similar systems attribute its origin on inhomogeneous adsorption of the dye onto the substrate.<sup>1-3</sup> This leads to slower electron injection, letting time for interception of the excited state by iodide. In the case of this experiment, working on  $\text{Al}_2\text{O}_3$  substrate, i.e. without electron transfer, this should not be an issue. Because the dye cannot inject any electron, its excited state lives long enough for making possible efficient iodide interception. The surface shape might also have an influence on the way iodide may approach the dye molecules. It is therefore possible to justify this difference in time constant by different samples, presenting a distinct aggregation level. Inhomogeneous adsorption onto the substrate is therefore observed on  $\text{Al}_2\text{O}_3$ . That is comparable to what has been reported for  $\text{TiO}_2$ .<sup>3,7</sup> This leads to the presence of different dye configurations at the semiconductor surface; not all of them being accessible to iodide in the same way. This might be also the reason for the low yield (10-15 %) of reductive quenching observed in the two-color pump-probe experiment, when probing at 630 nm.

In addition, the reported second time component of the SVD (in PMII) has a lifetime of 5 ps, very close to the one reported in the the two colors experiment. Unfortunately, this component has never been found during the global fitting procedure. Nevertheless, this observation confirms an inhomogeneity in dye adsorption, leading to an inhomogeneity in reductive quenching time constants.

### Femtosecond transient absorbance conclusions

Observing the transient absorbance at 860 nm did not help to identify the reductive quenching. Nevertheless measurements with 630 nm probe highlighted reductive quenching onto  $\text{Al}_2\text{O}_3$ . This is the first report of reductive quenching of N719 by iodide on this inert substrate, in other words without electron injection. Even on this substrate, only 15 % of the dye appears to be accessible to iodide reduction. The reaction takes place in the picosecond time domain, with  $\tau = 6.9$  ps. In a white-light-continuum probe experiment and in the presence of PMII, a DAS with a  $\tau = 19.2$  ps is reported. The DAS shows that the reduced species has no positive absorbance across the wavelength domain studied. Contrarywise, its appearance induces an increase in the bleaching signal centered at 540 nm. This discrepancy between the time constant reported in two distinct experiments is explained by the inhomogeneity of the adsorption of the dye onto the semiconductor surface.

## 3.4 Conclusions and outlook

This work achieved a deeper investigation on the reductive quenching (equation 3.5) reported as an alternative pathway in the reaction scheme of a DSSC.<sup>1,2</sup> Direct interception of the excited state of the sensitizer by iodide has been observed onto  $\text{Al}_2\text{O}_3$  substrate, i.e. without electron injection. This has been already attempted in the work of Bernard Wenger, but without success.<sup>2</sup> The only evidences reported were onto titania and therefore in the case of electron transfer between the dye and the semiconductor.

The strategy deployed herein is the use of  $\text{Al}_2\text{O}_3$  substrate, a semiconductor with conduction band potential which is low and, as a consequence, does not allow for electron transfer from the dye. It is therefore not sensitized, but has dye adsorbed onto it. Dyes used for this study are state of the art ruthenium complexes, namely N719 and Z907 analogues.

Previously, the origins of this reaction have been related to the presence of dye aggregates onto the surface of the semiconductor. It has therefore been

related with the slow time components of the electron injection dynamics into  $\text{TiO}_2$ . As a consequence, reductive quenching of N719 is believed to lie within a timescale of tens of picoseconds. At such short times, iodide ions in the mesoporous network might be considered as frozen.

This is easily explained at the very high concentrations of iodide used. A concentration of iodide of 6.1 M corresponds to an average distance between two adjacent iodide ions of 4 Å<sup>iii</sup>. This value is 2 orders of magnitude smaller than the mean diameter of the pores.

This is in accordance with the formation of an adduct between iodide ion and the ruthenium complex.<sup>41,42</sup> A second possibility is to have an iodide derivative replacing one ligand.<sup>43</sup> These interaction imply efficient ion pairing. Such pairing is favoured by the use of 6.1 M iodide PMII ionic liquid. The calculated value of 4 Å is in fact very close to the value reported for a  $\text{Ru}(\text{bpy})_2(\text{deeb})_2^+$  complex<sup>iv</sup>. Crystallographic data show that two iodide counterions are associated with a single deeb ligand with an interionic distance between the iodides of 6.246 Å.<sup>42</sup> In addition, any attempt of direct observation of reductive quenching in solution failed for N719 and Z907 compounds and therefore did not permit to present a Stern-Volmer analysis of the luminescence quenching. This is mainly due to the form of reaction 3.5 with iodide. The electron donor which is favoured is the form illustrated in the reaction 3.10, involving two iodides. This oxidation of iodide to  $\text{I}_2^-$  is thermodynamically more favorable than the reaction 3.9, leading to iodine atom.<sup>24</sup> Therefore, the formation of  $(\text{I}^- \cdots \text{I}^-)$  or  $(\text{S} \cdots \text{I}^-)$  pairs might be a prerequisite for the reaction to efficiently occur.



Nevertheless an indirect observation of the reductive quenching was made

<sup>iii</sup>This value is calculated from the concentration and a law of distribution of the nearest neighbor in a random distribution of particles<sup>40</sup>

<sup>iv</sup>bpy is 2,2-bipyridine and deeb is 4,4'-( $\text{CO}_2\text{CH}_2\text{CH}_3$ )<sub>2</sub>-2,2'-bipyridine

possible upon adsorption onto a surface, here  $\text{Al}_2\text{O}_3$ . This is again attributed to the high iodide concentration needed for significant static dye-iodide adduct formation which is not attainable in solution. All of these observations strongly support a static mechanism.

A photoinduced absorption spectroscopy study first lead to the spectral shape of the reduced ruthenium dye. The latter has never been prepared chemically, every attempt leading to irreversible degradation of the compound. Therefore, only the photoinduced reaction remains available. Unfortunately, onto  $\text{Al}_2\text{O}_3$  a strong emission masks any potential transient species. Nevertheless, upon adsorption onto  $\text{TiO}_2$  two absorption bands associated with the formation of the dye anion are revealed. At first, a positive transient absorbance below 520 nm is assigned to the transient dye anion absorbance as it does not correspond to any iodine species.<sup>44</sup> Secondly, a broad featureless positive transient absorbance is observed over the whole NIR spectrum, from 800 up to 1600 nm. It is clearly more intense than the absorbance of the electrons in the  $\text{TiO}_2$ . This transient absorbance is not clearly attributed to the reduced dye as it might arise from some atomic iodine species. However an attempt to photochemically oxidize iodide (from  $\text{LiI}$ ) with 10-methylacridinium perchlorate under UV light did not present any specific absorbance in this region of the spectrum (data not shown) and therefore supports attribution of this positive NIR transient absorbance to the dye anion.

Pump-probe transient absorbance measurements revealed at 630 nm direct observation of excited dye reduction. This reaction is achieved with a 6.9 ps time constant and its amplitude is rather low, concerning no more than 15 % of the dye. This observation is a clear proof of this reaction being able to compete with the slowest components of electron injection, when the dye is adsorbed onto a substrate such as  $\text{Al}_2\text{O}_3$  or  $\text{TiO}_2$ .

To confirm this, measurements with a white-light-continuum probe have been carried out. These measurements also lead to direct observation of reductive quenching of the dye by iodide, adding information over the whole

visible. The time constant reported after a global fit of the data is  $\tau = 19.2$  ps for the reductive quenching.

The origin of this discrepancy in the reported time components is attributed to inhomogeneous adsorption of the dye onto the surface. Both results are found within in the same timescale, but with a significant difference, the second result having treble duration than the first one. These two results are compatible with a competition with the slow components of the electron injection and therefore with the timescale reported onto  $\text{TiO}_2$ .<sup>2</sup> This difference has been found to be caused by the adsorption inhomogeneities of the dye onto the surface. This explanation can be transferred to the  $\text{Al}_2\text{O}_3$  case for explaining the different time constants observed. They are different samples, presenting different access to the surface for iodide.

This unwanted reaction is of interest when developing new electrolytes. The typical properties of ionic liquids, such as non-volatility, electrochemical stability and high conductivity, render them attractive as electrolytes for dye-sensitized solar cells.<sup>16</sup> But one has to be aware of potential drawbacks, such as the use of unusual concentrations, favouring alternative reaction schemes, which might, as the reductive quenching pathway, lower the charge separation yield.



## 3.5 References

1. Teuscher, J. *Investigation de l'agrégation de complexes polypyridyles de ruthénium (II) à la surface d'oxydes nanocristallins par photolyse par éclair laser*, Travail Pratique de Diplôme, LPI, École Polytechnique Fédérale de Lausanne, **2004**.
2. Wenger, B. *Effect of Electronic and Nuclear Factors on the Dynamics of Dye-to-Semiconductor Electron Transfer*, Thèse École Polytechnique Fédérale de Lausanne no. 3447, **2006**.
3. Wenger, B.; Grätzel, M.; Moser, J. E. *J. Am. Chem. Soc.* **2005**, *127*, 12150–12151.
4. Nasr, C.; Hotchandani, S.; Kamat, P. V. *J. Phys. Chem. B* **1998**, *102*, 4944–4951.
5. Thompson, D.; Kelly, C.; Farzad, F.; Meyer, G. J. *Langmuir* **1999**, *15*, 650–653.
6. Bergeron, B.; Meyer, G. J. *J. Phys. Chem. B* **2003**, *107*, 245–254.
7. Teuscher, J.; Moser, J. E.; Grätzel, M. *J. Am. Chem. Soc.* **2010**, in prep.
8. Antila, L. J.; Heikkilä, M. J.; Aumanen, V.; Kemell, M.; Myllyperkiö, P.; Leskelä, M.; Korppi-Tommola, J. E. I. *J. Phys. Chem. Lett.* **2009**, 536–539.
9. Pelet, S.; Grätzel, M.; Moser, J. E. *J. Phys. Chem. B* **2003**, *107*, 3215–3224.
10. Nazeeruddin, M. K.; Zakeeruddin, S.; Humphry-Baker, R.; Jirousek, M.; Liska, P.; Vlachopoulos, N.; Shklover, V.; Fischer, C.; Grätzel, M. *Inorg. Chem.* **1999**, *38*, 6298–6305.
11. Wang, P.; Zakeeruddin, S.; Moser, J. E.; Nazeeruddin, M. K.; Sekiguchi, T.; Grätzel, M. *Nat. Mater.* **2003**, *2*, 402–407.
12. Wang, P.; Zakeeruddin, S.; Comte, P.; Charvet, R.; Humphry-Baker, R.; Grätzel, M. *J. Phys. Chem. B* **2003**, *107*, 14336–14341.
13. Zakeeruddin, S.; Nazeeruddin, M. K.; Humphry-Baker, R.; Pechy, P.; Quagliotto, P.; Barolo, C.; Viscardi, G.; Grätzel, M. *Langmuir* **2002**, *18*, 952–954.
14. Wang, P.; Zakeeruddin, S.; Exnar, I.; Grätzel, M. *Chem. Commun.* **2002**, 2972–2973.

15. Papageorgiou, N.; Athanassov, Y.; Armand, M.; Bonhôte, P.; Pettersson, H.; Azam, A.; Grätzel, M. *J. Electrochem. Soc.* **1996**, *143*, 3099–3108.
16. Zakeeruddin, S.; Grätzel, M. *Adv. Funct. Mater.* **2009**, *19*, 2187–2202.
17. Wang, P.; Wenger, B.; Humphry-Baker, R.; Moser, J. E.; Teuscher, J.; Kantlehner, W.; Mezger, J.; Stoyanov, E.; Zakeeruddin, S.; Grätzel, M. *J. Am. Chem. Soc.* **2005**, *127*, 6850–6856.
18. Palomares, E.; Clifford, J.; Haque, S.; Lutz, T.; Durrant, J. R. *J. Am. Chem. Soc.* **2003**, *125*, 475–482.
19. Sauve, G.; Cass, M.; Coia, G.; Doig, S.; Lauermann, I.; Pomykal, K.; Lewis, N. S. *J. Phys. Chem. B* **2000**, *104*, 6821–6836.
20. Ardo, S.; Meyer, G. J. *Chem. Soc. Rev.* **2009**, *38*, 115–164.
21. Nazeeruddin, M. K.; Kay, A.; Rodicio, I.; Humphry-Baker, R.; Muller, E.; Liska, P.; Vlachopoulos, N.; Grätzel, M. *J. Am. Chem. Soc.* **1993**, *115*, 6382–6390.
22. Tachibana, Y.; Moser, J. E.; Grätzel, M.; Klug, D. R.; Durrant, J. R. *J. Phys. Chem-Us* **1996**, *100*, 20056–20062.
23. Boschloo, G.; Hagfeldt, A. *Inorganica Chimica Acta* **2008**, *361*, 729–734.
24. Pelet, S.; Moser, J. E.; Grätzel, M. *J. Phys. Chem. B* **2000**, *104*, 1791–1795.
25. Rothenberger, G.; Fitzmaurice, D.; Grätzel, M. *J. Phys. Chem-Us* **1992**, *96*, 5983–5986.
26. Hannappel, T.; Burfeindt, B.; Storck, W.; Willig, F. *J. Phys. Chem. B* **1997**, *101*, 6799–6802.
27. Kallioinen, J.; Benkö, G.; Myllyperkiö, P.; Khriachtchev, L.; Skarman, B.; Wallenberg, R.; Tuomikoski, M.; Korppi-Tommola, J. E. I.; Sundström, V.; Yartsev, A. P. *J. Phys. Chem. B* **2004**, *108*, 6365–6373.
28. Asbury, J.; Ellingson, R.; Ghosh, H. N.; Ferrere, S.; Nozik, A.; Lian, T. *J. Phys. Chem. B* **1999**, *103*, 3110–3119.
29. Kallioinen, J.; Benkö, G.; Sundström, V.; Korppi-Tommola, J. E. I.; Yartsev, A. P. *J. Phys. Chem. B* **2002**, *106*, 4396–4404.

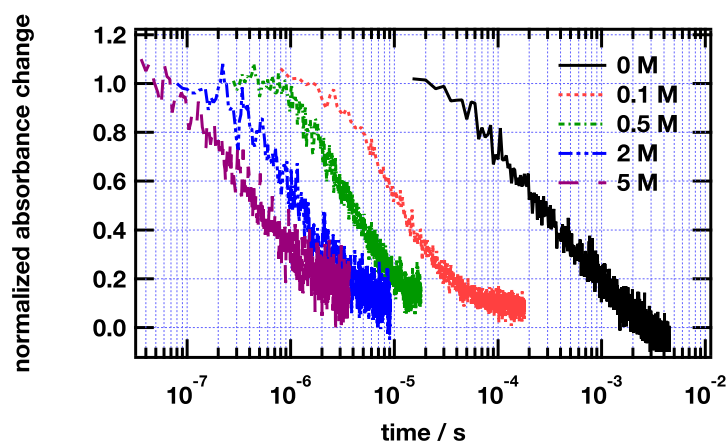
- 
30. Bhasikuttan, A.; Suzuki, M.; Nakashima, S.; Okada, T. *J. Am. Chem. Soc.* **2002**, *124*, 8398–8405.
31. Cannizzo, A.; van Mourik, F.; Gawelda, W.; Zgrablic, G.; Bressler, C.; Chergui, M. *Angew Chem Int Edit* **2006**, *45*, 3174–3176.
32. Moser, J. E.; Noukakis, D.; Bach, U.; Tachibana, Y.; Klug, D. R.; Durrant, J. R.; Humphry-Baker, R.; Grätzel, M. *J. Phys. Chem. B* **1998**, *102*, 3649–3650.
33. Benkö, G.; Kallioinen, J.; Korppi-Tommola, J. E. I.; Yartsev, A. P.; Sundström, V. *J. Am. Chem. Soc.* **2002**, *124*, 489–493.
34. Durrant, J. R.; Tachibana, Y.; Mercer, I.; Moser, J. E.; Grätzel, M.; Klug, D. R. *Z. Phys. Chem.* **1999**, *212*, 93–98.
35. Tachibana, Y.; Haque, S. A.; Mercer, I.; Durrant, J. R.; Klug, D. R. *J. Phys. Chem. B* **2000**, *104*, 1198–1205.
36. Tachibana, Y.; Nazeeruddin, M. K.; Grätzel, M.; Klug, D. R.; Durrant, J. R. *Chem. Phys.* **2002**, *285*, 127–132.
37. Asbury, J.; Anderson, N.; Hao, E.; Ai, X.; Lian, T. *J. Phys. Chem. B* **2003**, *107*, 7376–7386.
38. Kuciauskas, D.; Monat, J.; Villahermosa, R.; Gray, H.; Lewis, N. S.; McCusker, J. K. *J. Phys. Chem. B* **2002**, *106*, 9347–9358.
39. Satzger, H.; Zinth, W. *Chem. Phys.* **2003**, *295*, 287–295.
40. Chandrasekhar, S. *Rev Mod Phys* **1943**, *15*, 0001–0089.
41. Clark, C.; Marton, A.; Meyer, G. J. *Inorg. Chem.* **2005**, *44*, 3383–3385.
42. Marton, A.; Clark, C.; Srinivasan, R.; Freundlich, R.; Sarjeant, A.; Meyer, G. J. *Inorg. Chem.* **2006**, *45*, 362–369.
43. Agrell, H.; Lindgren, J.; Hagfeldt, A. *J. Photoch. Photobio. A* **2004**, *164*, 23–27.
44. Gardner, J. M.; Abrahamsson, M.; Farnum, B. H.; Meyer, G. J. *J. Am. Chem. Soc.* **2009**, *131*, 16206–16214.



# Chapter 4

## Iodide concentration dependance of sensitizer cations interception dynamics

### Graphical abstract



Dynamics of C203 dye cation, varying the iodide concentration

## 4.1 Introduction

A redox mediator is used in DSSCs for the regeneration of the dye ground state by electron transfer prior to recombination with the injected electron. The product of this reaction, the oxidized form of the redox mediator, transports the charge and is then reduced at a counter electrode. In the model case studied, involving half cells, there is no counter electrode, so the oxidized mediator regenerates with the injected electrons. This second process is out of the scope of this study.

The triiodide/iodide redox couple is the preferred redox couple in DSSC development. It still yields the most stable and efficient cells. This couple has several interesting properties. It has a suitable redox potential and does not absorb too much light. Its solubility is excellent, especially when used in molten salts that allow for the required very high iodide concentrations. In addition, the reduction of the triiodide species on the surface of  $\text{TiO}_2$  is very slow and therefore limits the dark current generation.<sup>1</sup> The triiodide/iodide couple is not reversible on doped thin oxide. No short circuit in case the electrolyte contacts the collecting electrode below  $\text{TiO}_2$ . Therefore no blocking layer is necessary.

The regeneration timescale for the ruthenium sensitizer N719<sup>i</sup> in the presence of about 0.5 M iodide is in the range of a microsecond.<sup>2</sup>

The chemical details of iodide oxidation with transition-metal compounds in solution have been known for a long time. But the detailed knowledge of the redox chemistry at sensitized electrodes is more recent.<sup>3</sup>

### 4.1.1 Reaction scheme

The basis for the reaction scheme following light absorption in a DSSC-like system are presented in section 3.1.1. In consequence, they will only be summarized here, such as the different steps illustrated in figure 4.1.

---

<sup>i</sup>bis(tetrabutylammonium)[cis-di(thiocyanato)-bis(2,2'-bipyridyl-4-carboxylate-4'-carboxylic acid)-ruthenium(II)]

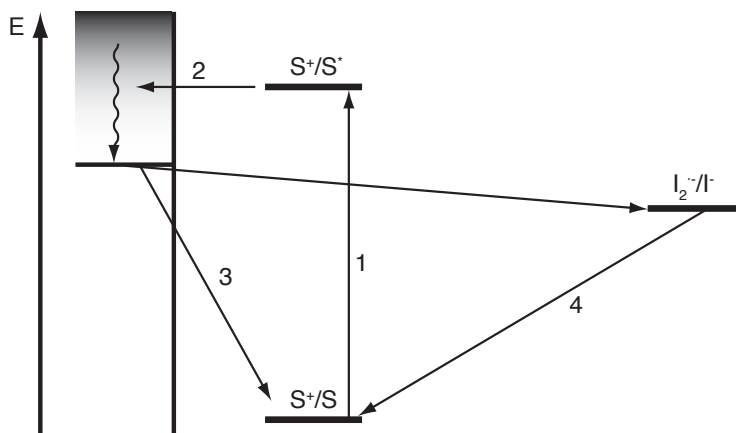
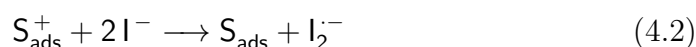


Figure 4.1: Reaction scheme of a sensitizer S at the photoanode of a DSSC in the presence of a donor D. 1. light absorption; 2. electron injection into the semiconductor; 3. recombination of the dye cation with an injected electron; 4. dye cation interception by the donor.

The reaction of interest in this study is the ground state regeneration reaction (also called the dye cation interception) 4.2 (number 4 on figure 4.1), and its dependance to the iodide concentration. The formation of I<sub>2</sub><sup>-</sup> is of particular relevance as the driving force for dye regeneration will be directly related to the (I<sub>2</sub><sup>-</sup>/I<sup>-</sup>) redox couple. Without any charge collection, I<sub>2</sub><sup>-</sup> disproportionates, forming the I<sub>3</sub><sup>-</sup> and I<sup>-</sup> species.



### 4.1.2 State of the art

The literature is very rich in tentative explanations about the interception mechanism of ruthenium dye cations. However, reports of interception dynamics for organic D- $\pi$ -A dye cations remains poor.

The first report of ruthenium(III)-polypyridyl compound regenerated by iodide on the surface of titania has been published in 1988.<sup>4</sup> However these measurements involved an iodide salt (KI) dissolved in water.

Since this first study, a large number of studies aimed at abstracting the rate at which the dye ground state is regenerated. The knowledge about the regeneration mechanism is crucial to DSSCs development and especially the relationship between the dye structure and the regeneration rate.

Most of the reports use transient absorption spectroscopy based on the oxidized dye absorption or ground state bleaching. This is a good way for quantifying rate constants, but does not give much information regarding the intrinsic mechanisms of the reduction.

### **Iodide-based redox couple**

The absorption spectrum of the different iodide-derived species is known over the visible.  $I_3^-$  does not absorb significantly above 450 nm but  $I_2^-$ , besides a peak centered at 400 nm, absorbs light around 700 nm,<sup>5</sup> but with a small  $\epsilon = 2000 \text{ l} \cdot \text{mol}^{-1} \cdot \text{cm}^{-1}$ . As a consequence, this should not influence the transient dynamics recorded at 650 nm. It could only add a small DC component to the measured data, that doesn't reach a real zero after the interception of the dye cations.

Contrary to working DSSC devices, most of the following study is performed with only iodide and not a complete regenerating electrolyte. The first difference is the absence of iodine. As a consequence, the real iodide ion is present in the studied solutions and not a mixture of triiodide and iodide as it is the case in usual electrolytes. However and because of the formation of  $I_2^-$  during the photo-cycle, the presence of some triiodide species is unavoidable.<sup>1</sup>

### **Iodide-dye interactions**

$TiO_2$  surface is acidic and therefore binds most of the species in the electrolyte to some degree. It is clear that the understanding of the absorption/desorption of the different ionic species contained in electrolytes is crucial. Especially because the iodide interception of  $S^+$  involves two iodides, its adsorption is crucial. The ratio between the number of solvent molecules



to the ionic species, within a pore of 20 nm diameter is also relevant. Not only the titania surface but also the dye, either in its ground or excited state, might bind iodide species, especially in the case of ruthenium dyes.<sup>6</sup>

The reaction of a ruthenium dye ground state and oxidized form with one iodide ion might lead to the formation of an intermediate complex.<sup>2,7,8</sup> The subsequent reaction of this complex with a second iodide ion, leading to the reduction of the dye cation, forms  $I_2^-$ . It is shown to be, kinetically and thermodynamically, the limiting step in the overall regeneration reaction.<sup>9</sup> Also, a working cell has to have an iodide and triiodide gradient for efficient work.

The interception of ruthenium tris(bipyridyl) dye cation also suggested a difference between the bulk iodide concentration and the concentration in the vicinity of the dye, revealing the importance of the titania surface charge.<sup>10</sup> This has been highlighted as the dye regeneration appears being faster when using cations such as  $Li^+$  in the electrolyte. This is attributed to a possibly higher local concentration of iodide in the  $TiO_2$  vicinity due to the adsorption of lithium cations.<sup>2</sup> Also in the case of a ruthenium phthalocyanine, a complex formation with iodine is postulated, leading to a local increase of iodide species.<sup>11</sup>

The isothiocyanato groups ( $-NCS$ ) of the ruthenium dyes can also be released from the dye and then form a complex with iodine species as observed with Raman spectroscopy.<sup>12</sup>

Interactions of iodide species with the reduced and oxidized ruthenium dye N3<sup>ii</sup> have been investigated by means of Density Functional Theory (DFT).<sup>13,14</sup> These studies revealed interactions between iodide and the sulfur atom of the isothiocyanate ligand as well as ligand exchange reactions between  $I^-$  and  $SCN^-$  moieties. Interactions of iodide with the bipyridyl rings of the dye are also proposed. Without being formerly identified, the formation of a bond between iodide and the dye is confirmed. These calculations bring new insights into the intrinsic mechanism of dye cation

---

<sup>ii</sup>cis-di(thiocyanato)-bis(2,2'-bipyridyl-4,4'-carboxylic acid)-ruthenium(II)

interception.

In the case of D- $\pi$ -A dyes, the absence of the isothiocyanate groups leads to the consideration of other interaction sites. For all the dyes studied, the  $\pi$ -bridge is found to contain thiophene units or derivatives. The sulfur atoms might therefore be an interacting site with iodide anions.

### Concentration dependance of the regeneration

In general and based on the N3/TiO<sub>2</sub> system, the use of a low concentration of iodide leads to a regeneration rate being first order in iodide. At higher concentrations, a static component is often observed.

A few studies are found that observe the dye regeneration on the surface of dye-sensitized TiO<sub>2</sub> electrodes as a function of the iodide concentration. A repulsive mechanism is observed and highlight the need for using a high enough iodide concentration for quantitatively regenerating Z907Na dye.<sup>15</sup> At moderate iodide concentrations ( $[I^-] \leq 100$  mM), the kinetic redundancy between the regeneration (reaction 4.2) and the recombination (reaction 4.1) is still important and therefore the results obtained at  $[I^-] \geq 0.1$  M represent the regeneration reaction.<sup>16</sup> In the present study, the concentration range investigated lies from 0.1 M up to 6.1 M iodide.

## 4.2 Experimental part

### 4.2.1 Chemicals

#### Dyes

Two amphiphilic ruthenium dyes are used in this study, Z907Na<sup>iii</sup> and N820<sup>iv</sup>. These dyes have alkyl substituents of different length (nonyl and methyl groups, respectively) grafted onto the ligand that faces the surrounding

<sup>iii</sup>sodium[*cis*-di(thiocyanato)-(2,2'-bipyridyl-4-carboxylate-4'-carboxylic acid)(4,4'-diononyl-2,2'-bipyridyl)-ruthenium(II)]

<sup>iv</sup>*cis*-di(thiocyanato)-(2,2'-bipyridyl-4,4'-dicarboxylic acid)(4,4'-dimethyl-2,2'-bipyridyl)-ruthenium(II)

medium. They present similar absorption spectra as the chromophore groups are not affected.

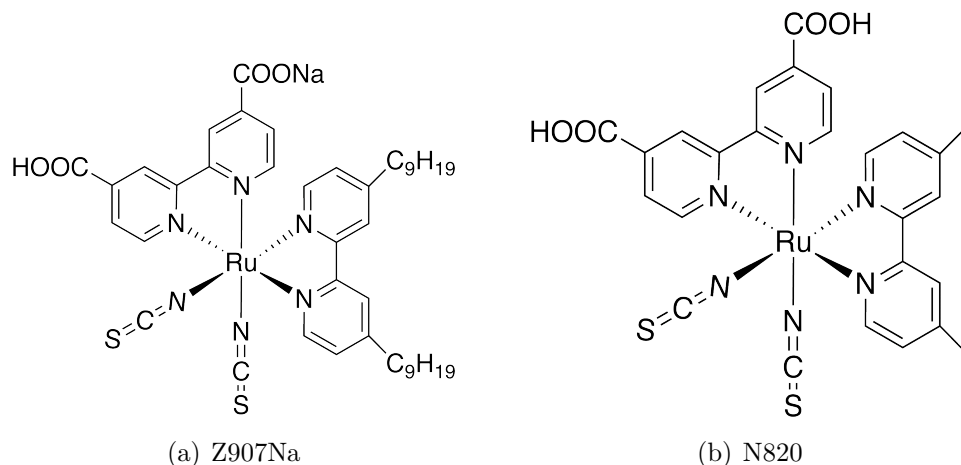


Figure 4.2: Molecular structure of ruthenium dyes.

Organic dyes are also studied, coded C201, C203, C204 and C205. They are D- $\pi$ -A organic dyes with the same donor and anchoring groups. Their common core is 3-{5'-[N,N-bis(9,9-dimethylfluorene-2-yl)phenyl]-*bridge*-5-yl}-2-cyanoacrylic acid. The triarylamine moiety is a common hole acceptor found in organic optoelectronics. It is present in different structures, such as spiro-MeOTAD<sup>v</sup>.<sup>17</sup> The  $\pi$ -conjugated bridge unit is composed of two or three fused thiophene rings for C201 and C203, respectively. In C204 and C205, one and two EDOTs<sup>vi</sup> moieties are used, respectively. This is illustrated in figure 4.4.

## Electrolytes

The electrolyte used in this study is iodide. It is made of dilutions of 1,3-propylmethylimidazolium iodide (PMII) ionic liquid in 3-methoxypropionitrile (MPN). This allows for preparing solutions ranging from 0 to 6.1 M

<sup>v</sup>2,2',7,7'-tetrakis-(N,N-di-p-methoxyphenylamine)-9,9'-spirobifluorene

<sup>vi</sup>3,4-ethylenedioxythiophene

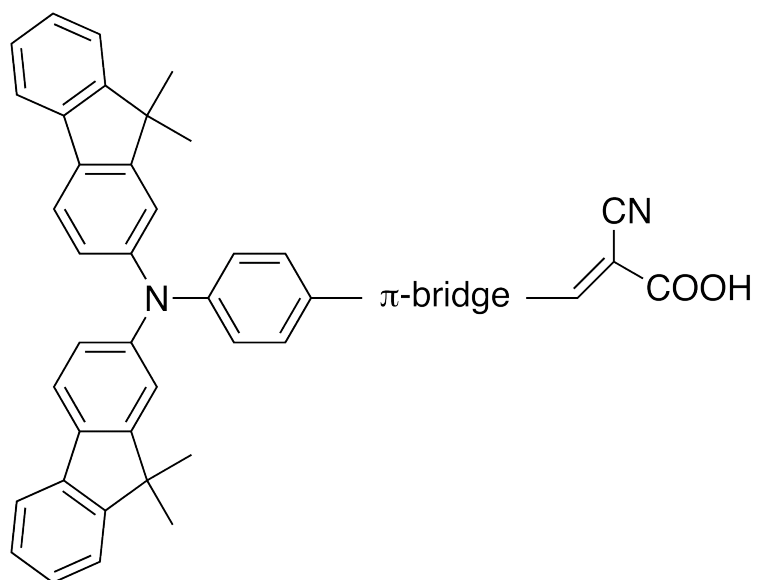


Figure 4.3: Molecular structure of organic D- $\pi$ -A dyes.

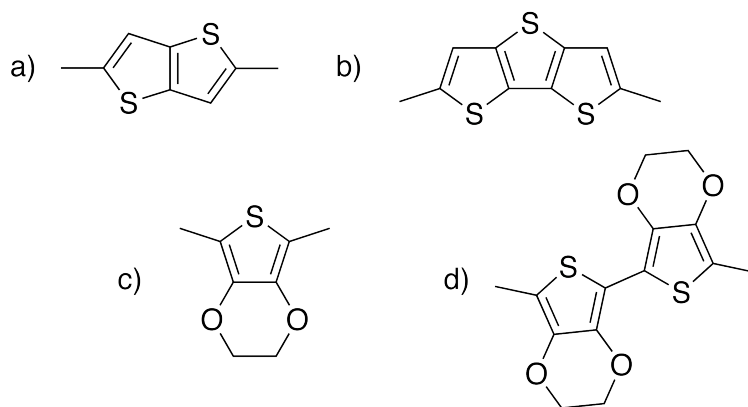


Figure 4.4: The four  $\pi$ -bridge units. a) two fused thiophenes, b) three fused thiophenes, c) EDOT, d) bis(EDOT).

iodide. Reaching such high iodide concentrations is the reason for the use of ionic liquid as the iodide source. Solutions of an iodide salt such as tetrapropylammoniumiodide (TPAI) does not allow to reach a concentration of 6 M. More details about PMII can be found in chapter 3.

For the experiment with Z907Na dye, a different electrolyte is used. It is a complex mixture, similar to the one used in functional DSSCs. It is described in the relevant section.

### **Titanium dioxide**

Anatase titanium dioxide ( $\text{TiO}_2$ ) films of 4.8 to 9.6  $\mu\text{m}$  thickness are used. They have a porosity of 0.625, allowing for high dye loading on a thin sample. Details on the preparation used can be found within chapters 2 and 3.

#### **4.2.2 Samples**

The films are immersed overnight in a dye solution. Prior to dyeing, the films are briefly warmed up to 200°C to avoid the presence of residual water within the porous network, and therefore favoring dye adsorption.

After dyeing, the films are rinsed with ethanol. Then they are covered with the desired electrolyte and a thin glass plate.

## **4.3 Results and discussion**

### **4.3.1 Fluence**

Charge recombination dynamics is strongly dependant on the excitation fluence.<sup>18</sup> To avoid this side effect, the excitation source is carefully monitored. The parameter of interest is then not only the laser power, but the fluence. This value is expressed in  $\text{J} \cdot \text{cm}^{-2}$ .

At high iodide concentrations, the fluence parameter is not crucial anymore as the interception reaction is monitored and does not depend on the fluence, i.e. on the number of injected electrons, but only on the

$I^-/S^+$  ratio (see section 4.3.2). However, measurement taken at lower iodide concentration might be affected.

To ensure that the observed dynamics do not depend on the fluence, a threshold is set at a level that guarantees that only one electron is injected per nanoparticle and thus only one oxidized dye species formed on each particle. In a mesoporous network, if the diffusion of injected electrons from one particle to another is slow compared to the electron-cation ( $e_{cb}^-|S^+$ ) recombination reaction, the ( $e_{cb}^-|S^+$ ) pair is confined within the volume of one single nanoparticle. A first order kinetics should prevail for the cases involving less or equal to one electron injected per nanoparticle. For a larger number of injected electrons, faster dynamics is expected, even reaching a second order dynamics for example when they are more than twenty electrons within one nanoparticle.<sup>19</sup>

The first assumption which is made in the following calculation is that the light is homogeneously absorbed through the sample. The real picture is probably different. The use of samples having large optical densities at the excitation wavelength, typically  $A \geq 1$ , implies that the light is attenuated through the film thickness. As a consequence, the light reaching the first layer of particles is one or two order of magnitude more intense than at the rear of the sample. This will causes a spread of the number of ( $e_{cb}^-|S^+$ ) pairs produced per nanoparticle. It will be seen as an inhomogeneity in the observed dynamics.

To correctly monitor the number of ( $e_{cb}^-|S^+$ ) pairs per nanoparticles, the first parameter to calculate is the number of nanoparticles per  $cm^2$  ( $n_{np}$ ). The diameter of a single nanoparticle is 16 nm and the porosity of the film is 0.625. This calculation is done for the illumination of 1  $cm^2$  of a film of 4.8  $\mu m$  thickness.

$$V_{np} = 2.14 \cdot 10^{-24} m^3 \quad (4.3)$$

$$V_{TiO_2} = (1 - porosity) \cdot V_{film} = 1.8 \cdot 10^{-10} m^3 \quad (4.4)$$

$$n_{np} = \frac{V_{\text{TiO}_2}}{V_{np}} = 8.39 \cdot 10^{13} \text{ cm}^{-2} \quad (4.5)$$

Such a film has a typical absorbance upon dyeing of more than 1 OD at the excitation wavelength. To calculate a safe limit, the calculations are made for 0 % transmittance. In this extreme case, every single photon is absorbed by the dye, so it can only lead to an overestimation of the number of injected electrons. The excitation wavelength is 530 nm light ( $3.75 \cdot 10^{-19}$  J). To have at most one injected electron per nanoparticle, then the number of incident photons has to equal the number of illuminated particles.

$$Fluence_{max} = E_{530} \cdot n_{np} = 3.15 \cdot 10^{-5} \text{ J} \cdot \text{cm}^{-2} \quad (4.6)$$

This result allows for a use of laser pulses with an energy of about  $30 \mu\text{J} \cdot \text{cm}^{-2}$  without affecting the reaction dynamics, even at the lower iodide concentrations. This condition is maintained for the results obtained through this chapter.

### 4.3.2 $\text{I}^-/\text{S}^+$ ratio

Another important parameter is the number of iodide available per dye cation at a certain concentration. Equation 4.2 shows that two iodide are needed per dye cation for the regeneration reaction to occur. It implies that the formation of iodide pairs is necessary. This might occur via several channels. The pairs can be formed around the dye, involving dye-iodide interaction. They can be formed onto the surface by iodide anchoring onto  $\text{Ti}^{\text{IV}}$  atoms as well. It can also be a mix of both mechanisms.

A rough estimate of the number of iodide available to each oxidized dye within the pores will therefore be helpful for having a better picture of a  $\text{TiO}_2$  pore.

Under the low excitation regime used in this study, about  $8.39 \cdot 10^{13} \text{ cm}^{-2}$  cations are formed. Within this same volume, the number of iodide anions can be calculated as the pore volume is known, as well as the bulk iodide

Table 4.1: Estimation of the  $I^-/S^+$  ratio.

$[I^-]$	$I^-/S^+$
0.01	22
0.1	215
0.5	1'076
1	2'153
3	6'458
6.1	13'130

concentration.

$$V_{pores} = porosity \cdot V_{film} = 3 \cdot 10^{-10} m^3 \cdot cm^{-2} \quad (4.7)$$

This approximation gives a better view to what an iodide concentration represents in terms of  $I^-/S^+$  ratio. Sample results are presented in table 4.1. Iodide is much more abundant than oxidized dye molecules under these conditions, even at the lower concentrations. This allows for the iodide concentration being seen as constant through the whole process, according to the great excess of reductant. These calculations are in accordance with the estimation of the pores occupancy reported by O'Regan *et al.*<sup>6</sup>

### 4.3.3 Reciprocal regeneration half-time

The kinetics observed can not systematically be fitted by a single exponential, according to a simple first-order law. Half reaction times are hence extracted for allowing the comparison of the different results with a single fit parameter.

A monoexponential time constant,  $\tau = 1/k_r$ , is related to the reaction half-time,  $t_{1/2}$ , according to the equation 4.8. On the curve presented on figure 4.5, the single exponential fit (solid red line) gives a time constant,  $\tau = 116 \mu s$ . This corresponds to a  $t_{1/2} = 80 \mu s$ .

$$t_{1/2} = \ln(2) \cdot \tau \quad (4.8)$$



The experimentally measured half-time is the experimental time at which the absorbance change equals half of the initial absorbance change (equation 4.9).

$$\Delta A(t = t_{1/2}) = \frac{1}{2} \cdot \Delta A(t = 0) \quad (4.9)$$

A  $t_{1/2} = 57 \mu\text{s}$  is measured from the sample data shown on figure 4.5.

This difference between the empirical and analytical values shows that the use of a single exponential underestimates the regeneration rate in the presented case. This is due to the first fast part of the decay, which is only poorly fitted. A correct analytical fit would then need the addition of a second exponential component, rendering the comparison non-trivial. This early faster dynamics is on the other hand taken into account for the empirical half-time measured.

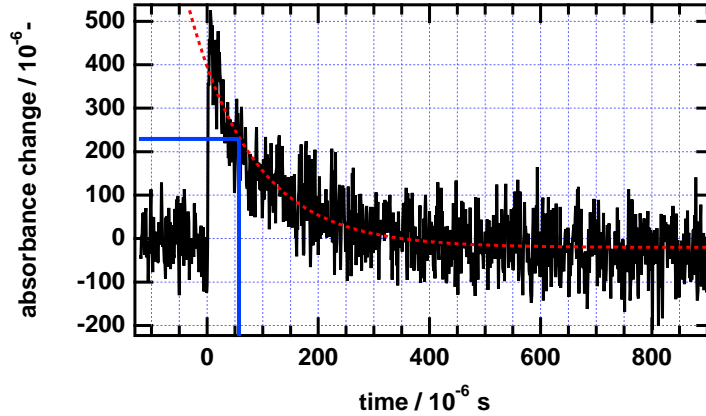


Figure 4.5: Nanosecond transient absorbance,  $\lambda_{obs} = 650 \text{ nm}$ ,  $\lambda_{ex} = 600 \text{ nm}$ , N820/TiO<sub>2</sub> in MPN. Single exponential fit (dashed red line) and reciprocal half-time analysis (solid blue lines) comparison.

This simple method allows for a good description of the observed dynamics with the use of only one parameter. This will help a straight comparison between the different measurements.

### 4.3.4 Ruthenium dyes

#### N820 dye

N820 cation has an experimental lifetime of 60  $\mu\text{s}$  in pure MPN.<sup>20</sup> It corresponds to a rate constant  $k_b = 16'600 \text{ s}^{-1}$ . This corresponds to the observation of the recombination reaction (reaction 4.1). In a 0.1 M iodide environment, the observed rate constant for the decay of the oxidized dye is  $k = 30'000 \text{ s}^{-1}$ . This shorter lifetime is assigned to the regeneration reaction (reaction 4.2). For all concentrations greater than 0.1 M, the rate constant increases and therefore reflects the efficiency of the dye cation interception by iodide.

The transient absorbance is monitored at 650 nm to observe the dye cation evolution,<sup>21</sup> upon 600 nm excitation. Figure 4.6 represents the extracted pseudo-first order rate constant of regeneration versus the iodide concentration in the bulk. The iodide concentration ranges from 0.1 M up to 2.5 M.

The observed pseudo-first order rate constant,  $k = 1/\tau$ , increases with the concentration and reaches a plateau at around 1.5 M. This behavior suggests an attractive mechanism and therefore the formation either of  $(\text{S}^+ \cdots \text{I}^-)$  or  $(\text{I}^- \cdots \text{I}^-)$  pairs.<sup>2</sup> The formation of a  $(\text{S} \cdots \text{I}^-)$  pair prior to electron injection leads to the same situation as a pair formed with the oxidized dye. In particular, the isothiocyanate groups of the dye can have interactions with iodide.<sup>8,12</sup>

Adsorption of iodide ions onto the surface might also occur and can be responsible for such a behavior. However, the surface of the  $\text{TiO}_2$  used in this study is on average negatively charged. The  $\zeta$ -potential (zeta-potential) of a  $\text{TiO}_2$  nanoparticle dyed with Z907 dye is estimated at -20 mV from Dynamic Light Scattering measurement of a solution containing a crushed dyed film.

Therefore,  $(\text{I}^- \cdots \text{I}^-)$  pairs are unlikely to form on the semiconductor surface under these conditions and will not be discussed. Nevertheless this possibility is not completely ruled out as  $\text{TiO}_2$  surface might be locally

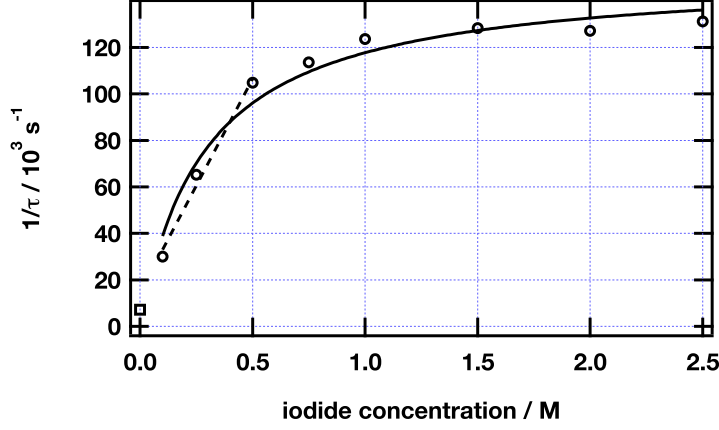
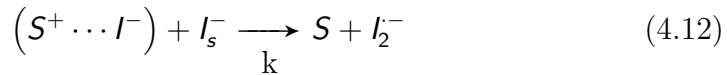
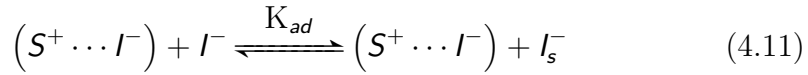
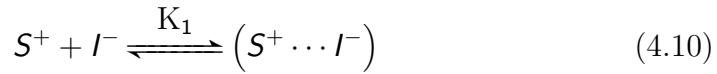


Figure 4.6: Regeneration rate constant ( $1/\tau = k$ ) of the oxidized dye as a function of the bulk iodide concentration. The solid curve is a Langmuir-like fit of the data. The dashed line corresponds to a slope of  $1.8 \cdot 10^5 \text{ M}^{-1} \cdot \text{s}^{-1}$ .

positively charged. The observed  $\zeta$ -potential is only an average potential at the location of the slipping plane versus a point in the bulk fluid away from the interface, which does not exactly represent the electric surface potential.

Two iodide ions have to be present in the vicinity of the oxidized dye for the regeneration reaction to occur and therefore, a second iodide has to be in the vicinity of this first ( $S^+ \cdots I^-$ ) pair. These consideration are described by the reactions 4.10, 4.11 and 4.12.



Equation 4.10 describes the prior formation of a pair between an iodide and the oxidized dye. It is a preliminary step to dye reduction by iodide and  $K_1$  is supposed to be larger than  $K_{ad}$  and might correspond to the association of iodide with an isothiocyanate ligand. Then, a second iodide has to encounter this pair, it will be called  $I_s^-$ , being associated to the surface

(equation 4.11).  $K_{ad}$  is the equilibrium constant for the adsorption of this second iodide ion.  $k$  is the pseudo first order reaction rate constant for reaction 4.12, the regeneration of the dye ground state.

The rate of reaction 4.12 depends on the number of occupied sites at a specific iodide concentration, in other words on the number of  $(S^+ \cdots I^-)$  pairs and on the number of  $I_s^-$ . According to the  $I^-/S^+$  ratio calculated in section 4.3.2, iodide is always in large excess and can be considered at a constant bulk concentration throughout the process.

This allows for writing the second order rate equation 4.13.

$$r = k'' \cdot [S^+ \cdots I^-] \cdot [I_s^-] \quad (4.13)$$

The observation of a first increase followed by the reaching of a plateau suggests that the local concentration of iodide,  $[I_s^-]$  might be greater than the average bulk concentration for the lower concentration values. The available sites are partially occupied up to about 1.5 M. At higher iodide concentrations, the observed rate constant is not dependant on  $[I_s^-]$  anymore. The sites are saturated by iodide ions and their occupation reaches a maximum,  $[I_s^-] = [I_s^-]_{max}$ . In this situation, the rate of dye reduction is governed by a maximum pseudo-first order rate constant, called  $k_{max} = k'' \cdot [I_s^-]_{max}$ .

A Langmuir-like isotherm equation is solved for the association mechanism found in reaction 4.11. In a Langmuir-like isotherm model,  $\theta$  is the fractional coverage of the surface. It can be calculated from the adsorption equilibrium constant  $K_{ad}$  and the free iodide concentration. The bulk iodide concentration will be used as the free iodide concentration,  $[I^-]$ .

$$\theta = \frac{K_{ad} \cdot [I^-]}{1 + K_{ad} \cdot [I^-]} \quad (4.14)$$

In the equation 4.14,  $\theta$  can be substituted by the ratio of the effective pseudo-first order rate constant to the maximum rate constant  $k_{max}$ , leading to equation 4.15.

$$k = k_{max} \cdot \frac{K_{ad} \cdot [I^-]}{1 + K_{ad} \cdot [I^-]} \quad (4.15)$$

The curve used for reproducing data in figure 4.6 is characterized by the parameters  $K_{ad} = 3.4 \text{ M}^{-1}$  and  $k_{max} = 152'000 \text{ s}^{-1}$ .

From the calculated adsorption constant, the association strength is estimated with the relation 4.16 at about  $3 \text{ kJ} \cdot \text{mol}^{-1}$ . It corresponds therefore to the strength of a van der Waals interaction, so it is a weak association between the second iodide,  $I_2^-$ , and the available site close to a  $(S^+ \cdots I^-)$  pair.

$$\Delta G = -R \cdot T \cdot \ln(K) = -3032 \text{ J} \cdot \text{mol}^{-1} \quad (4.16)$$

### Z907Na dye

The nonyl chains of Z907Na are responsible for its increased stability in DSSCs.<sup>22</sup> This advantage can also be a drawback, especially for the reductant to reach the active site. This is illustrated by the regeneration dynamics of Z907Na, which is slow compared to the reaction with reference dye N719. A difference of one order of magnitude in lifetime is observed between the two compounds.<sup>15</sup> Also, the experimental lifetime ( $t_{1/2}$ ) of Z907Na cation is of  $400 \text{ } \mu\text{s}$  ( $k_b = 2'500 \text{ s}^{-1}$ ) in MPN. It is longer than that of N820 dye ( $80 \text{ } \mu\text{s}$ ).

The usual electrolyte comprises a variable concentration from 0 to 2.5 M of 1,3-propylmethylimidazolium iodide (PMII) in MPN. It contains also 0.15 M iodine, 0.1 M guanidinium thiocyanate and 0.5 M N-methylbenzimidazole (NMBI). Iodine associates readily to iodide, forming  $I_3^-$ , and therefore the concentration of free iodide is effectively slightly smaller than the real amount of iodide molten salt added.

The transient absorbance is monitored at 680 nm to observe the dye cation evolution,<sup>15</sup> upon 600 nm excitation. Figure 4.7 represents the extracted pseudo-first order rate constant of regeneration versus the iodide abundance in the bulk. The iodide concentration range goes from 0.1 M up to 2.5 M. The

rate of regeneration (reaction 4.2) increases with the iodide concentration.

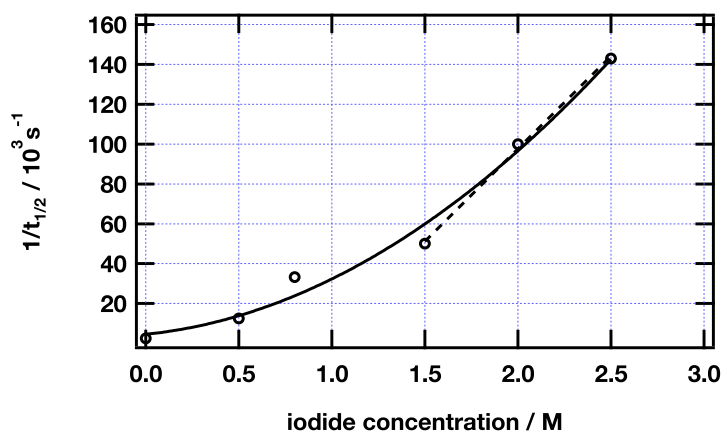


Figure 4.7: Regeneration rate constant ( $1/t_{1/2} = k$ ) of the oxidized dye as a function of the bulk iodide concentration. The solid curve is plotted for illustration. The dashed line corresponds to a slope of  $10^5 \text{ M}^{-1} \cdot \text{s}^{-1}$ . Adapted from.<sup>15</sup>

In contrast with the results obtained with N820 dye, the evolution of ( $1/t_{1/2}$ ) with the iodide concentration does not follow a Langmuir behavior. It shows an increase of the regeneration rate, even at higher concentrations. At 0.5 M iodide,  $t_{1/2}$  is equal to  $80 \mu\text{s}$ . This lifetime shortens to  $30 \mu\text{s}$  with 0.8 M iodide. Beyond this value,  $t_{1/2}$  is equal to 20, 10 and  $7 \mu\text{s}$  at 1.5, 2 and 2.5 M, respectively.

The value at 0.5 M corresponds to a pseudo-first order rate constant  $k = 18'000 \text{ s}^{-1}$ . This is much smaller than the  $104'000 \text{ s}^{-1}$  reported for N820 in the previous section. This confirms that the access of iodide to the active site is much more difficult in the presence of the long alkyl chains grafted onto Z907Na. Consequently, a repulsive behavior is postulated.

The slope of the function  $1/t_{1/2} = f([I^-])$  increases from a value of  $2 \cdot 10^4 \text{ M}^{-1} \cdot \text{s}^{-1}$  under  $[I^-] \leq 1.5 \text{ M}$  to approximately  $1 \cdot 10^5 \text{ M}^{-1} \cdot \text{s}^{-1}$  for  $[I^-] \geq 1.5 \text{ M}$ . As the iodide concentration exceeds 1.5 M, the slope seems to stay rather invariable. This allows for extracting a second order rate constant  $k'' = (t_{1/2} \cdot [I^-])^{-1} = 1 \cdot 10^5 \text{ M}^{-1} \cdot \text{s}^{-1}$ . In contrast, the attractive case of N820 dye, and even at the lower concentrations, leads to a higher

$k'' = 1.8 \cdot 10^5 \text{ M}^{-1} \cdot \text{s}^{-1}$  (figure 4.6).

### Ruthenium dyes conclusions

The study of the dependance of the iodide regeneration of ruthenium dye cations dynamics reveals two distinct cases.

At first an associative mechanism is proposed for a freely accessible dye, N820. Secondly, a prevailing repulsive interaction is found for a dye having long alkyl chains as a barrier, Z907Na. This observation is contrary to the report of Mori *et al.* who did not see an influence of the alkyl chain length to the interception reaction, but only in terms of the behavior versus the iodide concentration.<sup>23</sup> However, the reported lifetimes at the higher concentrations are similar.

In the attractive case, the static reactive concentration of iodide associated with the dye is larger than the bulk concentration at low iodide concentration. As the bulk iodide concentration increases, the available sites appear being saturated in redox mediator. On the contrary, the Z907Na pseudo-first order reaction rate constants reported,  $k = k'' \cdot [\text{I}_s^-]$ , indicate that the local concentration of iodide, close to the dye,  $[\text{I}_s^-]$ , is probably lower than the bulk concentration,  $[\text{I}^-]$ . This is revealed by a sublinear dependance to the concentration, below 1 M iodide.

At lower iodide concentrations, a Langmuir-like behaviour was also reported,<sup>24</sup> but these results are difficult to relate to the present study because the concentration range studied ranged only from 0 to 0.25 M in that case.

The values of the second order rate constants calculated are two orders of magnitude lower than what has been reported for N719 dye,<sup>2,25</sup> in which case  $k'' = 2 \cdot 10^7 \text{ M}^{-1} \cdot \text{s}^{-1}$ . In this latter case, lithium iodide (LiI) is used as an additive to modify the surface charge of  $\text{TiO}_2$ , rendering it positive. It could explain a more stronger attractive mechanism.

The comparison of the two ruthenium dyes shows that increasing the length of the alkyl chains results in a slowing of the dynamics, but only at

the lower concentrations. This can be related to what has been reported for a series of amphiphilic ruthenium dyes with alkyl chains of several lengths from 1 up to 18 carbons. At a constant concentration of iodide of 0.6 M, and therefore in the superlinear range of the Langmuir-like curve for N820, the trend is clearly indicating that the regeneration kinetics are related to the alkyl chain barrier length.<sup>26</sup> The longer is the barrier, the slower is the regeneration process.

#### 4.3.5 Organic D- $\pi$ -A dyes

C201, C203, C204 and C205 are organic dyes that only differ by their  $\pi$ -conjugated bridge. Their structure is presented on figure 4.3. As all the bridges investigated contain at least one sulfur atom, this part of the dye is likely to interact with the iodide species.

##### PIA spectroscopy

These state of the art organic D- $\pi$ -A dyes are not as well documented as the ruthenium bipyridyls complexes. As a consequence, preliminary measurements are performed to localize the spectral region where the dye cations can be probed in the nanosecond transient absorbance measurements. PIA is used for this purpose.

C201 and C203 exhibit residual emission on their PIA spectrum. It is centered at 620 nm for C201 and 660 for C203. Quenching of the excited state is therefore not complete for these two dyes. In other words, their electron injection yield into  $\text{TiO}_2$  does not reach unity. Such luminescence signals are not present in C204 and C205 dyes. The injection yield is therefore related to the presence of the thiophene units, versus the EDOTs moieties.

The emission of these D- $\pi$ -A dyes exhibits lifetimes shorter than 200 ps. As a consequence, these emissions will not be resolved in the nanosecond time-resolved measurement. The real shape of the dye cation absorbance will therefore not comprise this residual emission. C201, C203 and C204 have their maximum transient absorbance in the visible around 650 nm.



C205 presents a wider transient absorbance, centered at 700 nm. These will be the wavelength monitored for the time-resolved, transient absorbance measurement.

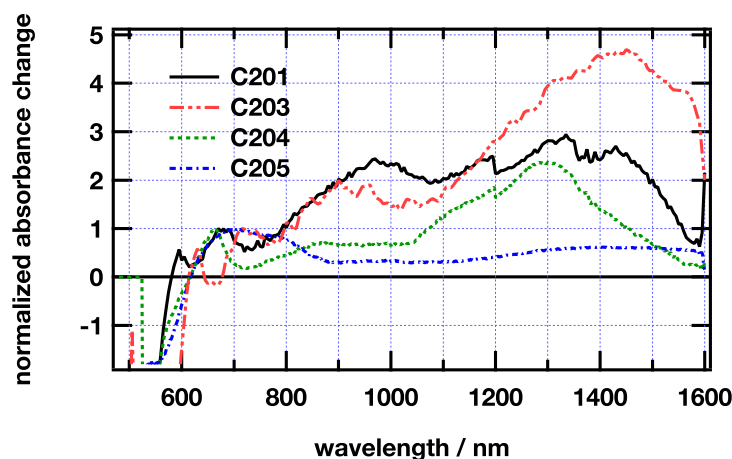


Figure 4.8: PIA spectra of C201/TiO<sub>2</sub> (—), C203/TiO<sub>2</sub> (---), C204/TiO<sub>2</sub> (···), C205/TiO<sub>2</sub> (-.-), 4.8  $\mu$ m,  $\lambda_{\text{ex}}$  = 470 nm at 9 Hz in air.

Another spectral feature observed on these spectra is a negative transient absorbance below 600 nm for the four dyes. It is attributed to the ground state bleaching. A broad positive transient absorbance in the NIR is also highlighted. It is assigned to the dye cation similarly to the positive absorbance change reported in the visible. Species containing triarylamine hole-acceptor units are known to present such spectral shapes, due to the localization of the hole on the amine.<sup>27</sup>

### Nanosecond transient absorbance

The transient absorbance is recorded for the four organic dyes over iodide concentrations ranging from 0.1 M up to 6.1 M. These electrolytes are dilutions of PMII in MPN. The samples have an absorbance value between 0.5 and 1 at the excitation wavelength.

C201 and C203 are excited at 525 nm, C204 is excited at 505 nm and C205 at 530 nm. For all the dyes, these values are at the red side of their

maximum visible absorption peak.

Figure 4.9 shows sample transient data for the C203 dye. The recombination reaction (4.1) is monitored by looking at the dye cation positive transient absorbance decrease in MPN, without any redox species added. Upon addition of 0.1 M of iodide, the ground state regeneration dynamics are increased by more than one order of magnitude. This is the reaction 4.2. The addition of iodide in larger concentrations continues to increase the regeneration rate.

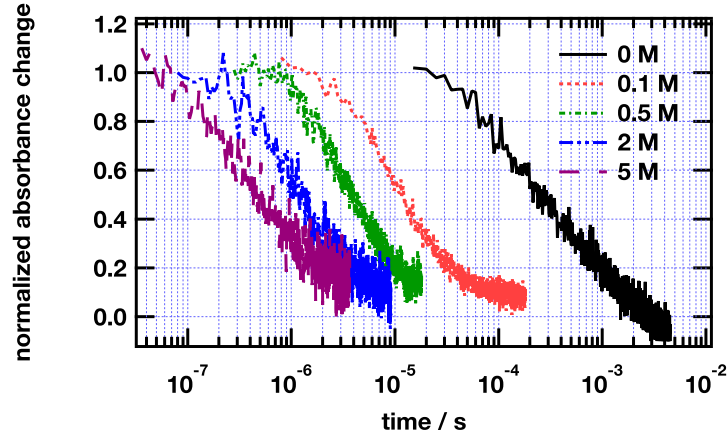


Figure 4.9: Nanosecond transient absorbance,  $\lambda_{obs} = 650$  nm,  $\lambda_{ex} = 525$  nm, C203/TiO<sub>2</sub>, several dilutions of PMII in MPN ( $[I^-]$ : (—) 0 M, (···) 0.1 M, (---) 0.5 M, (-·-) 2 M, (- -) 5 M).

At each concentration, the yield of oxidized dye interception can be calculated. This is achieved by applying relation 4.17.  $k = 1/t_{1/2}$  is the pseudo-first order rate constant for dye regeneration in the presence of iodide reductant species, while  $k_b$  is the rate constant in pure solvent, reflecting the back electron transfer reaction 4.1.

$$\eta_{reg} = \frac{k}{k + k_b} \quad (4.17)$$

These regeneration yields are calculated for C203 dye as an example.

With 1 M iodide, at least 99 % of the dye cations is regenerated by iodide. This indicates an efficient process for integration of these dyes into the DSSCs

Table 4.2: Ground state regeneration yields for C203 dye

$[I^-]$	$\eta_{reg}$
0.1 M	0.955
0.5 M	0.985
1 M	0.992
2 M	0.995
3 M	0.996
4 M	0.997
5 M	0.998
6.1 M	0.999

development.

This measurement is repeated for the three other dyes, resulting in a series of iodide concentration associated to each dye molecule.

The calculation of the regeneration yield does not reveal the large change in regeneration dynamics above 1 M iodide, but the lifetime reported versus the iodide concentration reveals significant dependence. This is illustrated for the four dyes in figure 4.10.

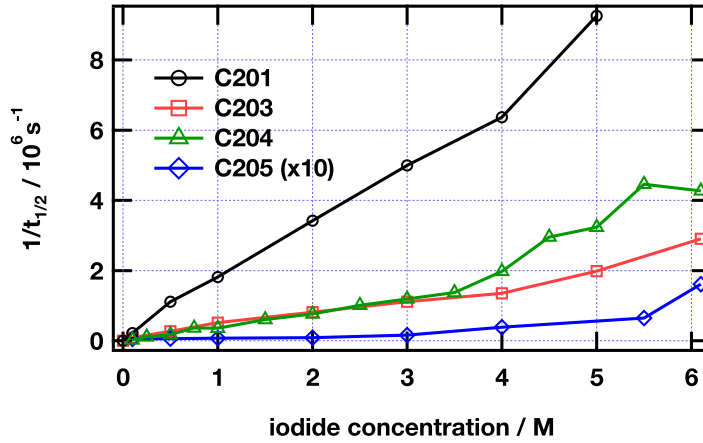


Figure 4.10: Regeneration rate constant ( $1/t_{1/2} = k$ ) of the oxidized dyes as a function of the bulk iodide concentration.

Firstly, the lifetime of the dye cation without electrolyte ranges from

245  $\mu\text{s}$  for C203 up to 1 ms for C201. Secondly, after addition of iodide the regeneration dynamics ranges over two orders of magnitude. C201 is the better intercepted dye, but C205 is only poorly regenerated. C203 and C204 exhibit similar timescale for the regeneration of their ground states.

Also the trend of the rate is different than what is observed with ruthenium dyes. None of the organic dye present an attractive behavior. On the contrary, C203, C204 and C205 evolve in a similar way to Z907Na and therefore are not likely to form the  $(\text{S}^+ \cdots \text{I}^-) \cdots \text{I}^-$  associations needed. This behavior is assigned to a repulsive interaction, leading to a lower slope at the lower iodide concentration values. It is the consequence of a weaker iodide concentration in the vicinity of the dye, than the bulk concentration.

C201 results exhibit a line, and therefore a real second order behaviour over the concentration range studied. The slope gives the second order rate constant  $k'' = (t_{1/2} \cdot [\text{I}^-])^{-1} = 1.73 \cdot 10^6 \text{ M}^{-1} \cdot \text{s}^{-1}$ . This value is one order of magnitude higher than for the ruthenium dyes studied.

C203 exhibits a different behaviour. As for the Z907Na case, two regions are identified. The slope of the function  $1/t_{1/2} = f([\text{I}^-])$  increases from a value of  $3.2 \cdot 10^5 \text{ M}^{-1} \cdot \text{s}^{-1}$  under  $[\text{I}^-] \leq 4 \text{ M}$  to approximately  $7.4 \cdot 10^5 \text{ M}^{-1} \cdot \text{s}^{-1}$  for  $[\text{I}^-] \geq 4 \text{ M}$ . A second order rate constant is extracted for the higher concentrations,  $k'' = 7.4 \cdot 10^5 \text{ M}^{-1} \cdot \text{s}^{-1}$ . It shows that it tends to a value similar to the C201 case.

C204 present a similar trend to C203, but with a steeper slope at the higher concentrations. A second order rate constant is extracted for the higher concentrations,  $k'' = 1.2 \cdot 10^6 \text{ M}^{-1} \cdot \text{s}^{-1}$ . It shows that it also tends to the value of the C201 case.

The C205 curve in figure 4.10 is expanded ten times for visual help. But the calculated slope reflects the real values. The maximum slope is only attained within the last two points and reaches a second order rate constant  $k'' = 1.6 \cdot 10^5 \text{ M}^{-1} \cdot \text{s}^{-1}$ . This value is still one order of magnitude smaller than for the other three dyes.

### Organic dyes conclusions

The regeneration rates for the dyes studied range over a broad time extent. C205, having two EDOTs units in its bridge is the dye which is only slowly regenerated, with a second order rate constant  $k'' = 1.6 \cdot 10^5 \text{ M}^{-1} \cdot \text{s}^{-1}$ . In comparison C201, having two fused thiophene units as a bridge, regenerates with a rate constant that is an order of magnitude larger, and from 0.1 M.

C201 is the only dye that does not present a region in which the iodide concentration is lower in the vicinity of the dye than in the bulk. The line shape of  $1/t_{1/2}$  reported versus the iodide concentration allows for considering a real second order reaction with  $k'' = 1.73 \cdot 10^6 \text{ M}^{-1} \cdot \text{s}^{-1}$ .

Oppositely, C203 and C204 dyes present a two phase behaviour. The first part results in an underestimated second order rate constant. This sublinear behaviour indicates that the iodide available for oxidized dye interception is smaller than the bulk concentration. After reaching a high enough concentration, the slope becomes invariant and  $[\text{I}^-]_{\text{bulk}} = [\text{I}_s^-]$ .

This change in the local concentration can arise from the dye structure. The fluorenes grafted onto the triarylamine hole-acceptor moiety are similar for the four dyes studied. Therefore, the access of iodide to the central amine should be similar. In addition, the anchoring group is a cyanoacrylate unit for the four dyes. As a consequence, no difference in adsorption nor aggregation onto the surface should be relevant.

The different bridges used in this study can be observed in terms of the potential interaction site they might have for accepting an iodide ion. Figure 4.11 is the schematic representation of a semi-empirical PM5 geometry optimization of the four dyes<sup>vii</sup>. The dyes are regularly distributed horizontally and aligned according to their anchoring group.

If an interaction occurs between the sulfur atoms of the  $\pi$ -conjugated bridges and the iodide, then the position of these groups might be relevant. The equilibrium of equation 4.10 has to be the first step of the regeneration. In the case of C201, both sulfur atoms might be available to an iodide. The

---

<sup>vii</sup>realised with the Scigress v.7.7.0.47 software

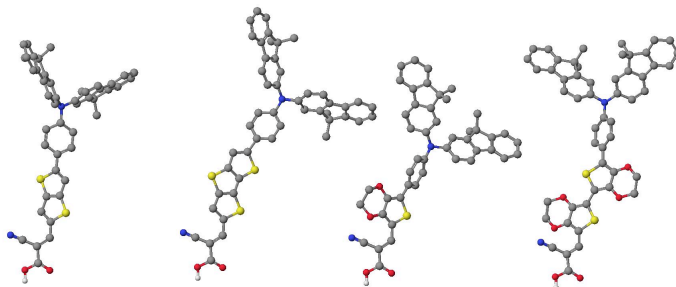


Figure 4.11: The four dyes sticks and balls representation. From left to right, C201, C203, C204 and C205.

situation is found similar for C203 and C204. However, C205 dye might have steric hindrance and the biggest two EDOT moieties might prevent iodide from associating with the sulfur atoms. Therefore, the meeting of two neighboring iodide atoms to complete the regeneration is less likely to occur and might be the cause for the slowest regeneration rate constant found for this molecule.

Because no maximum pseudo-first order rate constant is reached, the association of the dye with a second iodide (reaction 4.11) does not seem to occur in the case of these organic dyes. As a consequence, even reaching the highest iodide concentration still increases the pseudo-first order reaction rate constant.

## 4.4 Conclusions and outlook

This study of the interception rate of oxidized dyes by iodide contributed to the understandings of the interception mechanism in the DSSCs. Two different behaviors have been found.

The first one represent an associative, Langmuir-like adsorption behavior. It involves clearly the formation of a  $(S^+ \cdots I^-) \cdots I^-$  pair prior to the reaction

to complete. This associative mechanism is revealed by higher pseudo-first order rate constants at the lower concentrations, indicating a local concentration of iodide greater than in the bulk. It is favored by an attractive behavior between the dye and iodide.

Secondly a repulsive mechanism is found. It implies a sub-linear response at the lower iodide concentration, oppositely to the attractive case. After reaching a certain iodide bulk concentration, the second order rate constant is invariant and can be estimated.

These mechanisms are schematically depicted in figure 4.12 in a model graph summarizing the findings.

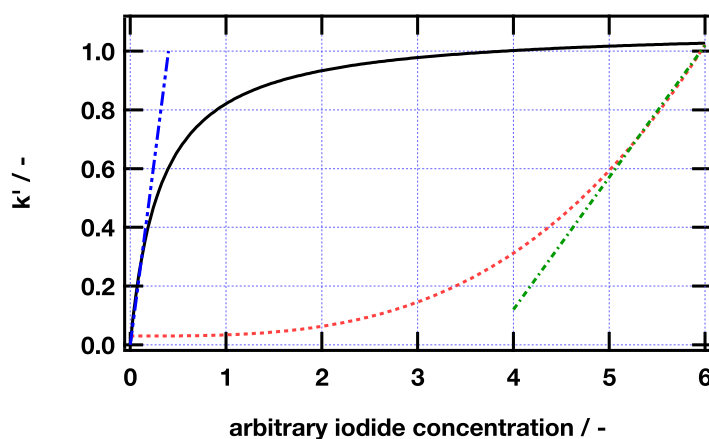


Figure 4.12: Schematic representation of the different dynamics cases; attractive mechanism (—), repulsive mechanism (···), slope of the  $k''_{max}$  for the repulsive case (— · —), slope of the  $k''_{max}$  for the associative case (— · · —).

For the four organic dyes, no Langmuir-type behaviour is reported. Therefore and contrary to the ruthenium based dye N820, no favorable adsorption site is found. In addition and because of the donor-acceptor structure of these dyes, there is no reason for the consideration of the formation of iodide-iodide pairs on the titania surface, because the oxidized center lies on the other side of the molecule.

With ruthenium dyes, several publications report an association between the dye and the iodide anion as reviewed in the introduction, especially onto

the isothiocyanate ligands, according to quantum chemical calculations.<sup>13</sup>

Table 4.3: Second order rate constants summary.

Dye	$k'' / \text{M}^{-1} \cdot \text{s}^{-1}$	Comments
N820	$1.8 \cdot 10^5$	$[\text{I}^-] \leq 0.5 \text{ M}$
Z907Na	$1 \cdot 10^5$	$[\text{I}^-] \geq 1.5 \text{ M}$
C201	$1.73 \cdot 10^6$	whole range of $[\text{I}^-]$
C203	$7.4 \cdot 10^5$	$[\text{I}^-] \geq 4 \text{ M}$
C204	$1.2 \cdot 10^6$	$[\text{I}^-] \geq 4 \text{ M}$
C205	$1.6 \cdot 10^5$	$[\text{I}^-] \geq 5.5 \text{ M}$

A look at the order of magnitude of the second order rate constants reported (summarized in table 4.3) reveals interesting differences.

At first, and except for C205 dye which seems to encounter steric issues, the second order rate constant reported for the organic dyes series are larger by approximately one order of magnitude than the constants reported for the two ruthenium dyes.

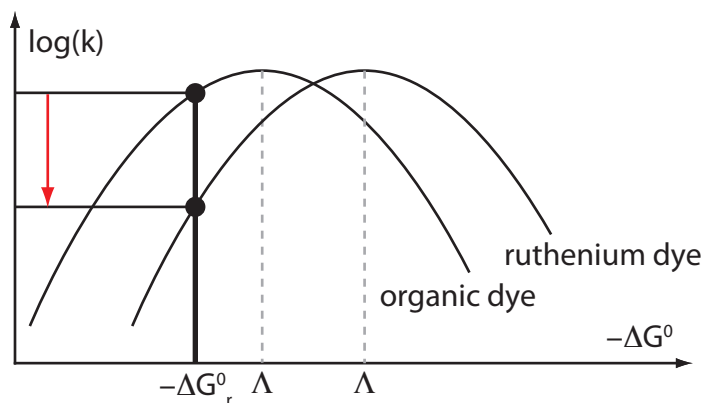


Figure 4.13: Schematic driving force dependance of  $k$  according to the Marcus classical theory. In the normal region, an increase in the reorganization energy results in a decrease of the rate constant.

This could be explained by the thermodynamics of the electron transfer. The regeneration reaction, with a small driving force, lies in the Marcus



normal region. The difference in driving force between the ruthenium and organic dyes,  $\Delta(-\Delta G_r^0)$ , is small. For N3 dye which has a structure close to N820, the oxidation potential in solution is +1.10 V/SHE.<sup>28</sup> For C204 it is +1.00 V/SHE.<sup>29</sup> This 100 mV difference, with an increased driving force for the ruthenium compounds, is incompatible to the observed dynamics and is therefore not a good explanation.

Considering a similar  $\Delta G^0$  for the different compounds, a larger reorganization energy in the ruthenium dyes could explain the difference observed in dynamics. This is illustrated in figure 4.13.

For the purpose of designing new dyes to be used with iodide electrolytes, the insertion of an easily accessible site to interact with iodide, directly onto the dye might be a good strategy, in addition to the D- $\pi$ -A design that enhances electron injection upon light absorption.

## 4.5 Acknowledgments

I warmly thank Julien Andres, Arianna Marchioro and Loïc Roch. They have all contributed to the results presented within this chapter during their respective semester projects and internship in the photochemical dynamics group.

---

## 4.6 References

1. Boschloo, G.; Hagfeldt, A. *Accounts Chem Res* **2009**, *42*, 1819–1826.
2. Pelet, S.; Moser, J. E.; Grätzel, M. *J. Phys. Chem. B* **2000**, *104*, 1791–1795.
3. Ardo, S.; Meyer, G. J. *Chem. Soc. Rev.* **2009**, *38*, 115–164.
4. Vlachopoulos, N.; Liska, P.; Augustynski, J.; Grätzel, M. *J. Am. Chem. Soc.* **1988**, *110*, 1216–1220.
5. Gardner, J. M.; Abrahamsson, M.; Farnum, B. H.; Meyer, G. J. *J. Am. Chem. Soc.* **2009**, *131*, 16206–16214.
6. O'Regan, B. C.; Durrant, J. R. *Accounts Chem Res* **2009**, *42*, 1799–1808.
7. Clark, C.; Marton, A.; Meyer, G. J. *Inorg. Chem.* **2005**, *44*, 3383–3385.
8. Agrell, H.; Lindgren, J.; Hagfeldt, A. *J. Photoch. Photobio. A* **2004**, *164*, 23–27.
9. Clifford, J. N.; Palomares, E.; Nazeeruddin, M. K.; Grätzel, M.; Durrant, J. R. *J. Phys. Chem. C* **2007**, *111*, 6561–6567.
10. Fitzmaurice, D.; Frei, H. *Langmuir* **1991**, *7*, 1129–1137.
11. O'Regan, B. C.; Lopez-Duarte, I.; Martinez-Diaz, M. V.; Forneli, A.; Albero, J.; Morandeira, A.; Palomares, E.; Torres, T.; Durrant, J. R. *J. Am. Chem. Soc.* **2008**, *130*, 2906–2907.
12. Greijer, H.; Lindgren, J.; Hagfeldt, A. *J. Phys. Chem. B* **2001**, *105*, 6314–6320.
13. Privalov, T.; Boschloo, G.; Hagfeldt, A.; Svensson, P. H.; Kloo, L. *J Phys Chem C* **2009**, *113*, 783–790.
14. Schiffmann, F.; VandeVondele, J.; Hutter, J.; Urakawa, A.; Wirz, R.; Baiker, A. *P Natl Acad Sci Usa* **2010**, *107*, 4830–4833.
15. Zhang, Z.; Ito, S.; Moser, J. E.; Zakeeruddin, S.; Grätzel, M. *ChemPhysChem* **2009**, *10*, 1834–1838.
16. Montanari, I.; Nelson, J.; Durrant, J. R. *J. Phys. Chem. B* **2002**, *106*, 12203–12210.

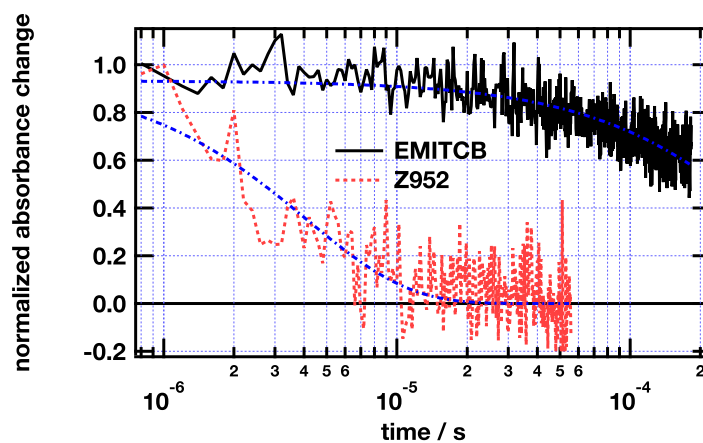
- 
17. Saragi, T. P. I.; Spehr, T.; Siebert, A.; Fuhrmann-Lieker, T.; Salbeck, J. *Chem. Rev.* **2007**, *107*, 1011–1065.
  18. Haque, S. A.; Tachibana, Y.; Willis, R. L.; Moser, J. E.; Grätzel, M.; Klug, D. R.; Durrant, J. R. *J. Phys. Chem. B* **2000**, *104*, 538–547.
  19. Rothenberger, G.; Moser, J. E.; Grätzel, M.; Serpone, N.; Sharma, D. *J. Am. Chem. Soc.* **1985**, *107*, 8054–8059.
  20. Snaith, H. J.; Karthikeyan, C. S.; Petrozza, A.; Teuscher, J.; Moser, J. E.; Nazeeruddin, M. K.; Thelakkat, M.; Grätzel, M. *J. Phys. Chem. C* **2008**, *112*, 7562–7566.
  21. Moser, J. E.; Noukakis, D.; Bach, U.; Tachibana, Y.; Klug, D. R.; Durrant, J. R.; Humphry-Baker, R.; Grätzel, M. *J. Phys. Chem. B* **1998**, *102*, 3649–3650.
  22. Wang, P.; Zakeeruddin, S.; Moser, J. E.; Nazeeruddin, M. K.; Sekiguchi, T.; Grätzel, M. *Nat. Mater.* **2003**, *2*, 402–407.
  23. Mori, S. N.; Kubo, W.; Kanzaki, T.; Masaki, N.; Wada, Y.; Yanagida, S. *J. Phys. Chem. C* **2007**, *111*, 3522–3527.
  24. Heimer, T.; Heilweil, E.; Bignozzi, C.; Meyer, G. J. *J. Phys. Chem. A* **2000**, *104*, 4256–4262.
  25. Moser, J.-E. *Dye Sensitized Solar Cells, Chapter 11: Dynamics of interfacial and surface electron transfer processes*, Kalyanasundaran K., Ed., EPFL Press, **2010**.
  26. Kroeze, J. E.; Hirata, N.; Koops, S. E.; Nazeeruddin, M. K.; Schmidt-Mende, L.; Grätzel, M.; Durrant, J. R. *J. Am. Chem. Soc.* **2006**, *128*, 16376–16383.
  27. Snaith, H. J.; Humphry-Baker, R.; Chen, P.; Cesar, I.; Zakeeruddin, S.; Grätzel, M. *Nanotechnology* **2008**, *19*, 424003.
  28. Nazeeruddin, M. K.; Kay, A.; Rodicio, I.; Humphry-Baker, R.; Muller, E.; Liska, P.; Vlachopoulos, N.; Grätzel, M. *J. Am. Chem. Soc.* **1993**, *115*, 6382–6390.
  29. Xu, M.; Wenger, S.; Bala, H.; Shi, D.; Li, R.; Zhou, Y.; Zakeeruddin, S.; Grätzel, M.; Wang, P. *J. Phys. Chem. C* **2009**, *113*, 2966–2973.



## Chapter 5

# Dynamics of an organic D- $\pi$ -A dye sensitizing TiO<sub>2</sub>

### Graphical abstract



C204 dye cation lifetime and its interception by an iodide redox mediator

## 5.1 Introduction

Benchmark dye-sensitized solar cells (DSSCs) are based on ruthenium complexes, derived from the well known N3, N719 or Z907 compounds, which sensitize a titanium dioxide ( $\text{TiO}_2$ ) mesoporous thin film.<sup>1-3</sup> With these molecules, maximum efficiencies of more than 11% were achieved.<sup>4</sup> Such complexes have broad metal-to-ligand charge transfer (MLCT) absorption bands, covering a wide part of the solar spectrum over the visible domain. They also have chemically stable excited and oxidized species. The latter have appropriate redox energy levels for both the electron injection into  $\text{TiO}_2$  enabling efficient electron transfer into the semiconductor, and for the regeneration of their ground state by the electrolyte's iodide, efficiently intercepting dye cations.

A major drawback of these metal complexes is their relatively low molar extinction coefficients ( $\epsilon$ ) compared to organic molecules. In order to overcome this limitation, use of all-organic molecules has to be considered.

Most of the organic molecules that have been used for the study of electron injection into a semiconductor present higher  $\epsilon$  value than the usual ruthenium-based dyes. However they also have a narrower absorption spectrum or an absorption spectrum located in the ultraviolet (UV) or blue end of the visible spectrum, like perylenes, cyanines, coumarins or indolines.<sup>5-7</sup> Nevertheless, they exhibit efficient sensitization of titania, with ultrafast electron injection rates comparable to what had been observed with ruthenium-based systems, typically leading to electron injection within a timescale of 100 fs.<sup>8</sup> In addition and due to the absence of heavy atoms in their structure, organic dyes have a weak intersystem crossing. Therefore the injecting excited states are of major singlet character.

Another issue is their potential lack of stability, inducing rapid bleaching of samples upon light soaking.

Therefore, these drawbacks present a challenge for solar energy conversion, especially in terms of light harvesting at the red-end of the solar spectrum which is crucial for obtaining good conversion yields. On the other

hand, there are major advantages using all-organic compounds. Indeed, there is no need for using precious metals such as ruthenium, which could be toxic and of limited availability. In addition, smart molecular design can be widely applied in order to attain the desired electrochemical and optical properties.

### 5.1.1 Organic D- $\pi$ -A dyes

A whole class of molecules has been designed in order to meet these requirements. They are donor,  $\pi$ -conjugated bridge, acceptor (D- $\pi$ -A) systems composed of a joint structure. Figure 5.1 shows the structure of the C204 dye used in this study<sup>i</sup>. An electron donor moiety, based on a dimethylfluorene triarylamine derivative, is present at one end of the molecule. This unit carries the dye's HOMO<sup>ii</sup> and therefore will be a good acceptor for the hole created upon oxidation. The electron rich  $\pi$ -bridge is composed of a thiophene derivative that is 3,4-ethylenedioxythiophene (EDOT) in the present case. The anchoring carboxylic group is accompanied by a cyano part, being a good electron acceptor. This cyanoacrylic unit will both locate the LUMO<sup>iii</sup> close to the titania surface and allows for an efficient anchoring onto the semiconductor surface.<sup>9</sup>

This design helps, upon light irradiation, to locate the electron close to the semiconductor, thus permitting efficient electron injection into the latter. These molecules also have redox energy levels that allow for efficient sensitization of TiO<sub>2</sub>, as well as the reduction of their cations by an electrolyte containing iodide.

### 5.1.2 Electron injection into TiO<sub>2</sub>

The primary charge separation step in DSSCs is the electron injection from the excited sensitizer into the semiconductor conduction band upon

---

<sup>i</sup>3-{5'-[N,N-bis(9,9-dimethylfluorene-2-yl)phenyl]-3,4-ethylenedioxythiophene-5-yl}-2-cyanoacrylic acid

<sup>ii</sup>Highest occupied molecular orbital

<sup>iii</sup>Lowest unoccupied molecular orbital

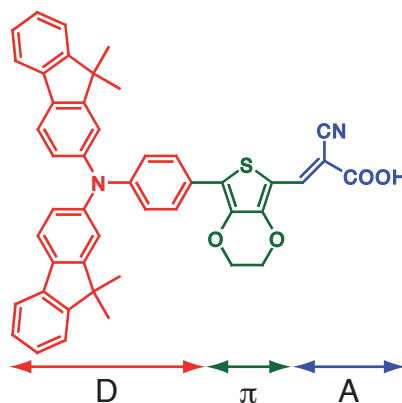


Figure 5.1: C204 dye structure. Note the triarylamine donor moiety, the electron rich  $\pi$ -bridge (EDOT moiety) and the cyanoacrylate anchoring group.

light absorption. In the case of ruthenium complexes, this reaction is well documented, revealing mainly sub-picosecond dynamics.<sup>10</sup>

However, the electron transfer process is not well known for this D- $\pi$ -A class of dye, having a cyanoacrylate unit as the anchoring group. Contrary to alizarin, for which the strong anchoring to  $\text{Ti}^{\text{IV}}$  atoms is achieved via chelating by two oxygen atoms,<sup>11</sup> here only one adsorption site is available on the dye structure, i.e. the carboxylic group. This implies a weaker adsorption with some degrees of freedom on the surface, and no control on the dye adsorption angle.

Only a few experiments have been done to resolve electron injection dynamics of this kind of D- $\pi$ -A dye. Kitamura *et al.* reported ultrafast electron injection by monitoring the free electrons in the conduction band in the NIR ( $5\text{ }\mu\text{m}$ ) region<sup>12</sup> and, more recently, Myllyperkiö *et al.* reported ultrafast measurements in the visible.<sup>13</sup> This latter study led to the finding of time components assigned to electron transfer up to 300 fs, especially when the donor moiety of the sensitizer is a tertiary amine, as it can be found on the C204 dye.

Electron injection dynamics heterogeneities have often been reported for inorganic dyes. They have been attributed to injection from hot



or thermalized states, from  $^3\text{MLCT}$  states,<sup>14–17</sup> from different types of adsorption sites, or from dye molecules aggregated on the surface of the semiconductor.<sup>18,19</sup> In all-organic dye-sensitized semiconductors, the intersystem crossing is weak and therefore injection from lower triplet states should not be relevant anymore. Nevertheless, dye aggregation might be a problem of major importance as many organic dye compounds are known to aggregate, such as cyanines.<sup>20,21</sup>

To prevent inhomogeneous coverage of the surface,  $3\alpha,7\alpha$ -dihydroxy- $5\beta$ -cholic acid (cheno) is often added to the dye solution as a co-adsorbant.<sup>22</sup> Reported dynamics for dyes similar to the one studied here present the same kind of heterogeneities reported for other ruthenium-based sensitizers.<sup>13</sup>

### 5.1.3 C204 state of the art

The dye studied herein, C204, presents good photovoltaic performances with an efficiency of 7.31 % in a solvent-free electrolyte as well as an excellent stability, akin to its parent dye C205.<sup>9</sup> Contrary to ruthenium dyes, which have been deeply investigated, these D- $\pi$ -A dyes photophysical properties, as well as their sensitization dynamics remain poorly documented.

C204 electron injection into  $\text{TiO}_2$  has been widely monitored and compared to redox inactive alumina samples. The dye cation recombination processes as well as its interception by iodide leading to the regeneration of the dye ground state are also reported for a complete time mapping of the photoinduced reactions.

## 5.2 Experimental part

### 5.2.1 Chemicals

#### Dye

The dye is described in the previous section 5.1.1. Its structure and especially the dimethylfluorenes might also help preventing dye aggregation on the

surface by prohibiting the  $\pi$ -stacking of the aromatic rings. This is due to their propeller shape. The resulting D- $\pi$ -A system is supposed to present an intramolecular charge transfer (ICT) transition at the red end of its spectrum.<sup>23,24</sup> Its synthesis has been described elsewhere.<sup>9</sup>

### Titanium dioxide

The electrode consists of a mesoporous layer of anatase TiO<sub>2</sub>, which is deposited onto a glass substrate by doctor blading<sup>1</sup> a paste containing 16 nm diameter TiO<sub>2</sub> particles (14 wt%), a polymer (ethyl cellulose) and diverse additives. Upon calcination at 470 °C for 25 minutes, the resulting layer has a controlled thickness of 4.8 to 9.6  $\mu$ m, with a porosity of 0.625.

### Alumina

Alumina (Al<sub>2</sub>O<sub>3</sub>) layers of 4 to 8  $\mu$ m are deposited on a glass substrate in a manner similar to TiO<sub>2</sub> layers. The paste used for the doctor blading procedure is composed of 6.4 nm Al<sub>2</sub>O<sub>3</sub> nanoparticles (18 wt%), a polymer (hydroxypropyl cellulose 100000) and diverse additives. Upon deposition, the semiconductor layer is sintered at 470 °C for 25 minutes, thus producing mesoporous layers with a porosity of 0.72.

### 5.2.2 Samples

TiO<sub>2</sub> and Al<sub>2</sub>O<sub>3</sub> films of about 1 cm<sup>2</sup> are dipped into a dye solution of no more than  $5 \cdot 10^{-4}$  M in acetonitrile-tert-butanol (1:1, v/v) for about 12 hours (typically overnight). This results in efficient coverage of the semiconductor by a monolayer of the dye. During analysis, samples are immersed into a redox inactive ionic liquid, 1-ethyl-3-methylimidazolium bis(trifluoromethanesulfonyl)imide (EMITFSI) or 3-methoxypropionitrile (MPN) or the desired redox electrolyte and then covered with a thin glass plate.

## 5.3 Results and discussion

### 5.3.1 Absorption spectrum of the dye

The absorption spectrum of the dye in an ethanolic solution presents two major bands in the UV-visible spectral domain as shown on figure 5.2. The first one has a maximum at 364 nm and the second at 455 nm. The band in the UV corresponds to a  $\pi$ - $\pi^*$  transition of the conjugated molecule, whereas the band centered in the blue can be assigned to an intramolecular charge transfer state (ICT) between the triarylamine electron donating moiety and the cyanoacrylate acceptor unit.<sup>24–26</sup> Upon adding some acid to the dye solution, the ICT band is red-shifted.

Upon adsorption onto an oxide,  $\text{TiO}_2$  or  $\text{Al}_2\text{O}_3$ , the ICT band maximum is not significantly affected. The observation of this band indicates that the electron density on the cyanoacrylate after the substitution of protons with  $\text{Ti}^{\text{IV}}$  or  $\text{Al}^{\text{III}}$  surface atoms is similar. Nevertheless, a broadening is observed on the red side of the transition, promoting an absorption shoulder at lower energies, thus enhancing light harvesting beyond 550 nm.

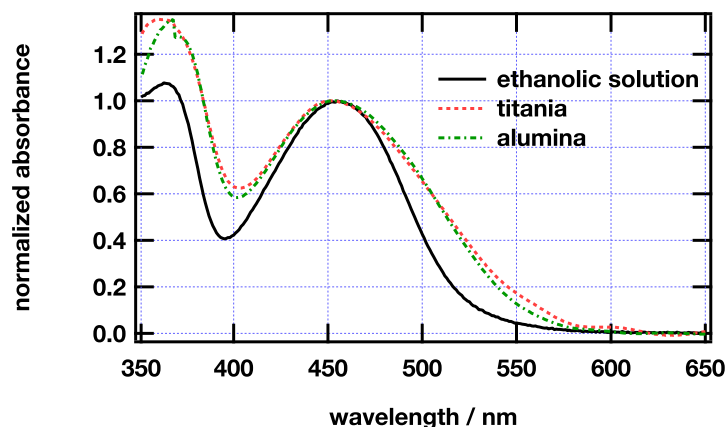


Figure 5.2: Normalized UV-Vis absorption spectra of C204 in ethanolic solution (—), C204/ $\text{TiO}_2$  (· · ·) and C204/ $\text{Al}_2\text{O}_3$  (- · -).

### 5.3.2 Emission spectroscopy

Emission spectroscopy reveals a spectrum with a maximum at 600 nm in ethanolic solution. This maximum is shifted to 640 nm upon adsorption to either of the semiconductors.

The  $E_{0-0}$  transition of the dye is estimated by the cross point of emission and excitation spectra at a value of 2.46 eV (505 nm). The emission quantum yields in solution and onto both oxydes are measured at two excitation wavelengths (450 and 550 nm). This will highlight the difference between the spectra of the adsorbed and free dye. Results are summarized in table 5.1 and show that C204 efficiently sensitizes  $\text{TiO}_2$ . On this oxide, the emission is almost quantitatively quenched by electron injection. In the case of  $\text{Al}_2\text{O}_3$ , a decrease in yield confirms the decrease of degrees of freedom of the dye upon adsorption. Nevertheless, it is found that the sensitization is inefficient. No major differences are observed upon red-wing excitation, excepted in solution, where the dye only poorly absorbs at 550 nm and, therefore, does not emit.

The emission lifetimes are measured by time correlated single photon counting (TCSPC). However, the resolution of the setup used does not allow for resolving numerically the changes in lifetime. They are all sub-200 ps, a time close to the time response of the detector. The excited state lifetime will be measured by transient absorbance spectroscopy with an adequate time resolution in section 5.3.5. A qualitative analysis shows that the signal amplitude at time zero is greatly decreased for the titania sample, confirming efficient static quenching by electron injection. The timescale reported corresponds to fluorescence process and therefore to an excited state singlet character.

The Stokes shift is large for this compound, around  $5215\text{ cm}^{-1}$ . This value is consistent with a fluorescence arising from an ICT state as well as with a potential conformational change in the excited state. The latter might be located over the double bond of the cyanoacrylate moiety.

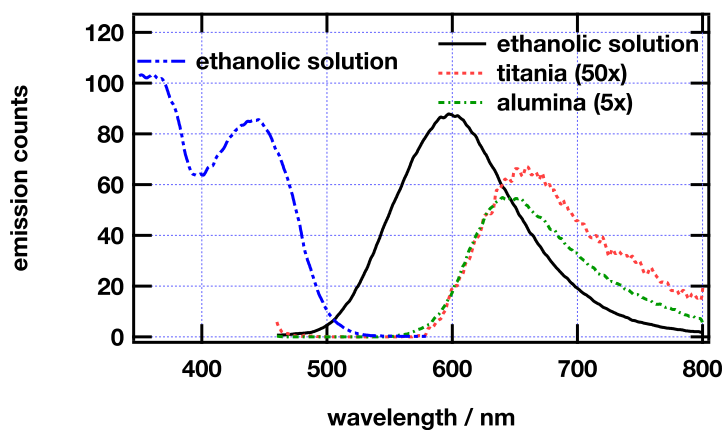


Figure 5.3: Excitation spectra of C204 in ethanolic solution,  $\lambda_{obs} = 600$  nm (---). Emission spectra at  $\lambda_{ex} = 445$  nm, C204 in ethanolic solution (—), C204/TiO<sub>2</sub> (· · ·) and C204/Al<sub>2</sub>O<sub>3</sub> (— · —).

Table 5.1: Emission quantum yield and lifetime values of the dye C204.

	Emission yield ( $\lambda_{ex} = 450$ nm)	Emission yield ( $\lambda_{ex} = 550$ nm)	$\tau$ ( $\lambda_{ex} = 400$ nm)
EtOH	0.0624	0	<200 ps
Al <sub>2</sub> O <sub>3</sub>	0.0142	0.011	<200 ps
TiO <sub>2</sub>	0.0006	0.0006	<200 ps

### 5.3.3 Photoinduced absorption spectroscopy

Photoinduced absorption spectroscopy (PIA) is a powerful technique for mapping the spectrum of transient species having a sufficiently long lifetime.<sup>27</sup> In the study of sensitized semiconductors, it is particularly convenient to locate the spectral signature of the dye cation formed upon electron injection. To this end, PIA spectra have been recorded on both alumina and titania samples upon 470 nm excitation.

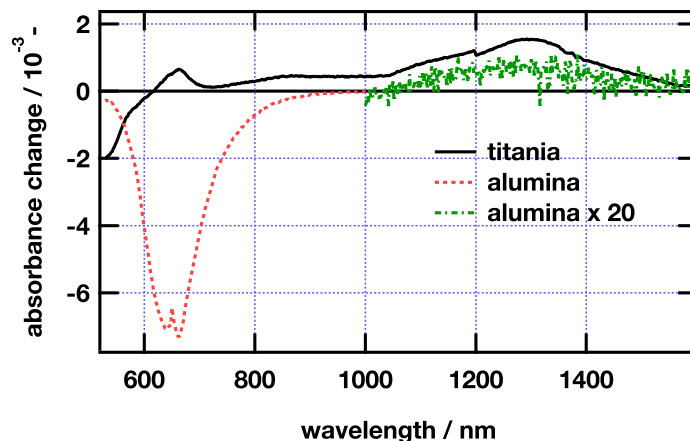


Figure 5.4: PIA spectrum of C204/TiO<sub>2</sub> 4.8  $\mu\text{m}$  (—), C204/Al<sub>2</sub>O<sub>3</sub> 5  $\mu\text{m}$  (···), C204/Al<sub>2</sub>O<sub>3</sub> expanded 20x (---),  $\lambda_{\text{ex}}$  = 470 nm at 9 Hz in air.

The measurements on the alumina sample reveal a strong negative signal with an intensity maximum at 640 nm, figure 5.4, which is the result of the emission of the dye. In addition, a very weak positive transient absorbance change is observed in the near-infrared. Because this positive change in absorbance is weak compared to the emission signal, the graph is expanded twenty times for better reading. This absorbance is attributed to the spectral signature of the intramolecular charge transfer state, particularly to the hole located on the triarylamine moiety of the dye.<sup>28</sup>

On TiO<sub>2</sub>, emission is quantitatively quenched, in accordance with the quantum yield reported above. The species observed is thus the dye cation. It ensures that the two major absorption bands, centered at 660 nm and

around 1300 nm, are attributed to the oxidized sensitizer. Again, the band at lower energies is the signature of the hole located on the triarylamine, which is here characterized by an enhanced intensity with respect to dye adsorbed onto alumina, confirming the existence of a long-lived charge separated state. This is yet another proof of the efficient sensitization of  $\text{TiO}_2$  with C204.

### 5.3.4 Nanosecond transient absorbance

Laser flash photolysis has been performed to time resolve the spectra obtained with PIA. At the same time, monitoring the interception of the dye cation by the redox mediator, iodide, has been achieved.

The transient spectra of the dye adsorbed onto  $\text{TiO}_2$  is reported on figure 5.5. The sample used has an absorbance of about 0.75 at the excitation wavelength of 530 nm. Over the spectral range that overlaps with the PIA spectrum, the shape of the absorbance spectrum is similar, with its maximum at about 650 nm and an isosbestic point at 600 nm. Such a well resolved isosbestic point confirms the observation of only two species (in this case S and  $\text{S}^+$ ) during the reaction. The blue side of the transient represents the bleaching of the dye ground state.

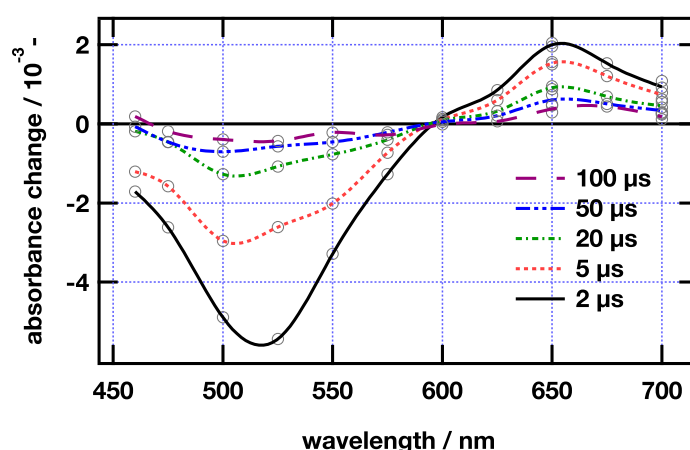


Figure 5.5: Nanosecond transient spectra of C204/ $\text{TiO}_2$  at 2 (—), 5 (· · ·), 20 (---), 50 (- · -) and 100  $\mu\text{s}$  (- - -) after the excitation pulse,  $\lambda_{\text{ex}} = 530$  nm in MPN.

This explains the choice of 650 nm wavelength for monitoring the dye cation in the visible.

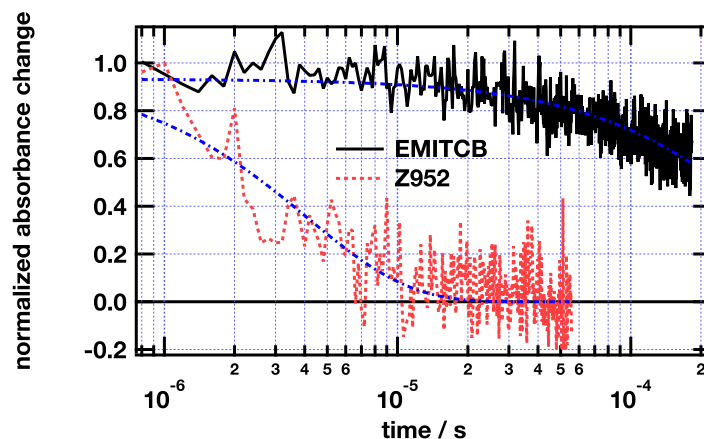


Figure 5.6: Nanosecond transient of C204/TiO<sub>2</sub> in EMITCB (—), Z952 electrolyte (· · ·) and monoexponential fits (— · —),  $\lambda_{\text{ex}} = 530$  nm,  $\lambda_{\text{obs}} = 650$  nm.

At this wavelength, the absorbance transient is followed under two distinct conditions. At first in EMITCB for monitoring the dye cation lifetime in a redox inert environment. Then, the addition of Z952 electrolyte<sup>iv</sup> to the sample allows to monitor the reaction of interception of the dye cation by the iodide redox mediator.

Figure 5.6 shows a decrease of two orders of magnitude of the lifetime of the dye cation upon addition of the electrolyte, confirming efficient interception of the oxidized dye by iodide.

Without electrolyte, the recombination reaction (reaction 5.1) has a monoexponential time constant  $\tau = 383$   $\mu$ s, which is shortened down to  $\tau = 4$   $\mu$ s upon addition of the electrolyte (reaction 5.2).



<sup>iv</sup>1,3-dimethylimidazolium iodide / 1-ethyl-3-methylimidazolium iodide / 1-ethyl-3-methylimidazolium tetracyanoborate / iodine / N-butylbenzimidazole / guanidinium thiocyanate (DMII / EMII / EMITCB / I<sub>2</sub> / NBB / GNCS, molar ratio 12 / 12 / 16 / 1.67 / 3.33 / 0.67)





The regeneration yield ( $\eta_{reg}$ ) is then calculated using equation 4.17, reported here (5.3).<sup>29</sup>  $k'_r = 1/\tau_r$  is the pseudo-first order rate constant of regeneration, i.e. in the presence of redox species  $I^-$  (equation 5.2), while  $k_b = 1/\tau_b$  is the rate constant in pure EMITCB and therefore represents the back electron transfer reaction (equation 5.1).

$$\eta_{reg} = \frac{k'_r}{k'_r + k_b} \quad (5.3)$$

The calculated yield is around  $\eta_{reg} = 99\%$ . The interception of the dye cation by iodide is efficient, thus, C204 is an interesting candidate for the dye-sensitized solar cell.

### 5.3.5 Femtosecond transient absorbance; two colors pump-probe

Pump-probe spectroscopy has been performed in order to monitor the ICT state lifetime. The pump beam is set at 530 nm and the probe beam in the NIR at 1100 nm. This last wavelength allows the hole, located on the triarylamine moiety of the dye, to be directly monitored. The measured transient contains also a small contribution from the electrons injected into  $TiO_2$ , but these will have similar dynamics than the hole. The sample is immersed in 3-methoxypropionitrile (MPN).

In ethanolic solution, the ICT state has a monoexponential lifetime of 61 ps, as shown on figure 5.7. One can observe a slow rise subsequent to the excitation pulse ultrafast response. It has a  $\tau = 1.1$  ps time constant, with a small amplitude with respect to the full range signal. Its origin remains unknown but might arise from the chirp induced by the quartz cell used<sup>v</sup>. This lifetime is shorter than the resolution of the TCSPC measurement, which is why it is not possible to compare it quantitatively.

---

<sup>v</sup>Hellma, 1mm, QS 100

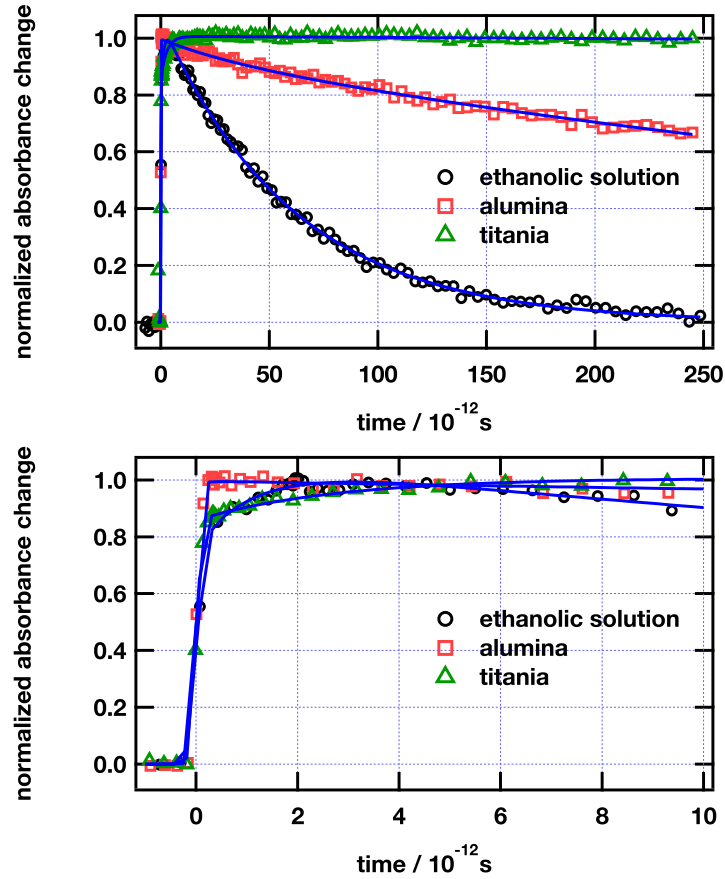


Figure 5.7: Top: Femtosecond transient absorbance,  $\lambda_{obs} = 1100$  nm,  $\lambda_{ex} = 530$  nm, C204 in ethanolic solution ( $\circ$ ), C204/ $\text{Al}_2\text{O}_3$  in MPN ( $\square$ ) and C204/ $\text{TiO}_2$  in MPN, solid lines are fits results for a convolution of a gaussian and two exponentials. Ethanolic solution:  $\sigma = 132$  fs,  $\tau_1 = 1.1$  ps (rise),  $\tau_2 = 61$  ps (decay). C204/ $\text{Al}_2\text{O}_3$ :  $\sigma = 88$  fs,  $\tau_1 = 37$  ps (decay),  $\tau_2 = 711$  ps (decay). C204/ $\text{TiO}_2$ :  $\sigma = 93$  fs,  $\tau_1 = 2.7$  ps (rise),  $\tau_2 = 2400$  ps (decay).  $\sigma$  and  $\tau_i$  are the parameters of equation 2.10. Bottom: zoom of the first ten picoseconds.

Upon adsorption onto alumina films, this lifetime is increased up to about 700 ps. Nevertheless, it contains a first faster decrease component of  $\tau = 37$  ps which remains unidentified. This could globally be interpreted as an increase in the dipole moment of the excited molecule induced by the adsorption. It stabilizes the electron close to the alumina and slows down the ground state regeneration dynamics. Additionally, alumina could have accessible trap states capable of accepting the excited electron, without engendering formal electron injection into the semiconductor. Both of these effects might be responsible for a global stabilization of the ICT state resulting in the slower dynamics observed.

On  $\text{TiO}_2$ , the story is different. During the time window studied, the transient is stable, without any decrease even beyond the 61 ps lifetime of the excited state. The signal can thus be attributed to the oxidized dye. This indicates efficient delocalization of the electron into the semiconductor, inducing a charge-separated state and not an ICT state. At short timescale, a second fast rise component is observed following the excitation pulse, with time constant of 2.7 ps. This might be attributed to slower components of the electron injection process, induced by the presence of aggregated molecules that would have a weaker coupling to the surface. Alternatively and similarly to the liquid sample, it might arise from solvation dynamics.

### 5.3.6 Femtosecond transient absorbance; pump white-light-continuum-probe

As showed on PIA spectra in figure 5.4, the dye cation also exhibit a positive absorbance in the visible. In this experiment, collecting simultaneously transients from 500 up to 700 nm allows to simultaneously monitor the ground state bleaching below 600 nm, and the oxidized sensitizer above 600 nm.

C204-sensitized  $\text{Al}_2\text{O}_3$  and  $\text{TiO}_2$  films were excited with green light ( $\lambda_{\text{ex}} = 530$  nm) and probed with a white-light pulse. Samples are immersed in MPN for this measurement.

On alumina films, the transient spectrum is characterized by a weak negative band representing the bleaching of the ground state (figure 5.8). This band overlaps with the positive band arising from the excited state absorbance and is, for this reason, difficult to monitor. Formation of the excited state is followed by an ultrafast relaxation within the first 100 fs which is represented by a decreasing positive absorbance band, centered at  $\sim 610$  nm. This ultrafast process is then followed by a long lived component, represented by the positive band at  $\sim 590$  nm. The stimulated emission, usually invoked in order to be able to easily record the electron injection dynamics is unfortunately absent, thus depriving us of an easy way of monitoring the excited state dynamics.

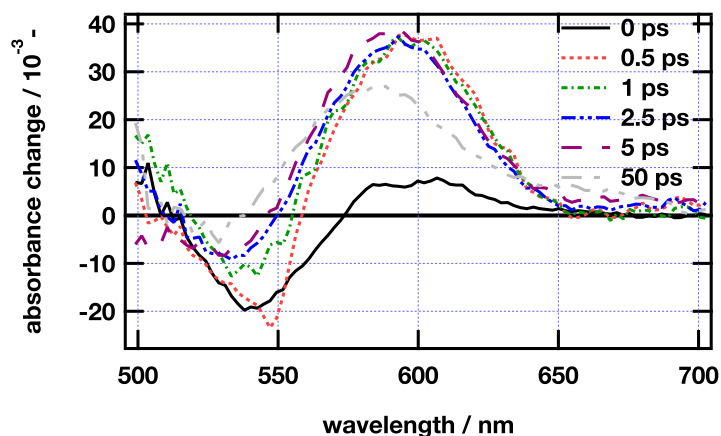


Figure 5.8: Pump-white-light-continuum-probe (WLC-probe) transient spectra of C204/ $\text{Al}_2\text{O}_3$ ,  $\lambda_{\text{ex}} = 530$  nm, wavelength smoothed data.

On  $\text{TiO}_2$ , the spectral shape of the transient spectra are similar at early times. A peak centered at 610 nm arises within the pulse. In contrast, this latter band is then shifted to the red end of the spectrum, up to 650 nm (figure 5.9). This observation is characteristic of the dye cation after electron injection into the semiconductor, as monitored during longer timescale experiments such as PIA or nanosecond flash photolysis. The species observed at 590 nm is not observed in this case, indicating efficient sensitization of the semiconductor by confirming that no excited

state remains within the system, even at the short timescales.

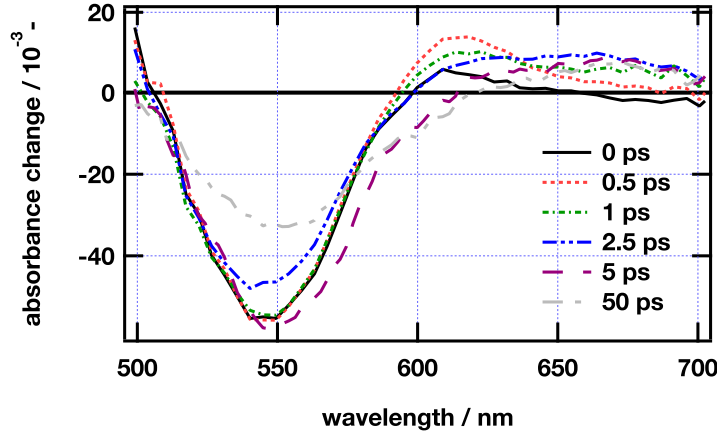


Figure 5.9: Pump-WLC-probe transient spectra of C204/TiO<sub>2</sub>,  $\lambda_{\text{ex}} = 530$  nm, wavelength smoothed data.

An extended analysis of these transients spectra has been performed. As described in section 2.1.7, the data treatment applied to white-light results involves both a time correction to account for the chirp of the probe pulse and a smoothing over the wavelength axis. Figures 5.8 and 5.9 reflect the quality of the data at this stage. Finally, the data are simplified by applying a singular value decomposition (SVD) procedure, which allows for an efficient reduction of the noise level of the data, granting easier global fitting convergence.

At short timescale, typically up to 3 ps, the result of the global fit, both on alumina and titania, should help resolve the electron injection into the semiconductor.

### Ultrafast dynamics on alumina

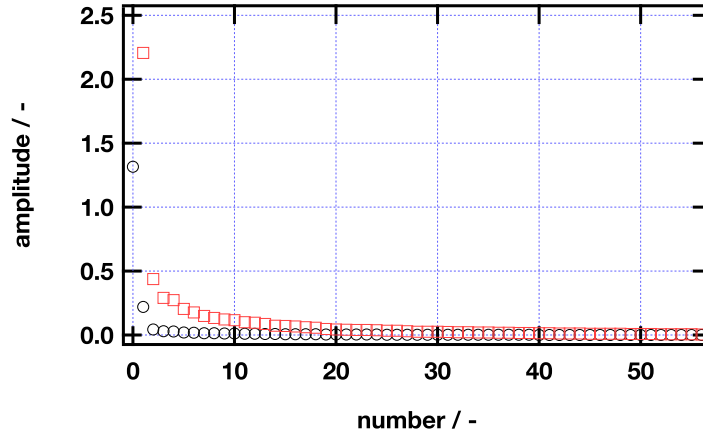
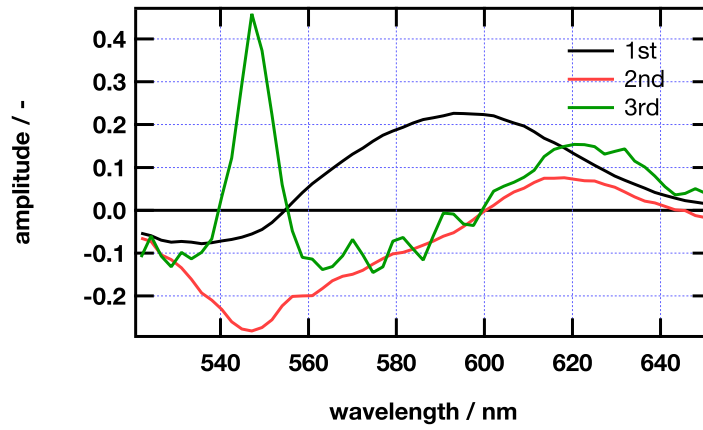
From the SVD results, several observations are made. The first singular value is very intense compared to the others and accounts for more than 70 % of the global amplitude. As explained in chapter 3, this suggests that only one species is monitored. This is in accordance with the experiment in which

only the C204 excited state is expected on alumina samples. Therefore, the first wavelength component of figure 5.10(b) should resemble the spectrum of the dye excited state. It is composed of an isosbestic point centered at 555 nm, the bleaching of the ground state at the higher energies and a positive transient in the red side, centered at 590 nm.

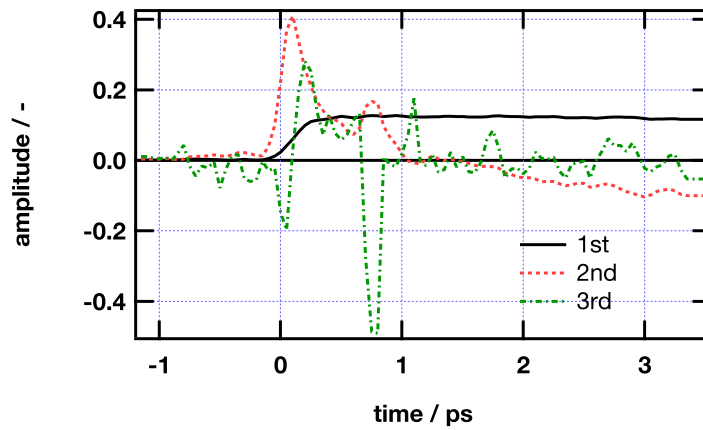
Although the third component seems to contain some spectral information, the third time vector seems to only represent experimental noise. The first two components of the SVD are used to reconstruct the matrix that will serve as the input of the global fitting analysis.

Equation 2.10 is used for the fitting procedure and represents a sum of convolutions between a gaussian instrument response function (IRF) and three exponential functions. The procedure is described in details in section 2.1.7. The time zero parameter ( $\mu$ ) as well as the width of the gaussian function ( $\sigma$ ) are kept close to the values estimated by measuring the IRF by Kerr gating in a glass slide.

On alumina, the global fitting routine needs three exponential components to reproduce the measured dynamics. A first component of 554 fs corresponds to the rise of the 600 nm absorbance peak. In the meantime, a relaxation channel with a typical time constant of  $\tau = 656$  fs decreases the maximum at 610 nm. This behavior could be attributed to a change in the dye conformation within the ICT state for example. This assumption is also supported by the relatively large Stokes shift of  $5215\text{ cm}^{-1}$ , revealed by emission measurements. This conformation change could be located around the double bond of the anchoring moiety which can rotate. The third and last component reported is related to the long lived excited state. Its time constant has been held at 100 ps (the parameter is fixed in the fitting procedure), being out of the range of the measurement. Figure 5.11 presents the Decay Associated Spectra (DAS) related to this three time constants.

(a) Singular values ( $\circ$ ), expanded 10 times ( $\square$ )

(b) Wavelength vectors



(c) Time vectors

Figure 5.10: Singular value decomposition of the femtosecond transient spectrum of C204/ $\text{Al}_2\text{O}_3$  in MPN.

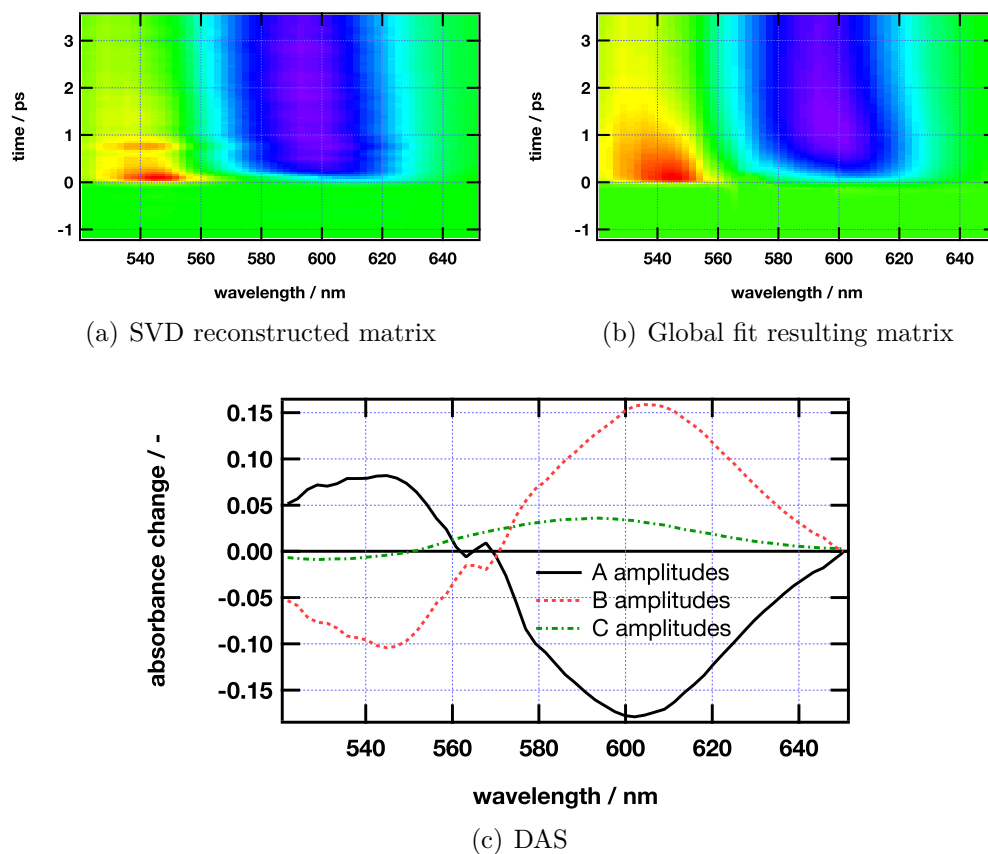


Figure 5.11: Data treatment results. (a) SVD reconstructed matrix with two wavelength and two time components. (b) Global fit resulting matrix, convolution of a gaussian ( $\sigma = 70$  fs) and three exponentials.  $\sigma$  and  $\tau_i$  are the parameters for equation 2.10. (c) Decay associated spectrum of the three time components. A amplitude  $\tau_A = 554$  fs (—), B amplitude  $\tau_B = 656$  fs ( $\cdots$ ), C amplitude  $\tau_C = 1000$  ps (hold) ( $-\cdot-$ ).



### Ultrafast dynamics on titania

The SVD results allow for a first analysis of the data. The first singular value contains most of the information of the transient spectrum. It accounts for more than 70 % of the total signal amplitude. This suggests that only one species is monitored. Therefore, the first wavelength component of figure 5.12(b) can be associated with the dye cation spectrum, as it is the product expected from electron injection into titania. It exhibits an isosbestic point around 600 nm, in accordance with the nanosecond time resolved results. The bleaching of the ground state can be observed on the green side and a small positive transient is flat up to 700 nm, in accordance with the dye cation absorption.

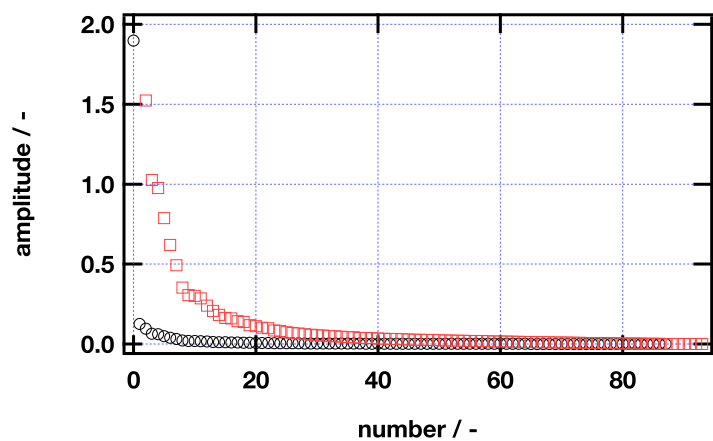
The third time vector does not seem to contain any time dependant data and therefore only the two first components of the SVD will be retained to construct the matrix used in the global fitting analysis.

The global fitting was done using equation 2.10. It needed two exponentials components. The time zero parameter ( $\mu$ ) as well as the width of the gaussian function ( $\sigma$ ) are kept constant at the values estimated by measuring the IRF by Kerr gating in a glass slide.

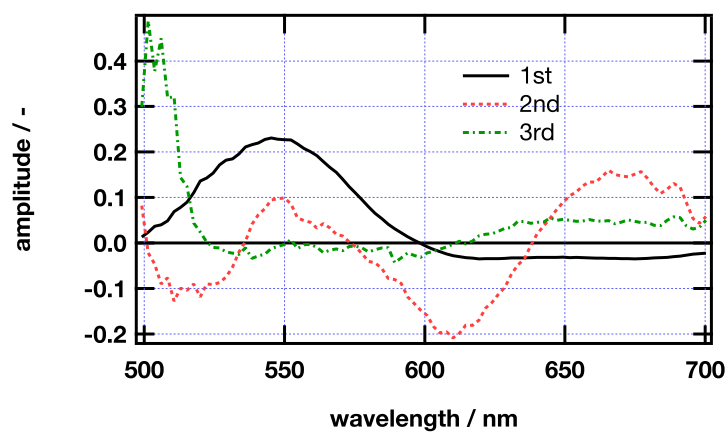
When measuring onto  $\text{TiO}_2$ , only two time components are necessary for reconstructing the recorded dynamics. The fitting procedure reveals the timescale of the electron injection into the semiconductor.

A positive transient absorbance centered at 605 nm corresponds to the early component detected on alumina sample. This positive change vanishes with a time constant of  $\tau = 1.71$  ps. This is correlated with a broader absorption rise in the red end of the recorded spectrum, having a maximum at 660 nm, which corresponds to the absorption spectrum of the dye cation. This band is constant up to the end of the investigated time window and has a time constant of 7 ps (hold). The band centered at 590 nm that is observed for alumina samples is not present for titania which confirms an efficient electron injection into the  $\text{TiO}_2$  conduction band.

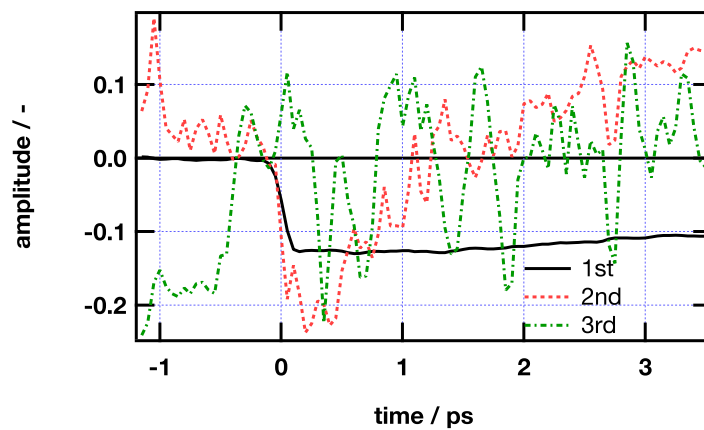
The absorbance band centered at 660 nm also has a component that rises



(a) Singular values (○), expanded 10 times (□)



(b) Wavelength vectors



(c) Time vectors

Figure 5.12: Singular value decomposition of the femtosecond transient spectrum of C204/TiO<sub>2</sub> in MPN.

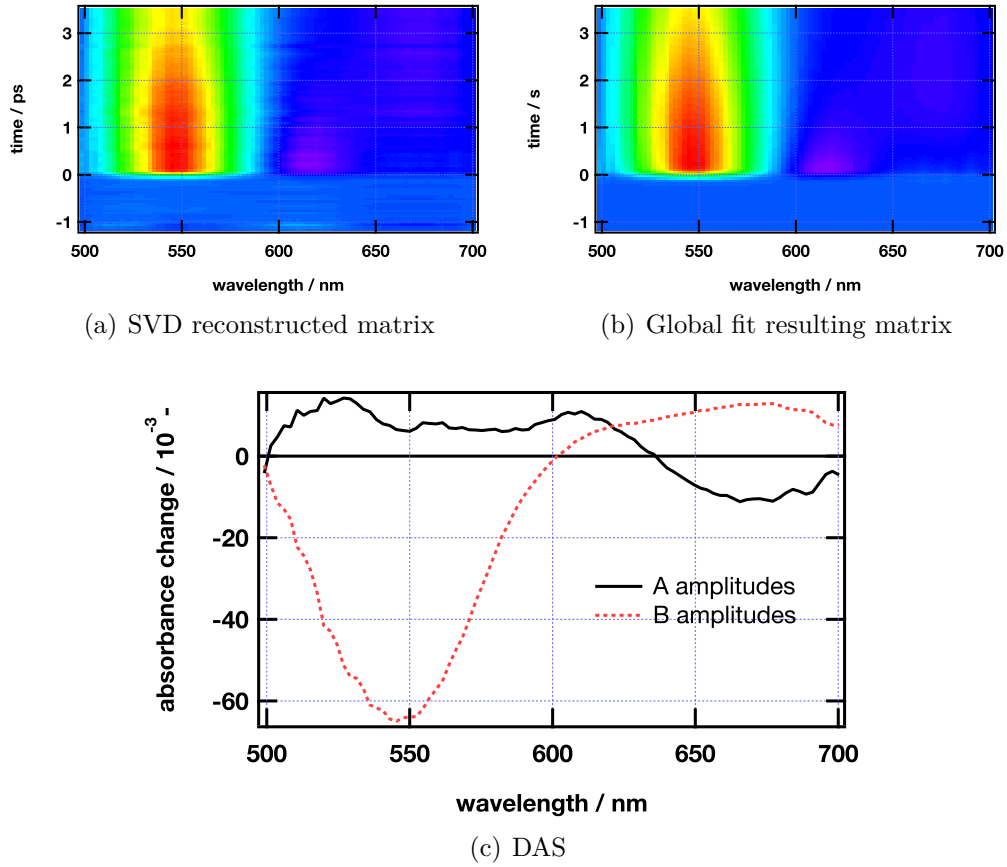


Figure 5.13: Data treatment results. (a) SVD reconstructed matrix with two wavelength and two time components. (b) Global fit resulting matrix, convolution of a gaussian ( $\sigma = 70$  fs) and two exponentials.  $\sigma$  and  $\tau_i$  are the parameters for equation 2.10. (c) Decay associated spectrum of the two time components. A amplitude  $\tau_A = 1.71$  ps (—), B amplitude  $\tau_B = 7$  ps (hold) (···).

within the excitation pulse, i.e.  $< 50$  fs, without being formerly resolved. This indicates an heterogeneity in the electron injection process, which might be due to dye aggregation on the semiconductor surface, inducing an heterogeneous binding of the dye onto the surface. Sample to sample variations in the measured amplitudes of each components, relatively to each other, seem to suggest that the degree of aggregation is varying.

### **Longer measurements on alumina and titania**

In addition, measurements have been carried out on both oxides on timescales up to 100 ps by using a lower time resolution than that presented on figures 5.8 and 5.9. On alumina, the excited species absorption spectrum centered at 590 nm is stable over this longer timescale, with a decay comparable to the values reported for the 1100 nm probe. On titania, the cation formed upon electron injection is stable as well, but on an even longer timescale, in accordance with the infrared results of figure 5.7. Global fitting procedure also revealed components of several tens of picoseconds in addition to the longer lifetimes. They might be attributed to fast recombination channels induced by the high pump fluence needed in these WLC measurements, inducing injection of several electrons per nanoparticle. As a consequence, some fast recombination can be observed. In summary, these do not permit to elucidate other processes.

### **470 nm excitation**

The observed dye absorption spectrum presented on figure 5.2 reveals that an excitation at 530 nm lies within the absorption shoulder of the dye spectrum, enhanced by adsorption onto semiconductors. To ensure that this broadening corresponds to a transition located on the dye, the ultrafast pump white-light-continuum-probe experiments were repeated with the excitation light tuned at  $\lambda_{\text{ex}} = 470$  nm, closer to the absorption maximum of the dye in solution. The results are omitted herein since they do not give further information than what is presented using a 530 nm pump.

## 5.4 Conclusions and outlook

The results brought by this study allow for a better understanding of the organic D- $\pi$ -A dyes behavior upon light absorption, using C204 dye as a model. The adsorption onto a mesoporous semiconductor does slightly red-shift the absorption spectrum as well as the emission spectrum. This lowering in energy is assigned to the stabilization of the LUMO of the dye after adsorption and corresponds to a shift of 0.3 eV of the  $E_{0-0}$ .

PIA measurements highlight the presence of an ICT state, even when the dye is adsorbed onto an insulator such as alumina. The dye cation formed after electron injection into titania is efficiently regenerated (99 % of intercepted cations) by an iodide-based electrolyte, confirming the potential of using this kind of dyes in a DSSC.

Femtosecond pump-probe spectroscopy has been carried out both in the visible domain, with a WLC-probe and in the NIR. The results confirm quantitative electron injection within a few picoseconds. The slowest time component assigned to electron injection is  $\tau = 1.71$  ps. A potential structural change following light absorption is revealed onto alumina, but not present anymore in the titania case.

---

## 5.5 References

1. Nazeeruddin, M. K.; Kay, A.; Rodicio, I.; Humphry-Baker, R.; Muller, E.; Liska, P.; Vlachopoulos, N.; Grätzel, M. *J. Am. Chem. Soc.* **1993**, *115*, 6382–6390.
2. Nazeeruddin, M. K.; Zakeeruddin, S.; Humphry-Baker, R.; Jirousek, M.; Liska, P.; Vlachopoulos, N.; Shklover, V.; Fischer, C.; Grätzel, M. *Inorg. Chem.* **1999**, *38*, 6298–6305.
3. Wang, P.; Zakeeruddin, S.; Moser, J. E.; Nazeeruddin, M. K.; Sekiguchi, T.; Grätzel, M. *Nat. Mater.* **2003**, *2*, 402–407.
4. Gao, F.; Wang, Y.; Shi, D.; Zhang, J.; Wang, M.; Jing, X.; Humphry-Baker, R.; Wang, P.; Zakeeruddin, S.; Grätzel, M. *J. Am. Chem. Soc.* **2008**, *130*, 10720–10728.
5. Li, C.; Yum, J.-H.; Moon, S.-J.; Herrmann, A.; Eickemeyer, F.; Pschirer, N. G.; Erk, P.; Schoeneboom, J. C.; Muellen, K.; Grätzel, M.; Nazeeruddin, M. K. *ChemSusChem* **2008**, *1*, 615–618.
6. Hara, K.; Sato, T.; Katoh, R.; Furube, A.; Ohga, Y.; Shinpo, A.; Suga, S.; Sayama, K.; Sugihara, H.; Arakawa, H. *J. Phys. Chem. B* **2003**, *107*, 597–606.
7. Ito, S.; Miura, H.; Uchida, S.; Takata, M.; Sumioka, K.; Liska, P.; Comte, P.; Pechy, P.; Grätzel, M. *Chem. Commun.* **2008**, 5194–5196.
8. Hara, K.; Wang, Z.-S.; Sato, T.; Furube, A.; Katoh, R.; Sugihara, H.; Dan-Oh, Y.; Kasada, C.; Shinpo, A.; Suga, S. *J. Phys. Chem. B* **2005**, *109*, 15476–15482.
9. Xu, M.; Wenger, S.; Bala, H.; Shi, D.; Li, R.; Zhou, Y.; Zakeeruddin, S.; Grätzel, M.; Wang, P. *J. Phys. Chem. C* **2009**, *113*, 2966–2973.
10. Ardo, S.; Meyer, G. J. *Chem. Soc. Rev.* **2009**, *38*, 115–164.
11. Huber, R.; Moser, J. E.; Grätzel, M.; Wachtveitl, J. *J. Phys. Chem. B* **2002**, *106*, 6494–6499.
12. Kitamura, T.; Ikeda, M.; Shigaki, K.; Inoue, T.; Anderson, N.; Ai, X.; Lian, T.; Yanagida, S. *Chem. Mater.* **2004**, *16*, 1806–1812.
13. Myllyperkiö, P.; Manzoni, C.; Polli, D.; Cerullo, G.; Korppi-Tommola, J. E. I. *J. Phys. Chem. C* **2009**, *113*, 13985–13992.

- 
14. Benkő, G.; Kallioinen, J.; Korppi-Tommola, J. E. I.; Yartsev, A. P.; Sundström, V. *J. Am. Chem. Soc.* **2002**, *124*, 489–493.
  15. Kallioinen, J.; Benkő, G.; Sundström, V.; Korppi-Tommola, J. E. I.; Yartsev, A. P. *J. Phys. Chem. B* **2002**, *106*, 4396–4404.
  16. Kuciauskas, D.; Monat, J.; Villahermosa, R.; Gray, H.; Lewis, N. S.; McCusker, J. K. *J. Phys. Chem. B* **2002**, *106*, 9347–9358.
  17. Asbury, J.; Anderson, N.; Hao, E.; Ai, X.; Lian, T. *J. Phys. Chem. B* **2003**, *107*, 7376–7386.
  18. Tachibana, Y.; Haque, S. A.; Mercer, I.; Moser, J. E.; Klug, D. R.; Durrant, J. R. *J. Phys. Chem. B* **2001**, *105*, 7424–7431.
  19. Wenger, B.; Grätzel, M.; Moser, J. E. *J. Am. Chem. Soc.* **2005**, *127*, 12150–12151.
  20. West, W.; Carroll, B.; Whitcomb, D. *J. Phys. Chem-Us* **1952**, *56*, 1054–1067.
  21. Steiger, R.; Kitzing, R.; Junod, P. *J. Photogr Sci* **1973**, *21*, 107–116.
  22. Kay, A.; Grätzel, M. *J. Phys. Chem-Us* **1993**, *97*, 6272–6277.
  23. Liang, M.; Xu, W.; Cai, F.; Chen, P.; Peng, B.; Chen, J.; Li, Z. *J. Phys. Chem. C* **2007**, *111*, 4465–4472.
  24. Shen, P.; Liu, Y.; Huang, X.; Zhao, B.; Xiang, N.; Fei, J.; Liu, L.; Wang, X.; Huang, H.; Tan, S. *Dyes and Pigments* **2009**, *83*, 187–197.
  25. Roquet, S.; Cravino, A.; Leriche, P.; Aleveque, O.; Frere, P.; Roncali, J. *J. Am. Chem. Soc.* **2006**, *128*, 3459–3466.
  26. Qin, H.; Wenger, S.; Xu, M.; Gao, F.; Jing, X.; Wang, P.; Zakeeruddin, S.; Grätzel, M. *J. Am. Chem. Soc.* **2008**, *130*, 9202–+.
  27. Boschloo, G.; Hagfeldt, A. *Inorganica Chimica Acta* **2008**, *361*, 729–734.
  28. Snaith, H. J.; Humphry-Baker, R.; Chen, P.; Cesar, I.; Zakeeruddin, S.; Grätzel, M. *Nanotechnology* **2008**, *19*, 424003.
  29. Zhang, Z.; Ito, S.; Moser, J. E.; Zakeeruddin, S.; Grätzel, M. *ChemPhysChem* **2009**, *10*, 1834–1838.





# Chapter 6

## Concluding remarks and outlook

In this work, we studied the dynamics of several electron transfer processes at the surface of dye-sensitized semiconductor films. The obtained results provide several new findings that allow for a better understanding of the parameters governing these electron transfers. Especially, these results are relevant for the development of new systems, dyes and electrolytes, for the dye-sensitized solar cell (DSSC).

The reductive quenching reported in chapter 3 is a loss pathway for the DSSC. With the use of ionic liquids in electrolytes to stabilize the DSSC, and the high concentrations of redox mediator used, this issue cannot be neglected. This reaction is in kinetic competition with the electron injection into the semiconductor. As a consequence, and especially with the recent use of organic donor-bridge-acceptor (D- $\pi$ -A) dyes for sensitization, it is crucial to have a dye that injects as fast as possible. The reductive quenching reaction occurs within the first ten picoseconds and therefore a weak coupling of the dye to the surface might lead to such unwanted reaction. Electron injection from a D- $\pi$ -A dye, C204, is found to occur inhomogeneously, with a first part within our excitation pulse, i.e.  $< 70$  fs and a longer  $\tau = 1.7$  ps, one order of magnitude slower than ultrafast component. Although a large time

range is found between the electron injection and the back electron transfer reaction, such annihilation reaction might occur and lower the photon-to-current efficiency.

The interception of the dye cation by iodide as a redox mediator reported in chapter 4 is also a key reaction in the DSSC. The need of two iodide ions to reduce the oxidized dye implies that adsorption equilibrium are required for the reaction to complete before charge recombination. The importance of having a good association site located on the dye is revealed in this study. When such a site is found, the interception reaction might follow an associative mechanism. Oppositely, when the access to the dye is less favorable, a repulsive behavior is encountered. The use of four different D- $\pi$ -A dyes in the same conditions reveal the same findings, until a case in which steric hindrance dramatically slows down the reaction. As a consequence, the design of new organic dyes for the DSSC has to take into account, the need for efficient association sites for iodide, located as close as possible to the hole. This has to apply in addition to the usual thermodynamic and electronic considerations. However, the intrinsic mechanism of dye regeneration at the surface of semiconductors, by iodide, remains unclear and not fully explained. Especially in the working conditions of DSSC devices, in which the electrolyte comprises several additives that might alter the dye-iodide interaction.

Chapter 5 reports a study of one of these D- $\pi$ -A dyes, C204. The design of this dye efficiently locates the lowest unoccupied molecular orbital of the dye as close as possible to the surface. Oppositely, the hole acceptor moiety is at the other end of the molecule, preventing a fast back electron transfer. The internal charge transfer state that rise from this situation is observed in solution with a lifetime  $\tau = 61$  ps. However, the cause for the relatively slow electron injection observed ( $\tau = 1.7$  ps) is unraveled. Further studies on the anchoring of this dye to the surface are necessary. Also the effect of the co-adsorbants used in DSSC development might be a parameter affecting the electron injection rate significantly.

# Remerciements

Cette thèse est le fruit de mon travail de ces quatre dernières années. Si ce document a pu voir le jour, c’est grâce à de nombreuses personnes que je tiens ici à remercier.

Je remercie chaleureusement le Prof. Jacques-E. Moser pour m’avoir fait confiance, d’abord en 2003 lors de l’accomplissement de mon travail de diplôme au sein de son groupe, puis en 2006 pour m’avoir engagé pour l’accomplissement de cette thèse de doctorat. Il est l’initiateur de ce projet de recherche, mais a su me laisser une grande autonomie dans mes recherches. Lors de questions difficiles ou plus simples, sa porte était toujours ouverte pour une discussion, qui bien souvent se prolongeait au delà de la science pure.

Je tiens également à remercier le Prof. Michael Grätzel qui m’a permis de réaliser ce travail au sein du laboratoire de photonique et interfaces. Ce grand laboratoire pluridisciplinaire apporte un cadre unique à la réalisation d’un travail de doctorat.

Je remercie également mes prédécesseurs sur l’installation de la “femtocave”. D’abord Serge Pelet qui a construit le setup, mais aussi Bernard Wenger qui m’a formé à l’utiliser. Je lui suis particulièrement reconnaissant pour le temps qu’il m’a consacré, même après son départ de l’EPFL, au cours de multiples conversations sur Skype qui m’ont permis de finalement dompter le setup femtoseconde.

Je remercie encore mes collègues. Angela Punzi, qui est malheureusement arrivée que trop tard au sein du groupe, ainsi que Jan Brauer, avec qui

nous nous partageons la “femtocave”. Plusieurs membres du LPI reçoivent également mes remerciements. Pour ses discussions scientifiques toujours enrichissantes Robin Humphry-Baker, pour sa disponibilité et la qualité de ses préparations chimiques de dioxyde de titane Pascal Comte, pour une source inépuisable de colorants Shaik Zakeeruddin. Je ne vais pas tous les nommer, mais je remercie aussi collectivement toute l’équipe du couloir F, pour les diverses collaborations scientifiques que nous avons pu avoir, mais aussi pour les très bons moments passés ensemble, après le travail.

Les services de l’ISIC, le magasin, les ateliers mécaniques et électroniques ainsi que Frédéric Gummy reçoivent également mes meilleurs remerciements. Je ne vais pas non plus oublier Pierre-André Perroud, dit le PAP !

Il y a aussi mes compagnons d’études, en particulier Hugues, Loïck, Jérém, Le Raf, Séb. . .

Et pour terminer, un grand merci va à mes parents qui m’ont toujours encouragé et soutenu dans mes projets !

# Curriculum Vitae

**Joël Teuscher**

chemical engineer

Rue des Lilas 3, CH-1202 GENÈVE

Phone : + 41 22 340 63 90

E-mail : joel.teuscher@a3.epfl.ch

## État civil

31 years old; 07.05.1979

Single

Geneva, Switzerland

## Education

**2006 - 2010 Doctoral Studies**, Laboratory for Photonics and Interfaces, École Polytechnique Fédérale de Lausanne (EPFL);

**2004 Chemical engineer diploma**, Section of Chemistry and Chemical Engineering, EPFL;

**1998 Maturité Fédérale de type C** (scientific branch), Collège de Candolle, Genève, mention bien (grade good).

## Research projects

- 2006 - 2010 PhD Project** : Ultrafast electron transfer dynamics in the dye sensitization of wide-bandgap nanocrystalline semiconductors for solar cells applications, directed by Prof. J.-E. Moser and Prof. M. Grätzel, Laboratory for Photonics and Interfaces, Photochemical Dynamics Group, Institute of Chemical Sciences and Engineering (ISIC), EPFL;
- 2004 - 2005 Civil Service** : Development of high performance liquid chromatography coupled to an ion-trap mass spectrometer (HPLC-MS(n)) analysis methods for therapeutic drug monitoring, Clinical Chemistry Central Laboratory, University Hospitals of Geneva (HUG);
- 2003 - 2004 Diploma Thesis in Physical Chemistry** : Investigation de l'agrégation de complexes polypyridyles de ruthénium (II) à la surface d'oxydes nanocrystallins par photolyse par éclair laser, directed by Dr. J.-E. Moser, Laboratory for Photonics and Interfaces, Photochemical Dynamics Group, ISIC, EPFL;
- 2003 Semester Project in Chemical Engineering** : Hydrovoltaic cells, directed by Prof. C. Comninellis, Groupe de Génie Électrochimique, ISIC, EPFL.

## Teaching experience

- **2007 - 2010 : Teaching Assistant**, five semester projects and two master Projects supervision, EPFL;
- **2006 - 2008 : Teaching Assistant**, exercises of the "Thermodynamique chimique" course given by Prof. M. Grätzel, EPFL;
- **2000 - 2001 : Assistant-Étudiant**, exercises of the "Applied Chemistry" course given by Prof. C. Comninellis, EPFL.

## Language skills

- **French** Mother tongue;
- **English** Good written and spoken level;
- **Spanish** Good written and spoken knowledge, becoming steadily more proficient;
- **German** Good written and spoken knowledge, becoming steadily more proficient;

## Computer skills

- **Operating systems** : Familiarity with Mac OS 9 & X, Windows, Linux;
- **Softwares** : Microsoft Office suite, LaTeX; Wavemetrics Igor Pro, data treatment software; National Instruments Labview, virtual instrument software, control of apparatus and data treatment;

## Published and unpublished work

- **Competition between charge injection and reductive quenching at the surface of dye-sensitized semiconductors, an evidence for dye aggregation**, J. Teuscher, B. Wenger, S. M. Zakeeruddin, M. Grätzel and J.-E. Moser, *J. Am. Chem. Soc.*, **2010**, in prep.;
- **Dynamics of an organic D- $\pi$ -A dye sensitizing TiO<sub>2</sub>**, J. Teuscher, R. Humphry-Baker, S. M. Zakeeruddin, P. Wang, M. Grätzel and J.-E. Moser, *J. Phys. Chem. C*, **2010**, in prep.;

- **Molecular Design of Metal-free D- $\pi$ -A Substituted Sensitizers for Dye-sensitized Solar Cells**, L. Alibabaei, M. Wang, N. Pootrakulchote, J. Teuscher, D. Di Censo, R. Humphry-Baker, J.-E. Moser, K.-Y. Kay, S. M. Zakeeruddin and M. Grätzel, *Inorg. Chem.*, **2010**, in prep.;
- **Application of Cu(II) and Zn(II) Coproporphyrins as sensitizers for thin film dye sensitized solar cells**, L. Alibabaei, M. Wang, R. Giovannetti, J. Teuscher, D. Di Censo, J.-E. Moser, P. Compte, F. Pucciarelli, S. M. Zakeeruddin, and M. Grätzel, *Energy Environ. Sci.*, **2010**, accepted;
- **Efficient Electron Transfer and Sensitizer Regeneration in Stable  $\pi$ -Extended Tetrathiafulvalene-Sensitized Solar Cells**, S. Wenger, P.-A. Bouit, Q. Chen, J. Teuscher, D. Di Censo, R. Humphry-Baker, J.-E. Moser, J. L. Delgado, N. Martín, S. M. Zakeeruddin and M. Grätzel, *J. Am. Chem. Soc.*, **2010**, vol. 132, pp 5164-5169;
- **High Extinction Coefficient antenna Dye in Solid-State Dye-Sensitized Solar Cells: A Photophysical and Electronic Study**, H. J. Snaith, C. S. Karthikeyan, A. Petrozza, J. Teuscher, J. E. Moser, M. K. Nazeeruddin, M. Thelakkat, and M. Grätzel, *J. Phys. Chem. C*, **2008**, vol. 112(20), pp 7562-7566;
- **Dynamics of photoinduced interfacial electron transfer and charge transport in dye-sensitized mesoscopic semiconductors**, V. K. Thorsmølle, B. Wenger, J. Teuscher, C. Bauer and J.-E. Moser, *Chimia*, **2007**, vol. 61, pp 631-634;
- **Efavirenz-induced Urolithiasis**, G. Wirth, J. Teuscher, J.-D. Graf, and C. Iselin, *Urol. Res.*, **2006**, vol. 34(4), pp 288-289;
- **Charge separation and efficient light energy conversion in sensitized mesoscopic photoelectrochemical cells based on binary ionic liquids**, P. Wang, B. Wenger, R. Humphry-Baker, J.-E. Moser, J. Teuscher, W. Kantelehn, J. Mezger, E. V. Stoyanov, S. M. Zakeeruddin, and M. Grätzel, *J. Am. Chem. Soc.*, **2005**, vol. 127(18), pp 6850-6856.